Università degli Studi di Ferrara

DOTTORATO DI RICERCA IN
FISICA

CICLO XXV

COORDINATORE Prof. Vincenzo Guidi

X-ray characterization of innovative semiconductor crystals and study of their applications

Settore Scientifico Disciplinare FIS/01

Dottoranda
Dott. Ilaria Neri

Tutore
Prof. Vincenzo Guidi

Anni 2010/2012

INDEX

Introduction

Semiconductor materials exist in many structural forms and therefore require a large range of experimental techniques for their analysis. However, for investigation of structure on the atomic scale, X-ray diffraction is a very sensitive analysis tool. It has been used for a long time and has successfully helped scientists to reveal and study the structure of a wide range of materials.

This thesis focuses on experimental work, carried out both at Sensor and Semiconductor Laboratory (SSL, Ferrara, Italy) and at European Synchrotron Radiation facility (ESRF, Grenoble, France), in which X-ray diffraction technique has been used to probe and study the properties of semiconductor crystals for applications in astrophysics and photovoltaics.

In the last years, the field of soft gamma-ray telescopes aimed to studying violent phenomena occurring in galaxy has received a tremendous impulse by the advent of a new generation of semiconductor crystals, which resulted in a significant increase of performance with respect to traditional instruments operating in this part of the electromagnetic spectrum. In particular, for realization of a Laue lens as focusing optics to concentrate X and gamma rays coming from the sky, the key factor was the usage of silicon and germanium crystals exploiting deformations, which provide extremely uniform bending throughout the whole crystal thickness.

X-ray diffraction has been applied to silicon and germanium bent crystals with the aim to study their structural deformation and diffraction properties, for the purpose of diffracting high-energy photons for astrophysical observations through a Laue lens. In the framework of "Laue project", devoted to build a broadband (80-600 keV) focusing lens and financed by the Italian Space Agency (ASI), a thorough X-ray characterization allowed accurate adjustment of the experimental parameters for crystal fabrication and certification of its quality of diffraction properties prior to installation as optical element onto the lens.

With regard to photovoltaics, semiconductors crystals are still under investigation as efficient heteroepitaxial structures for multi-junction solar cells.

Several characterization techniques have been used for the evaluation of heteroepitaxial semiconductors, and have enabled the advancement of the field to its present state. X-ray diffraction is the most widely used technique for the characterization of heteroepitaxial layers. In fact, it is nondestructive and yields a wealth of structural information, including the lattice constants and strains, composition and defect densities.

In this thesis it will be shown main experimental results of X-ray characterization of semiconductor crystals of silicon and germanium as well as their applications to astrophysics and material science.

Chapter 1 contains a theoretical background on X-ray diffraction in perfect and in specifically deformed crystals. Chapter 2 highlights the equipment which have been used for X-ray characterization of the samples analyzed in the framework of this thesis. Chapter 3 is

devoted to the investigation of Si and Ge crystals fabricated at SSL for the realization of a Laue lens for astrophysics. With this aim, main experimental results of X-ray diffraction obtained at ESRF are presented. In particular, it will be pointed out that crystals diffracted photons from 150 to 700 keV with efficiency peaking 95% at 150 keV for Si. Chapter 4 presents heteroepitaxial SiGe samples, their fabrication and investigation of structural properties by X-ray analysis at SSL, for their usage as solar cells in photovoltaics. Finally, an Appendix shows results of X-ray study on ceramic coatings for applications of wear resistant materials in metallurgy.

1. X-ray diffraction in crystals

1.1. Theory of X-ray diffraction in ideal crystals

In the present chapter, the basics of the theory of X-ray diffraction in crystals will be described. The following concepts and equations are mainly taken from Refs. [1.1-1.5]. Please, refer to these documents for further details as well as to other articles in this volume for a good coverage of recent works on hard X-ray diffraction, both theoretical and experimental. The possibility of using crystals as natural diffraction gratings for X rays was conceived by von Laue in 1912, and the subsequent experiments immediately proved that the idea was correct. In fact, von Laue showed that the observed effects could be interpreted as due to diffraction of electromagnetic waves in a three-dimensional grating [1.6, 1.7] and his discovery gave convincing proof of both the wave nature of X rays and of the periodic structure of crystals. Thus, the foundation was laid for two important fields of scientific research, i.e., the study of X rays and the study of crystal structure. The improved experimental technique due to W. H. and W. L. Bragg [1.8, 1.9] greatly contributed to the rapid development of both fields and their work clearly proved the far reaching consequences of Von Laue‘s discovery.

1.1.1. The Laue and Bragg Equations

As stated in Ref. [1], a linear diffraction grating may conveniently be defined as a straight line along which the scattering power is a periodic function of position, i.e.,

$$\psi(\bar{r}) = \psi(\bar{r} + L_1\bar{a}_1) \tag{1.1.}$$

where L_1 is any integer and $\bar{a}_1$ is the period and measures the vector separation of neighboring points. An electromagnetic plane wave of monochromatic radiation incident onto the grating will be then scattered in all directions by a line element. Since the scattering power of the grating has a periodic nature, the diffraction maxima will take place in the directions corresponding to path differences equal to an integral number of wavelengths.

This diffraction problem leads to the formula

$$\bar{a}_1 \cdot \left(\bar{k}_{H_1} - \bar{k}_0\right) = H_1 \tag{1.2.}$$

$\bar{k}_0$ is the wave vector of incident X-ray beam and $\bar{k}_{H_1}$ that of the diffracted beam, i.e.,

$$\bar{k}_0 \equiv \frac{1}{\lambda} u_0 \,, \quad \bar{k}_{H_1} \equiv \frac{1}{\lambda} \bar{u}_{H_1} \tag{1.3.}$$

Here λ is the wavelength while $\bar{u}_0$ and $\bar{u}_{H_1}$ represent unit vectors along the directions of incident and maximum diffraction, respectively.

On the other hand, a three-dimensional grating corresponds to a spatial distribution of matter for which the scattering power is a triply periodic function of position or

$$\psi(\bar{r}) = \psi(\bar{r} + L_1\bar{a}_1 + L_2\bar{a}_2 + L_3\bar{a}_3) \tag{1.4.}$$

Thus, the three-dimensional grating can be considered as consisting of three sets of linear gratings with periods $\bar{a}_1, \bar{a}_2$ and $\bar{a}_3$. In order to find the diffraction maxima for such a three-dimensional grating, the wave vectors must simultaneously satisfy equation 1.2. for each of the components, i.e.,

$$\begin{aligned} \bar{a}_1 \cdot \left(\bar{k}_{H_1H_2H_3} - \bar{k}_0\right) &= H_1 \\ \bar{a}_2 \cdot \left(\bar{k}_{H_1H_2H_3} - \bar{k}_0\right) &= H_2 \\ \bar{a}_3 \cdot \left(\bar{k}_{H_1H_2H_3} - \bar{k}_0\right) &= H_3 \end{aligned} \tag{1.5.}$$

These are Laue's equations, where H_1, H_2 and H_3 are integers associated with each diffraction maximum. These three scalars equations can be rearranged in more convenient form as a single vector equation, leading to

$$\bar{k}_H - \bar{k}_0 = \bar{B}_H \tag{1.6.}$$

that is called the Laue vector equation, where the abbreviated form of $\bar{k}_H$ $\left(\equiv \bar{k}_{H_1H_2H_3}\right)$ has been used. Here $\bar{B}_H = \bar{B}_{H_1H_2H_3} = H_1\bar{b}_1 + H_2\bar{b}_2 + H_3\bar{b}_3$, where $\bar{b}_1$, $\bar{b}_2$, $\bar{b}_3$ represents the vector set in reciprocal lattice space, i.e., reciprocal to $\bar{a}_1$, $\bar{a}_2$, $\bar{a}_3$. Thus, according to Eq. 1.6., $\bar{B}_H$ is associated with each diffraction maximum. If the first two equations in 1.5. are rearranged and subtracted from each other, we will have

$$\left(\frac{\bar{a}_1}{H_1} - \frac{\bar{a}_2}{H_2}\right) \cdot \bar{B}_H = 0 \tag{1.7.}$$

which means that $\left(\frac{\bar{a}_1}{H_1} - \frac{\bar{a}_2}{H_2}\right)$ must be perpendicular to $\bar{B}_H$, and similarly for all the combinations. If one considers a plane in lattice space that intercepts the "$\bar{a}_1$" axis at $1/H_1$, the "$\bar{a}_2$" axis at $1/H_2$ and the "$\bar{a}_3$" axis at $1/H_3$, the quantities H_1, H_2, H_3 may accordingly be denoted as Miller indices of a family of lattice planes. Therefore, equation 1.7. can only be satisfied if $\bar{B}_H$ is normal to the plane $(H_1 H_2 H_3)$.

Since $|\bar{k}_H| = |\bar{k}_0| = 1/\lambda$, the Laue vector equation expresses the fact that the vectors $\bar{k}_H$ and $\bar{k}_0$ are edges of a rhomb whose $\bar{B}_H$ is a diagonal as shown in Fig. 1.1. In the lattice space the sequence of planes represented by $\bar{B}_H$ makes equal angles with $\bar{k}_0$ and $\bar{k}_H$. One can thus considers the diffracted beam to be produced by a reflection of the incident beam in the family of planes normal to $\bar{B}_H$. The magnitude of left side of equation 1.6. results to be $\frac{2 \sin \theta_B}{\lambda}$ where θ_B is the Bragg angle and $2\theta_B$ the scattering angle. On the other hand, the magnitude of the right side is $1/d_{H_1 H_2 H_3}$ where d_H is the spacing between the sets of crystal planes. Therefore we have

$$\frac{2 \sin \theta_B}{\lambda} = \frac{1}{d_H} \qquad 1.8.$$

i.e., the Bragg equation. For a cubic crystal with lattice constant a, the spacing of the (hkl) planes is given by formula

$$d(hkl) = a(h^2 + k^2 + l^2)^{-1/2} \qquad 1.9.$$

The hkl Bragg angle is then

$$\theta_B(hkl) = \sin^{-1}\left[\lambda(h^2 + k^2 + l^2)^{1/2}/2a\right] \qquad 1.10.$$

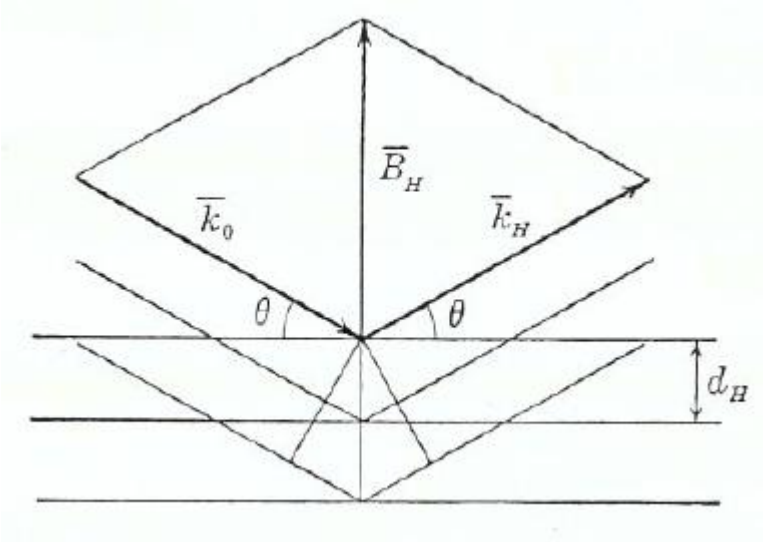

Figure 1.1: The Bragg condition for diffraction [1.1].

1.1.2. Construction of the diffracted wave vectors in the reciprocal lattice

To deepen the understanding Bragg's formulation of diffraction phenomenon, a simple geometric construction in the reciprocal lattice of the diffracted wave vectors associated with a given direction of incidence and a given wavelength was reported in Ref. [1.10]. As shown in Fig. 1.2, since the three vectors $\bar{k}_0, \bar{k}_H,$ and $\bar{B}_H$ form a closed triangle (see equation 1.6.), a vector $\bar{B}_H$ which satisfies the Laue equation must terminates on the sphere of reflection or the Ewald sphere. In fact, if the incident wave vector $\bar{k}_0$ is chosen at random, the Ewald sphere will not pass through any reciprocal lattice point in general. Thus, in order to produce diffraction maxima, it becomes necessary to adjust the wavelength or the incident direction in such a way that one or more of the reciprocal lattice points fall on the Ewald sphere. Indeed, as depicted in Fig. 1.2. when the wavelength or the direction of incidence $(\bar{k}_0)$ is varied, there will be a corresponding variation in the radius vector in the reciprocal lattice. If the Laue vector equation is satisfied a diffraction maximum will be produced.

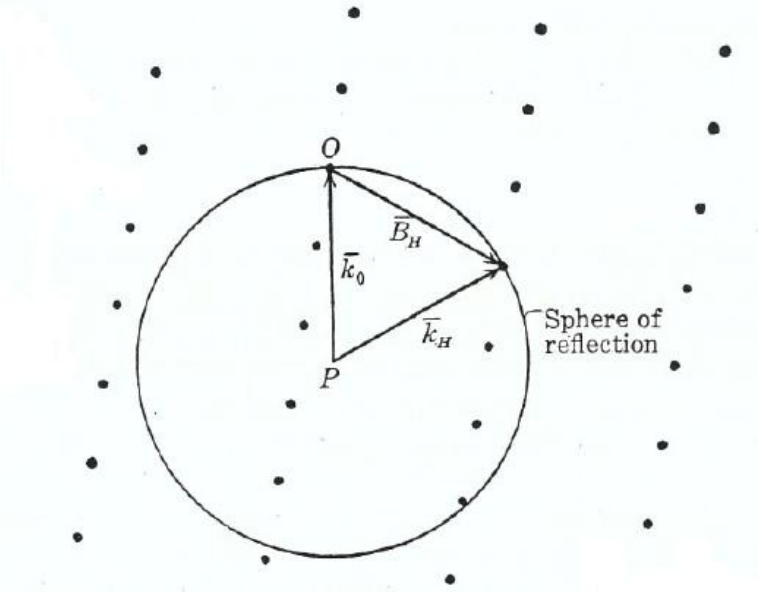

Figure 1.2: The Ewald sphere construction [1.1].

With this regard, there are several experimental methods which are being used to produce X-ray diffraction maxima. Since $\bar{k}_0$ is a function of three scalar variables, it is sufficient to vary only one of the three variables in the incident wave vector, while the other two are being fixed. However, two or all three variables may be varied at the same time.

With this aim, let $\lambda, \mu,$ and ν be the three scalar variables of the incident wave vector, where λ is the wavelength, while μ and ν are two parameters describing the direction of incidence of the plane wave. As said above, in order to produce diffraction maxima, it is necessary to allow at least one of the three quantities $\lambda, \mu,$ and ν to vary continuously. Therefore, the different experimental methods can be depicted as follows:

I. The wavelength is variable, but the direction of incidence is fixed, i.e., λ variable, $\mu = \mu_0, \nu = \nu_0$
II. The wavelength is fixed, but the direction of incidence varies with one degree of freedom, i.e., $\lambda = \lambda_0, \mu = \mu_0, \nu$ variable or $\lambda = \lambda_0, \nu = \nu_0, \mu$ variable.
III. The wavelength is fixed, but the direction of incidence changes with two degrees of freedom, i.e., $\lambda = \lambda_0, \mu$ and ν vary independently.

In cases I and II, the incident wave vector has one degree of freedom and the diffraction direction is then uniquely determined. The diffraction maxima are sharply defined, being recorded as spots on a photographic plate. The first method is called the *Laue method*, because it was used by Laue in its original experiments, and can be experimentally carried out by using continuous X rays. Since this technique is based on sharply defined direction of incidence, a single crystal must be used as sample under analysis. On the other hand, the second method consists in variation of the direction of incidence with one degree of freedom, thus the best way of achieving it is to rotate the sample relative to the incident X-ray beam, this latter being monochromatic. In this case a single crystal can be employed but one can also uses substances in the form of aggregates where the direction of incidence with respect to

such an aggregate will have one degree of freedom. This latter method is also called the *rotating crystal method*.

The third method consists in variation of the direction of incidence with two degrees of freedom. If a single crystal is available, one of the two parameters μ and ν can be changed at a time, i.e., it results to be the rotating crystal method again. However, the third method is of importance only in connection with the study of substances in the form of aggregates or powders having random orientation because the observed diffraction effects are the same as for a single crystal will all combinations of μ and ν. This method is commonly called the *powder method* and the diffraction maxima will draw out a line on a photograph film located on focal plane. Indeed, each diffraction pattern is made up of a large number of small spots, each from a separate crystallite of the aggregate and every spot is so small as to give the appearance of a continuous line.

For the sake of simplicity, there have been reported only the main methods for production of X-ray diffraction maxima. For more information, see Ref. [1.1].

1.1.3. X-ray scattering by a single electron and by a single atom

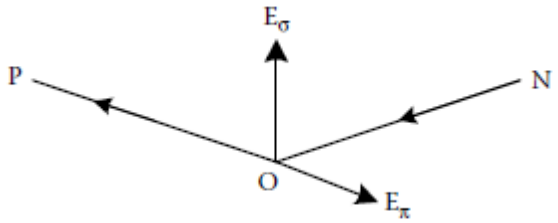

Fig. 1.3: Scattering of a randomly polarized X-ray beam from an electron [1.5].

As stated in Ref. [1.5], X rays are scattered in all directions by a single electron, with the scattered intensity strongly dependent on the scattering angle, φ. This dependence was derived by J. J. Thomson and is given by formula

$$I_e = I_0 \left(\frac{\mu_0}{4\pi}\right)^2 \left(\frac{q^4}{m^2 r^2}\right) \sin^2\theta \qquad 1.11.$$

where I_e is the intensity of scattering from a single electron at a distance r, $\mu_0 = 4\pi \times 10^{-7}\mathrm{Hm}^{-1}$, q is the charge of electron ($1.602 \times 10^{-19}\ C$), and m is the electron rest mass, i.e., $9.11 \times 10^{-31} kg$. φ is the angle between the scattering direction and the direction of acceleration for the electron, thus depending on the polarization of the X-ray beam. If the incident wave is unpolarized, the angle φ becomes indeterminate and the term $\sin^2\theta$ must be replaced by its average value. Considering Fig. 1.3, an unpolarized X-ray beam diffusing

from point *N* encounters an electron at the origin *O* and the scattered beam is consequently observed at point *P*. Electric vector $\bar{E}$ can be divided into two orthogonal components, $E_\sigma$and E_π, where the first is perpendicular to both the line *NO* and the scattering plane *NOP* and E_π is the component parallel to this plane. Because of the random nature of the direction of $\bar{E}$, the mean square values are equal, i.e., $\overline{E_\sigma^2} = \overline{E_\pi^2} = \bar{E}$. The scattered intensity is thus divided between the two polarization, leading to

$$I_{0\sigma} = I_{0\pi} = {}^{I_0}/_2 \qquad 1.12.$$

At point *P* the scattered intensity is the sum of the intensities for the two polarizations. In particular, for σ polarization, $\varphi = {}^{\pi}/_2$, but for π polarization, $\varphi = {}^{\pi}/_2 - 2\theta$, where θ is the scattering angle. Then the intensity scattered to the point *P* results to be

$$I_P = \frac{I_0}{2}\left(\frac{\mu_0}{4\pi}\right)^2\left(\frac{q^4}{m^2r^2}\right)(1+\cos^2 2\theta) \qquad 1.13.$$

This is the familiar Thomson scattering formula for an unpolarized X-ray beam by a single electron. In an X-ray diffraction experiment, all of the terms in this equation are constant except for $(1+\cos^2 2\theta)$, which is called the polarization factor.

The total effect of the electrons which scatter an X-ray beam in an atom is taken into account by the atomic scattering factor f, which is defined as the ratio between the amplitude of a wave scattered by an atom and that scattered by a single electron. The atomic scattering factor depends on the atomic number, the scattering Bragg angle and the wavelength of X-ray beam. As highlighted in Ref. [1.2], the exact calculation of the atomic scattering factor is usually difficult because it requires to consider the coherent diffusion by each electron of an atom, taking into account quantum physics. Numerical values can be obtained by using analytic expressions available in the *International Tables for X-ray Crystallography* [1.11]. These expressions are best fits to experimentally determined atomic scattering factors and are in the form

$$f = c + \sum_{i=1}^{4} a_i e^{-\frac{b_i}{4d_{hkl}^2}} \qquad 1.14.$$

where the c, a_i, and b_i in $\dot{A}^2$ coefficients are tabulated in [1.11] for many elements.

While the atomic scattering factor provides for the intensity of the beam as diffused by a given atom, the structure factor F is the sum of all scattering contributions from individual atoms in a unit cell, i.e., the scattering power of a unit cell

$$F(\bar{B}_H) = f_m \sum_{m=1}^{n} e^{-i2\pi\bar{B}_H\cdot(u_m\bar{a}_1+v_m\bar{a}_2+lw_m\bar{a}_3)} \quad 1.15.$$

where n represents the number of atoms per elementary lattice, and the m^{th}atom has been considered to be at the position (u_m, v_m, w_m) in the unit cell defined by the lattice vectors $(\bar{a}_1, \bar{a}_2, \bar{a}_3)$. f_m is the atomic scattering factor of the m^{th} atom. If the atoms of the lattice are of the same kind (e.g., silicon germanium, copper, etc.) the structure factor can be written as:

$$F = f_m \sum_{m=1}^{n} e^{-i2\pi\bar{B}_H\cdot(u_m\bar{a}_1+v_m\bar{a}_2+lw_m\bar{a}_3)} = fG \quad 1.16.$$

where G is the geometrical factor which depends on the positions of the atoms in the lattice and on the Miller indexes and shows that, due to destructive interferences, some crystallographic planes can not reflect the beam. Theoretical computation of the geometrical factor can be found in [1.2].

Finally, the amplitude of scattering from a single unit cell can be written as

$$FE_e \quad 1.17.$$

E_e being the amplitude of scattering from a free (Thomson) electron.

1.1.4. X-ray scattering from a single ideal crystal

Under the assumptions highlighted in Ref. [1.1], the amplitude of scattering due to a single ideal crystal will be given by the sum of the contributions from the various unit cells, taking into account the phase differences. Considering an entire ideal crystal, if the origin is chosen at a corner of one unit cell, the location of any other unit cell can be described in terms of a lattice vector $\bar{A}_L = L_1\bar{a}_1 + L_2\bar{a}_2 + L_3\bar{a}_3$. In fact, the contribution to the total amplitude from the unit cell positioned at $\bar{A}_L$ is $FE_e e^{i\bar{s}\cdot\bar{A}_L}$, where $\bar{s} = 2\pi(\bar{k} - \bar{k}_0) = 2\pi\bar{B}_H$ and $\bar{s}\cdot\bar{A}_L$ is the difference in phase with respect to the radiation reflected by the unit cell located at the origin. Thus, the total amplitude is simply given by

$$E_t = E_e F \sum_L e^{i\bar{s}\cdot\bar{A}_L} \tag{1.18.}$$

where the summation must be extended all over the unit cells of the crystal under consideration. If one considers a crystal with parallelepiped shape having edges $N_1\bar{a}_1, N_2\bar{a}_2, N_3\bar{a}_3$, the total number of unit cells in the crystal is therefore $N_1N_2N_3 = N$ and the expanded form of the summation in equation 1.19. becomes

$$\sum_L e^{i\bar{s}\cdot\bar{A}_L} = \sum_0^{N_1-1} e^{iL_1\bar{s}\cdot\bar{a}_1} \sum_0^{N_2-1} e^{iL_2\bar{s}\cdot\bar{a}_2} \sum_0^{N_3-1} e^{iL_3\bar{s}\cdot\bar{a}_3} \tag{1.19.}$$

which is the one of a geometric series and hence equation 1.19. turns out to be

$$\frac{E_t}{E_e} = F \prod_i \frac{e^{iN_i\bar{s}\cdot\bar{a}_i} - 1}{e^{i\bar{s}\cdot\bar{a}_i} - 1} \tag{1.20.}$$

The intensity ratio can be obtained from the amplitude ratio by multiplication with the complex conjugate, thus leading to

$$\frac{I_t}{I_e} = |F|^2 \prod_i \frac{\sin^2 \frac{1}{2} N_i\bar{s}\cdot\bar{a}_i}{\sin^2 \frac{1}{2}\bar{s}\cdot\bar{a}_i} \tag{1.21.}$$

Hence, due to the periodicity of the crystal, the intensity of the diffracted beam is essentially zero unless

$$\begin{aligned} \bar{s}\cdot\bar{a}_1 &= 2\pi H_1 \\ \bar{s}\cdot\bar{a}_2 &= 2\pi H_2 \\ \bar{s}\cdot\bar{a}_3 &= 2\pi H_3 \end{aligned} \tag{1.22.}$$

this latter being identical to the Laue vector equation. Finally, the intensity of scattering from an ideal crystal is

$$I = I_e F^2 N^2 \tag{1.23.}$$

where N is the number of unit cells in the crystal and F the structure factor.

It is worth to note that equation 1.21. has been obtained assuming that the incident wave is not affected by the presence of the crystal medium. In fact, an X-ray beam traversing matter will suffer absorption, i.e., there will be a deviation in energy from the incident beam. The absorption phenomena which occur in crystal matter are of two main types. The first type is the photoelectric absorption where the incident radiation energy is converted into the kinetic energy of an ejected electron. The second type of absorption is based on a transfer of energy from the incident to the scattered radiation and in this latter case, there are two scattering processes, i.e., the Compton scattering and the coherent scattering. According to equation 1.21., the intensity of the coherent scattering from a crystal is negligible except when the Laue conditions are satisfied. When the Laue equation is not fulfilled, the incident beam will undergo the absorption due to the ejection of photoelectrons and Compton scattering, hereinafter referred to as normal absorption. On the other hand, the absorption which arises when the Laue conditions are satisfied and diffracted waves are produced is called extinction. Normal absorption is described by means of the linear absorption coefficient μ which is defined as the fractional intensity decrease per unit length of path through the crystal medium. Since equation 1.21. shows that diffracted intensity decreases as the crystal size decreases, in the limit of very small crystals, both normal absorption and extinction can be neglected. Later studies proved that extinction must be taken into account when the linear dimension of the crystal is of the order of $10^{-4}\ cm$ or greater. Thus, the intensity formula in equation 1.21. represents an asymptotic solution which holds true only for crystals having linear dimensions of $10^{-4}\ cm$ or smaller.

1.1.5. The dynamical theory of X-ray diffraction: basic concepts

As highlighted in the above section, the main concepts of X-ray diffraction theory presented so far neglected both normal absorption and extinction, thus being valid only in the limiting case of small crystals. On the other hand, the dynamical diffraction model has to be considered for best describing the physics of incident and diffracted waves within the crystal. With this regard, let's consider a crystal with a series of atomic planes which are parallel to each other as in Fig. 1.4.

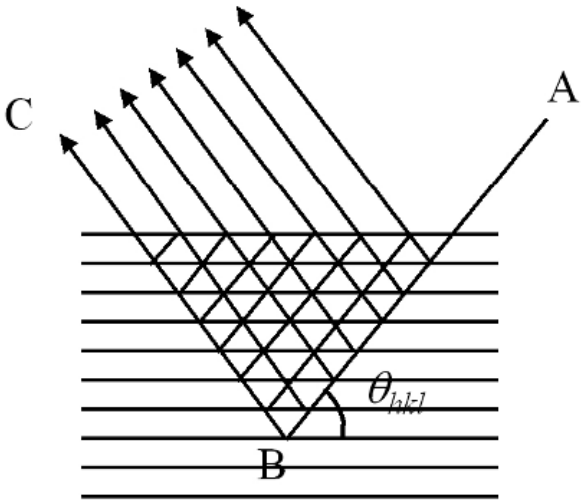

Fig. 1.4: Dynamical interaction of X rays with a perfect parallel-sided set of diffracting planes [1.3].

If the beam path AB of a photon is at an incident angle θ_{hkl} in such a way to scatter it in the direction BC, then it will also be at the correct incident angle to be scattered from the underside of these crystallographic planes. Therefore a dynamic situation occurs inside the crystal, where the energy of the incident beam decreases with depth due to losses and interferences between the multiple scattered beams along the direction AB. Clearly, normal absorption occurs for all directions of incidence, while extinction is important only when the incident wave vector has such a value that the Laue equation is satisfied.

This represents the basis of the dynamical scattering model proposed by Darwin in Refs. [1.12, 1.13]. The foundation of the dynamical theory is a solution of Maxwell's equations in the periodic electron density of the crystal. This theory has enabled the calculation of the intensities and shapes of diffraction profiles from thick, perfect and real crystals.

To understand how the photon is scattered within a crystal and generates an internal wave-field, the physical description given by Ewald or Laue can be followed [1.3]. In fact, each atomic site is considered to be occupied by a dipole which oscillates and emits radiation when a photon passes nearby. Due to the periodicity of the crystal, there will be an array of oscillating dipoles (also called "dipole-waves") all emitting electromagnetic radiation, which adds to the total radiation field and interacts with other dipoles. Each dipole has been assumed to emit in phase, thus producing two plane waves: an electromagnetic wave which is created by the dipole and the dipole itself. Nevertheless, since Ewald did not consider that the crystal has a distributed electron density and should hence be considered as a dielectric, Laue made another approach but obtaining the same results. Indeed, he thought the crystal to be formed by continuous negative charge with shielded positive charges, these latter being the atomic nuclei, in a periodic array. When no incident photon exists, any atomic site in the crystal can be seen as neutrally charged. On the other hand, when an electric field is applied there will occur a relative displacement of the charges which would result in an electric polarization and thus the induced electric field will be given by

$$\bar{D} = \bar{E} + 4\pi\bar{P} \tag{1.24.}$$

or

$$\bar{D} = (1 + \chi)\bar{E} \tag{1.25.}$$

where $\bar{E}$ is the applied electric field and $\bar{P}$ is the polarizing field. $\bar{\chi}$ is the polarizability or the electric susceptibility of the crystal as given by

$$\chi = -\frac{e^2\lambda^2}{\pi mc^2}\rho_e(\bar{r}) \tag{1.26.}$$

where e is the electric charge, λ the wavelength, m the mass of the electron, c the speed of light in vacuum and $\rho_e(\bar{r})$ is the variable electron density given by the formula

$$\rho_e(\bar{r}) = \frac{1}{V}\sum_h\sum_k\sum_l F\, e^{-2\pi i\bar{B}_H\cdot\bar{r}} \tag{1.27.}$$

where V is the volume of the unit cell and the assumption that the electron density is strongly associated to the atomic sites, i.e., the inner electrons dominate has been made. The crystal can be therefore considered as a structure with an anisotropic periodic complex polarizability.

The electric field within the crystal must obey Maxwell's equations, thus the resulting electromagnetic field is the sum of plane waves, i.e.,

$$\begin{aligned}\bar{D} &= e^{2\pi ivt}\sum_H \bar{D}_H\, e^{-2\pi i\bar{K}_H\cdot\bar{r}}\\ \bar{H} &= e^{2\pi ivt}\sum_H \bar{H}_H\, e^{-2\pi i\bar{K}_H\cdot\bar{r}}\end{aligned} \tag{1.28.}$$

which represent the total electric displacement and magnetic field at time t and position r for a total of m waves propagating within the crystal. $\nu = {}^{c}/_{\lambda}$ is the frequency of the electromagnetic wave while $\bar{K}_m$ is the scattered wave vector satisfying the Laue equation. $\bar{H}_m, \bar{D}_m$and $\bar{K}_m$ have to be determined on the basis of the boundary conditions and Maxwell's equations.

1.2. Theory of X-ray diffraction in mosaic and curved crystals

1.2.1. Definitions and assumptions

In this section two physical quantities should be introduced because they will be employed in the following. Such quantities, typically used to qualify the diffraction properties of a crystal, are *reflectivity* and *diffraction efficiency*. According to Ref. [1.2, 1.14], reflectivity is defined as the ratio of diffracted beam intensity over incident beam intensity while diffraction efficiency is the ratio of diffracted beam intensity over the transmitted one when no diffraction occurs.

In the previous section it was assumed that an incident wave entered a crystal through a plane boundary and produced a diffracted wave inside the crystal. In fact, the diffraction inside the crystal can either occur near the surface, this being referred to as Bragg geometry or "in volume", while the beam is propagating through the entire crystal (Laue geometry, see Fig. 1.5). Indeed, considering a parallel-plane bounded crystal of thickness T_0 with unlimited lateral dimension, the equations of the two boundary planes are $\bar{n} \cdot \bar{r} = 0$ and $\bar{n} \cdot \bar{r} = T_0$. Although the incident wave enters the crystal through the plane $\bar{n} \cdot \bar{r} = 0$, the diffracted wave may emerge either through the plane $\bar{n} \cdot \bar{r} = 0$ or through $\bar{n} \cdot \bar{r} = T_0$. Because the boundary conditions are different, this distinction is sharp and gives rise to the two geometries, i.e., the Bragg and Laue case respectively.

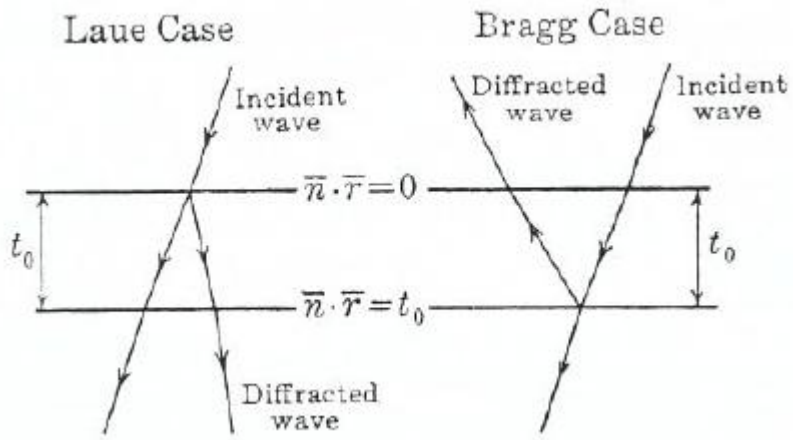

Figure 1.5: Distinction between Laue and Bragg geometries [1.1].

Since the framework of this thesis will mainly deal with X-ray diffraction in the Laue case, theoretical formulas in the following sections will be given for the Laue geometry.

1.2.2. Mosaic crystals

Mosaic crystals have been described by using Darwin's model [1.15], i.e., as an assembly of small perfect crystals, the crystallites, each slightly misaligned with respect to

each other according to an angular Gaussian distribution. For mosaic crystals the reflectivity is given by the formula [1.1, 1.14]

$$r_M = \frac{1}{2}\left(1 - e^{-2W(\Delta\theta)QT_0}\right)e^{-\mu T_0/\cos\theta_B} \qquad 1.29.$$

where the second factor is for diffraction efficiency, and the latter is the attenuation factor due to linear absorption μ within the crystal. T_0 is the crystal thickness traversed by the radiation, $\Delta\theta$ the difference between the angle of incidence and the Bragg angle θ_B and $W(\Delta\theta)$ the distribution function of crystallite orientations, namely

$$W(\Delta\theta) = 2\left(\frac{\ln 2}{\pi}\right)^{1/2}\frac{1}{\Omega_M}e^{-\ln 2\left(\frac{\Delta\theta}{\Omega_M/2}\right)^2} \qquad 1.30.$$

where Ω_M is the mosaicity of the crystal, i.e. the angular distribution of the crystallites. Finally, Q represents the integrated intensity diffracted by a single perfect crystal per unit of thickness. Considering the kinematical theory approximation [1.1], Q is simply given by

$$Q = \frac{\pi^2 d_{hkl}}{\Lambda_0{}^2\cos\theta_B} \qquad 1.31.$$

where d_{hkl} is the d spacing of planes hkl and Λ_0 the extinction length as defined by Authier [1.4] for the Laue case.

1.2.3. Curved crystals

Crystals having curved diffracting planes (CDP) are nowadays under investigation by the scientific community as an innovative concept because they appear very useful for several applications spanning from astrophysics to nuclear medicine [1.16-1.22].

Theory of X-ray diffraction in CDP crystals was widely developed in the past half century in the frame of dynamical theory of diffraction, with particular contribution by C. Malgrange [1.23]. The equations given by Malgrange represent an extension of the PPK theory of diffraction in distorted crystals [1.24, 1.25] for the case of a large and homogeneous

curvature. In this theory, the deformation of diffracting planes is described by the strain gradient $\boldsymbol{\beta}$ which, in the case of uniform curvature, can be written as

$$\beta = \frac{\Omega}{T_0 \delta_w} \tag{1.32.}$$

where Ω is the FWHM of the angular distribution of planes, i.e. the bending angle of the crystal and δ_w the Darwin width, namely the angular range around the Bragg angle for a flat crystal where diffraction is possible. When the orientation of the diffracting planes consistently changes over an extinction length owing to its curvature, the probability of diffraction parallel to the incident beam drops, so that Eq. 1.32 holds. Formally, this occurs when the strain gradient β is larger than a critical value $\beta_c = {}^{\pi}/_{2\Lambda_0}$. The reflectivity for a curved crystal in Laue geometry is given by

$$r_{curved} = \left[1 - e^{\left(\frac{-\pi^2}{\alpha}\right)}\right] e^{\left(\frac{-\mu T_0}{\cos\theta_B}\right)} \tag{1.33.}$$

where the first factor is for diffraction efficiency, and the latter is the attenuation factor due to linear absorption μ throughout the crystal. Here α is interpreted as the angular variation of the diffracting planes over the extinction length (in unit of Darwin width) and can be expanded as

$$\alpha = \frac{\pi|\beta|}{2\beta_c} = \frac{\Omega {\Lambda_0}^2}{T_0 d_{hkl}} \tag{1.34.}$$

Thereby, the reflectivity becomes

$$r_{curved} = \left[1 - e^{\left(\frac{-\pi^2 T_0 d_{hkl}}{\Omega {\Lambda_0}^2}\right)}\right] e^{\left(\frac{-\mu T_0}{\cos\theta_B}\right)} \tag{1.35.}$$

It is worth noting that there are two main differences between diffraction properties of mosaic and CDP crystals. Firstly, perfect crystals thicker than the extinction length and mosaic crystals suffer a maximum diffraction efficiency of 50% because of re-diffraction of the incident beam onto lattice planes (Fig. 1.6a). Conversely, curved crystals prevent this

effect due to continuous change of the incidence angle so that only a single diffraction occurs onto curved crystalline planes (Fig. 1.6b). Hence, diffraction efficiency in CDP crystals can ideally reach the unity. Secondly, unlike for mosaic crystals, which normally exhibit a Gaussian-like reflectivity passband, a curved crystal offers a continuum of possible diffraction angles over a finite range, leading to a rectangular-shape energy passband directly owing to its curvature.

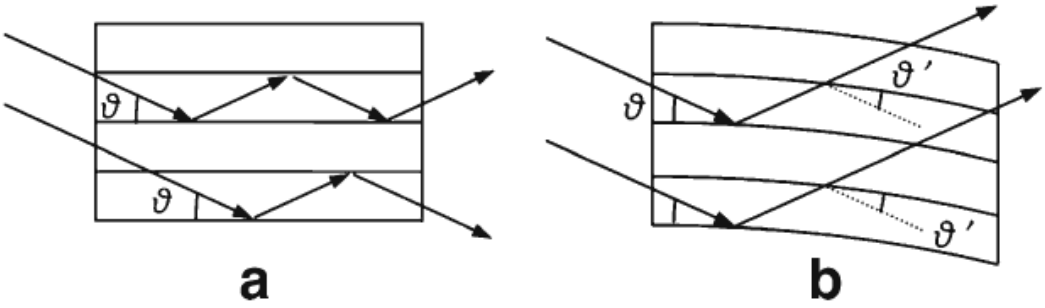

Figure 1.6: X-ray diffraction in Laue geometry in case of an unbent (a) and of a bent crystal (b). Multiple reflections in case (a) results in maximum 50% diffraction efficiency while in case (b) diffraction efficiency can reach 100% [1.17].

1.3. References

[1.1] W. H. Zachariasen, *Theory of X-ray Diffraction in Crystals*. New York: J. Wiley and Sons, (1945) and references therein

[1.2] H. Halloin and P. Bastie, *Exp. Astron*. **20**, 151–170 (2005) and references therein

[1.3] P. F. Fewster, *X-ray Scattering from Semiconductors*, London: Imperial College Press (2003)

[1.4] A. Authier, *Dynamical Theory of X-ray Diffraction*, Oxford University Press (2001).

[1.5] J. E. Ayers, *Heteroepitaxy of semiconductors: Theory, Growth and Characterization*, CRC Press (2007).

[1.6] M. von Laue, *Munchener Sitzungsberichte*, 363 (1912)

[1.7] M. von Laue, *Ann. der Phys*., **41**, 989 (1913)

[1.8] W. H. Bragg and W. L. Bragg, *Proc. Roy. Soc. London*, **88**, 428 (1913)

[1.9] W. H. Bragg and W. L. Bragg, *Proc. Roy. Soc. London*, **89**, 246 (1913)

[1.10] P.P. Ewald, *Phys. Zeitschr*., **14**, 465 (1913)

[1.11] D. T. Cromer and J. T. Waber, in *International Tables for X-ray Crystallography*, Kynoch Press, Birmingham, **4**, 71-147 (1974)

[1.12] C. G. Darwin, *The theory of X-ray reflexion*, Part I. Philosophical Magazine **27**, 315-333 (1914a)

[1.13] C. G. Darwin, *The theory of X-ray reflexion*, Part II. Philosophical Magazine **27**, 675-690 (1914b)

[1.14] N. Barriere et al., *J. Appl. Crystallogr*. **42** (5), 834 (2009)

[1.15] C. G. Darwin, *The reflexion of X rays from imperfect crystals*, *PhilosophicalMagazine*, **43**, 800-829 (1922)

[1.16] N. Barriere et al., *J. Appl. Crystallogr*. **43**, 1519 (2010)

[1.17] V. Bellucci et al., *Exp. Astron*. **31**, 45-58 (2011)

[1.18] V. Guidi et al., *J. Appl. Cryst*. **44**, 1255–1258 (2011)

[1.19] V. Bellucci et al., *Il Nuovo Cimento*, **34** C , 503-511 (2011)

[1.20] R. Camattari et al., *Experimental analysis and modeling of self-standing curved crystals for focusing of x-rays*, submitted (2012).

[1.21] I. Neri et al., *Proceeding of Spie*, 844334, doi:10.1117/12.926191 (2012)

[1.22] V. Guidi et al., *accepted for publication in Nucl. Instrum. Meth. B* (2013)

[1.23] C. Malgrange, *Cryst. Res. Technol*. **37**, 654 (2002)

[1.24] P. Penning and D. Polder, *Philips Research report*, **16**, 419-440 (1961)

[1.25] N. Kato, *Journal of the Physical Society of Japan*, **18**, 1785-1791 (1963)

[1.24] P. Penning and D. Polder, Philips Research report, **16**, 419-440 (1961)

[1.25] N. Kato, Journal of the Physical Society of Japan, **18**, 1785-1791 (1963)

2. Equipment for measuring diffraction patterns

2.1. High-resolution X-ray diffractometer (HRXRD)

At Sensors and Semiconductor Laboratory (SSL, Ferrara, Italy), a high-resolution X-ray diffractometer (HRXRD, X'Pert Pro MRD XL PANalytical^{TM}) has been used for structural characterization of semiconductor crystals and ceramic materials.

The instrument, as illustrated in Fig. 2.1, consists of basic features: an X-ray source, incident beam conditioning, sample stage and diffracted beam optics. The nature of these features have to be selected to best meet the needs of the material property to be analyzed.

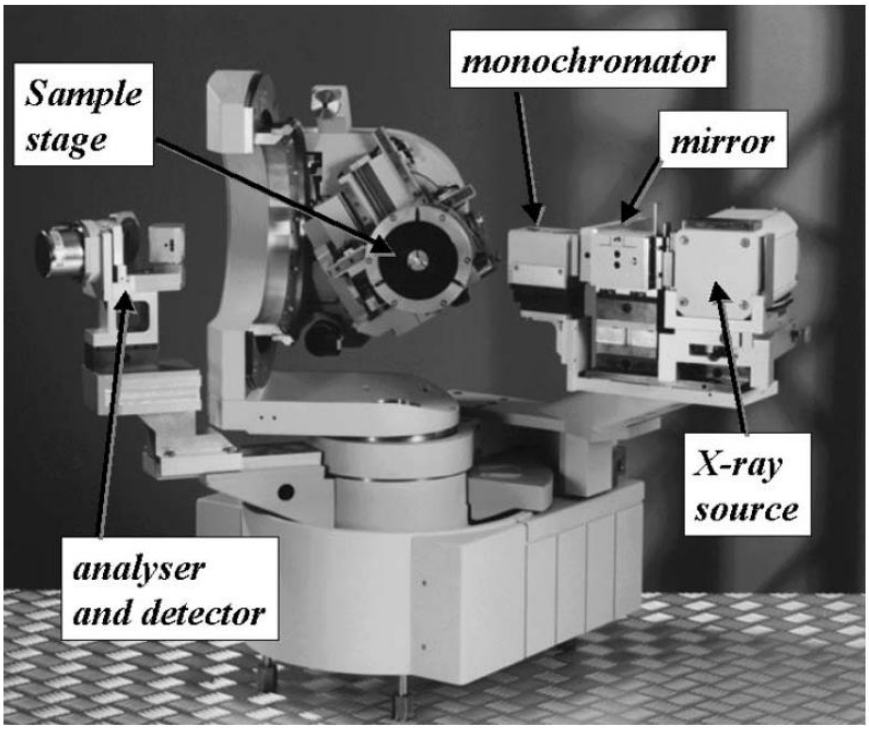

Figure 2.1: the high-resolution X-ray diffractometer at SSL (Ferrara, Italy) [2.1].

2.1.1. X-ray source

In a laboratory source of X rays, i.e., X-ray tube (see Fig. 2.2), photons are generated by electron energy transitions to the innermost electron orbitals in a solid and are characteristic of the atom concerned. The emission lines arise from excitations that transfer sufficient energy to remove an inner electron and allow the more loosely bound to transfer to the vacant inner states. As with any vacuum tube, there is a cathode, which emits electrons into the vacuum and an anode to collect the electrons, thus establishing a flow of electrical current, known as the beam, through the tube. A

high voltage power source, for example 30 to 150 kV, is connected across cathode and anode to accelerate the electrons. The X-ray spectrum depends on the anode material and the accelerating voltage.

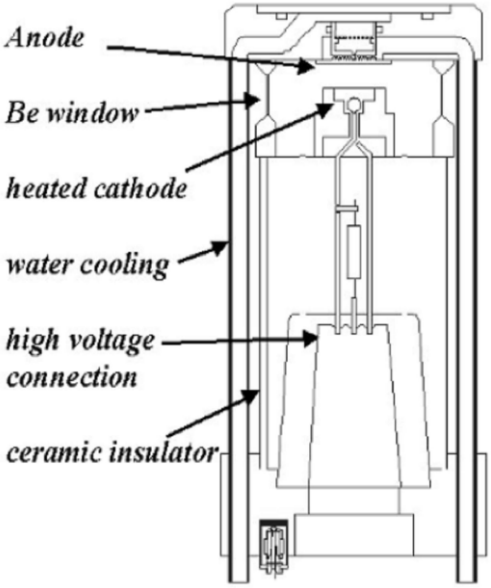

Figure 2.2: sketch of X-ray tube.

For the diffractometer under study, the material of the anode is copper, thus generating a spectrum of radiation as shown in Fig. 2.3.

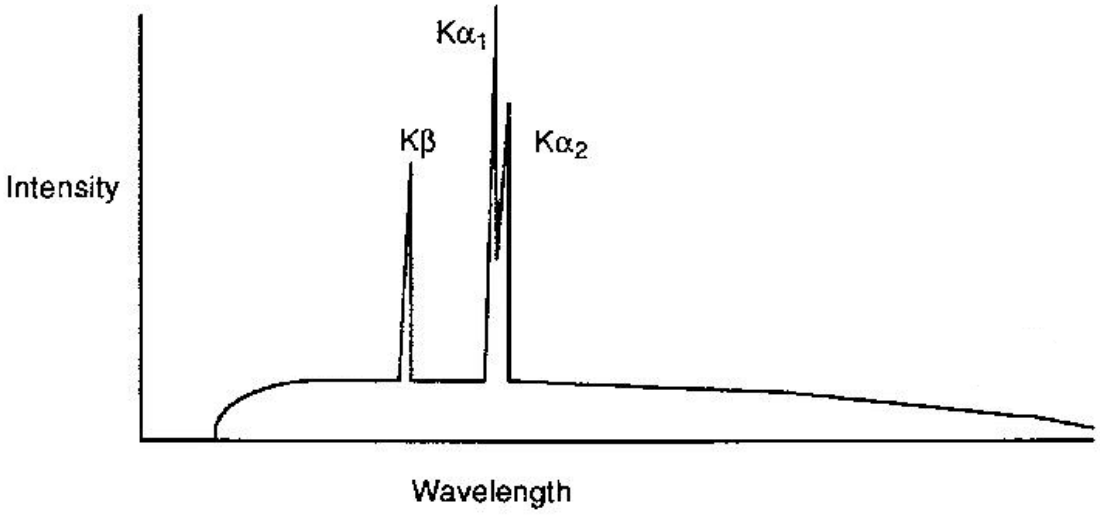

Figure 2.3: the Cu radiation spectrum.

For maximum intensity of the beam and focus stability, typical values of voltage and current are 45 kV and 40 mA, respectively.

The filament of the X-ray tube is a small linear coil and its dimension partially defines the focus, being approximately rectangular in shape. The advantage of this shape is that the projection normal and parallel to the long axis produces two very useful configurations of the X-ray source (see Fig. 2.4), i.e., line and point focus. Depending on the geometry of the focus of the anode, the thermal load from high-energy electrons impacting onto the anode can be very high, therefore, a balance between focus size and power is strictly necessary. Nevertheless, efficient cooling is used for correct operation of the X-ray tube.

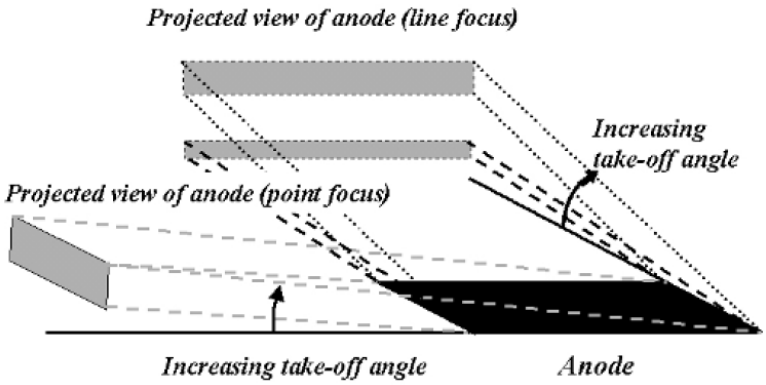

Figure 2.4: the different projections available from the HRXRD [2.1].

2.1.2. Incident beam conditioning

2.1.2.1. Incident beam slits and filters

In order to reduce the divergence of the X-ray beam, thus the irradiated length of the sample under analysis, incident beam slits with variable size are normally used during measurements. Indeed, divergence slits are fitted in the incident beam path to control the equatorial divergence of the beam and thus the amount of sample that is irradiated by the X-ray beam. In particular, the size of the divergence slit can be set to one of these fixed values: $1/2\,°, 1/4°, 1/16°$ and $1/32°$. Moreover, it is also possible to adjust the beam size by means of two knobs within the accessory "Crossed Slits Assembly". The knobs, one vertical and one horizontal, allow a gap of the aperture between 0 and 10 mm to be set. The knob scales are graduated in steps of 20 µm, thereby a size of the beam as small as 20×20 µm^2 can be achieved. The knob nearest to the X-ray tube controls the width of the beam while the knob furthest away from the tube controls the height of the beam.

In order to prevent the saturation of the detector due to a high photon flux, especially when the detector is positioned along the path of direct beam, absorbing filters or automatic beam attenuator placed in front of the X-ray source are required. However, by placing an absorbing material of an appropriate thickness, that has an absorption edge very close to the characteristic radiation of the X-ray tube, the spectral distribution can be dramatically changed, thus improving working operation of the whole diffractometer. In fact, as seen in Fig. 2.3, the X-ray source has several characteristic peaks due to the $K\alpha$ doublet and a complex $K\beta$ line though with lower intensity. Because several radiation peaks may add complications to diffraction patterns of samples

under analysis, the filter must be chosen in such a way that its elemental material has an absorption edge just on the high side of the $K\beta$ line. In particular, for the Cu anode tube, nickel fits the requirement, so that the $K\beta$ line is almost completely eliminated but also the broad white radiation is reduced and a sharp absorption edge can be seen.

A parabolic X-ray mirror (see Fig. 2.5), just positioned after the filter, enhances the performance because it parallelizes the beam from the focus by accepting nearly 0.8° of divergence and thus the Cu $K\beta$ is virtually eliminated (only 0.5% diffracted).

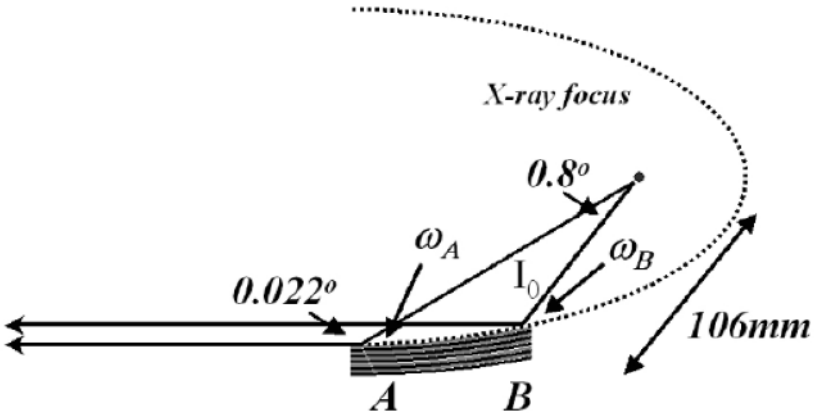

Figure 2.5: sketch of the parabolic X-ray mirror.

On the other hand, the energy difference in the $k\alpha$ doublet is small, thus high-energy resolution is required to separate these contributions. With this aim, a high-resolution crystal monochromator is used, its features being described in the following section.

2.1.2.2. Monochromator

Depending on the geometry of the tube, i.e., either line or point focus, the monochromator (see Fig. 2.6) of the HRXRD uses four symmetric 220 or 440 reflections from two channel-cut Ge crystals with (110) faces.

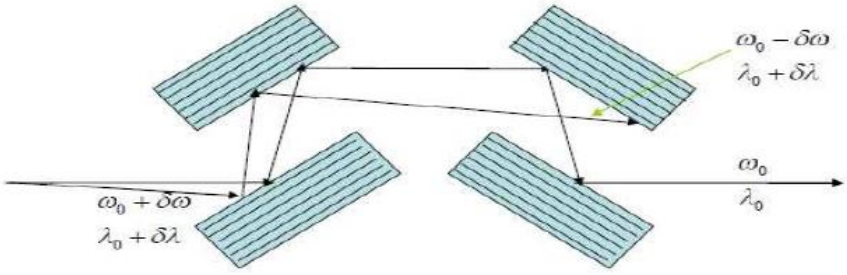

Figure 2.6: scheme of the Bartels monochromator

The beam is just conditioned by four diffracting crystals arranged according to the so-called Bartels monochromator. Indeed, as depicted in Ref. [2.2], each of the crystals acts as a double-crystal diffractometer in the (+, –) configuration. In the first channel-cut crystal, the first reflection passes a wide range of wavelengths, but each wavelength is diffracted at a particular angle. The

second reflection accepts this entire wavelength spread, but bends the beam back into line with the source beam. The third reflection (from the first surface of the second channel-cut crystal) can accept a narrow piece of this spectrum, because this crystal is antiparallel with the second and its acceptance angle for a particular wavelength is approximately the Darwin width for this reflection. The fourth reflection brings the beam back into the line of the source beam. Therefore, the monochromator produces a conditioned beam with a divergence and wavelength spread that are both determined by the Darwin width of the reflections from the channel-cut crystals.

In particular, by using Ge 440 reflections, the conditioned beam exiting the monochromator has a divergence of few arcsec and a monocromaticity of about $\delta_\lambda/_\lambda \approx 5 \times 10^{-5}$.

2.1.3. Sample stage

The sample stage of the HRXRD is a goniometer having optical encoders on the axes, leading to angular resolution of about 10^{-4} degrees. The angles associated with the diffractometer movements are shown in Fig. 2.7.

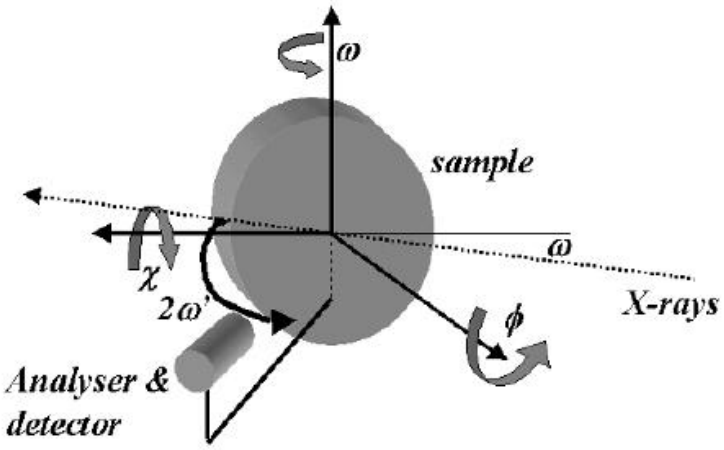

Figure 2.7: angles associated with the HRXRD movements [2.1].

The χ tilt axis allows for 180° rotation and the ϕ rotation axis, being normal to sample surface, can rotate through 360°. Sample can also be translated by xyz stage. The $2\omega'$ angle has a defined zero angle related to the direction of incident beam, while the ω angle can be conveniently be defined with respect to sample surface, this latter supposed to be flat.

2.1.4. X-ray detector

To reveal the energy of incident photons, the X-ray diffractometer at SSL uses a proportional gas counter, which is one of the most reliable detectors capable to record every X-ray photon and produce a measurable signal proportional to the flux of photons over a large range. Its scheme is shown in Fig. 2.8 and the working principle is the following: in a proportional counter the fill gas of the chamber which is usually an inert gas, to prevent rections, is ionised by incident radiation.

Indeed, an ionizing particle entering the gas collides with a molecule of the inert gas and ionises it to produce an electron and a positively charged atom, commonly known as an "ion pair". As the charged particle travels through the chamber, it leaves a trail of ion pairs along its trajectory, the number of which is proportional to the energy of the particle if it is fully stopped within the gas.

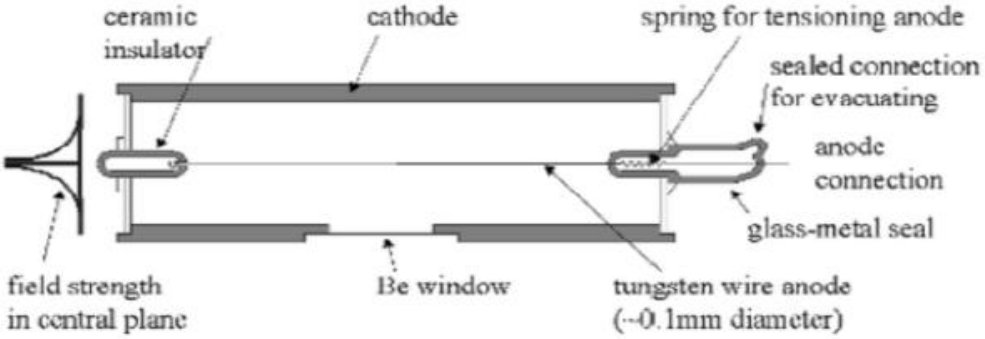

Figure 2.8: the proportional gas detector. The incoming photon impinges onto an X-ray transparent Be window and ionizes the gas inside the chamber. Electrons and ions are accelerated by an intense electric field towards the anode and cathode, respectively, creating further impact ionization events and thus an electric signal being proportional to the energy of the incoming photon [2.1].

Indeed, to obtain a highly efficient counter, the absorption of X-ray photons must occur within the chamber and this fact partially determines the choice of the inert gas. In particular, for the case of the HRXRD at SSL, a gas of Xe is employed, giving about 93% of absorption efficiency for X rays coming from the Cu X-ray tube. Further advantage of the usage of Xe as inert gas is the creation of electrons owing to Auger process, which is the favoured absorption mechanism for reliable counting. Finally, one of the most important aspects of any detector is the relationship between the signal and the incoming photon flux. Fig. 2.9 highlights the good energy resolution of the detector, for a stable and proportional response.

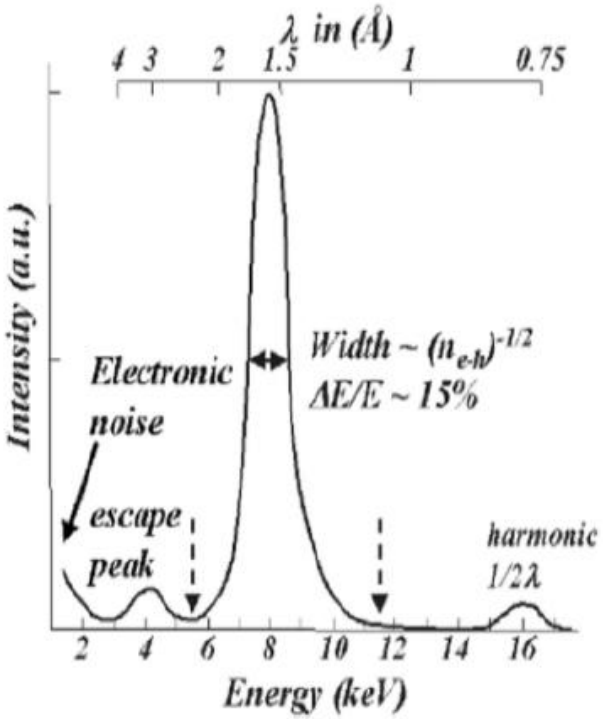

Figure 2.9: the energy distribution for discriminating Cukα X rays with the proportional detector [2.1].

.

2.1.4.1. Combination with scattered beam analyzer

In order to reduce the angular acceptance of X-ray beam scattered from sample, thus increasing the instrumental resolution, an analyzer crystal is positioned between sample and detector. The analyzer consists of two channel-cut Ge (220) crystals oriented in such a way to diffract the beam from the specimen, with an angle of acceptance equal to the Darwin width of the crystals. Indeed, by selecting only parallel X rays scattered from the sample, i.e., those which satisfy the Bragg condition for the analyzer, the angular acceptance is significantly reduced. The scheme of the analyzer is depicted in Fig. 2.10.

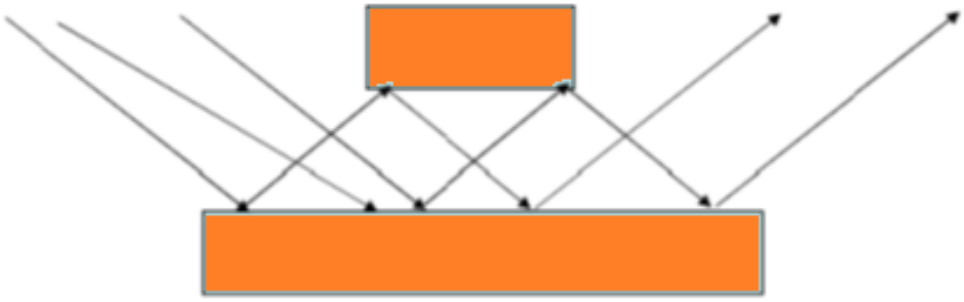

Figure 2.10: scheme of the analyzer crystal made by two channel-cut Ge (220) crystals. The beam undergoes three internal reflections within the analyzer before entering the detector. Indeed, odd numbers of reflections reduces the chance of the directly scattered beam from reaching the detector. Only X-rays which satisfy Bragg condition for the analyzer will enter the detector. For the analyzer of the HRXRD acceptance angle is about 11 arcsec.

A further method of controlling the divergence of the scattered beam is the usage of a parallel-plate collimator as analyzer (see Fig. 2.11). In this case, the advantage is that small divergence can be preserved while still maintaining high intensity of photons by using a large X-ray source. Capture of scattering from large regions on the sample is allowed, and this method is often used in applications of thin film analysis, where very low angle of incidence are required, or powder diffraction.

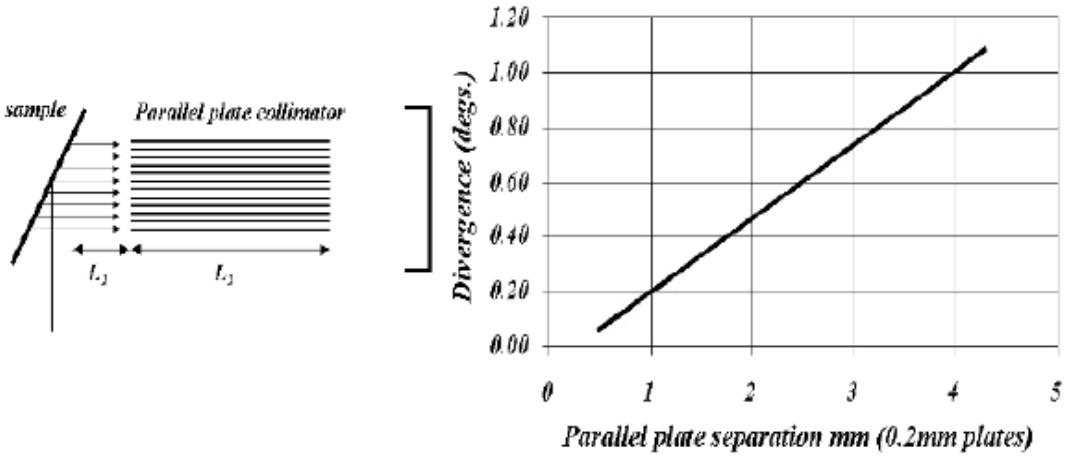

Figure 2.11: on the left side, sketch of the parallel-plate collimator while the right side shows the variation of divergence as a function of the separation between plates [2.1].

2.1.5. Configuration of the HRXRD for characterization of samples by rocking curve

The *rotating crystal method*, which has been described in previous chapter (section 1.1.2.), represents the basis of X-ray characterization of samples at SSL by rocking curve (RC) measurement. Indeed, a RC measurement involves rotating the specimen in the monochromatic X-ray beam in order to plot the diffracted intensity as a function of the incidence angle of the beam.

The configuration of the HRXRD for measuring a RC, thus a diffraction profile of the sample under analysis, is depicted in Fig. 2.12.

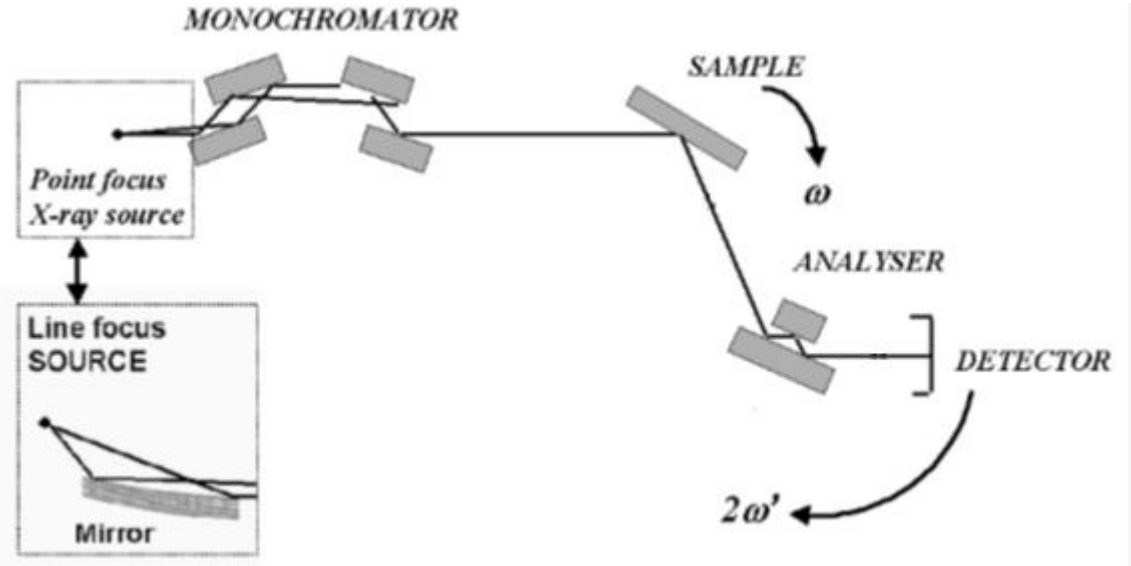

Figure 2.12: configuration of the high-resolution X-ray diffractometer at SSL for measurement of a RC of sample in Bragg geometry with respect to incident beam.

Either point or line focus can be used as geometry of the X-ray source. Because in line focus configuration the divergence is higher than for point focus, the X-ray mirror is required to parallelize the beam. Then, the monochromator controls the scattering plane divergence and wavelength dispersion, producing a well-defined incident beam. The analyzer crystal only passes scattered X rays coming from the sample in the specific direction defined by its rotation about an axis common with the sample rotation. However, it is worth noting that depending on the application of the specimen under analysis, the analyzer can be used or not, this latter case being the so-called open detector mode. As an example, with the aim to reveal mosaic crystallites in an imperfect sample, the introduction of the analyzer crystal before the detector allows for scanning along the direction normal to the plane that is sensitive to strain, because it selects only parallel X rays coming from the sample. Therefore, it results possible to separate the mosaic block orientation from other contributions of imperfections of the specimen, e.g., bending, strain variation and intrinsic scattering, consequently revealing mosaicity of the sample. On the other hand, an open detector scan would result in a very broad profile, many times that of the intrinsic scattering profile of the sample, because all contributions are mixed, the major contributing factor to the width of an open detector scan being normal to this direction. In Fig. 2.13, RCs obtained with the HRXRD show the difference between a scan in open detector mode and that with an analyzer.

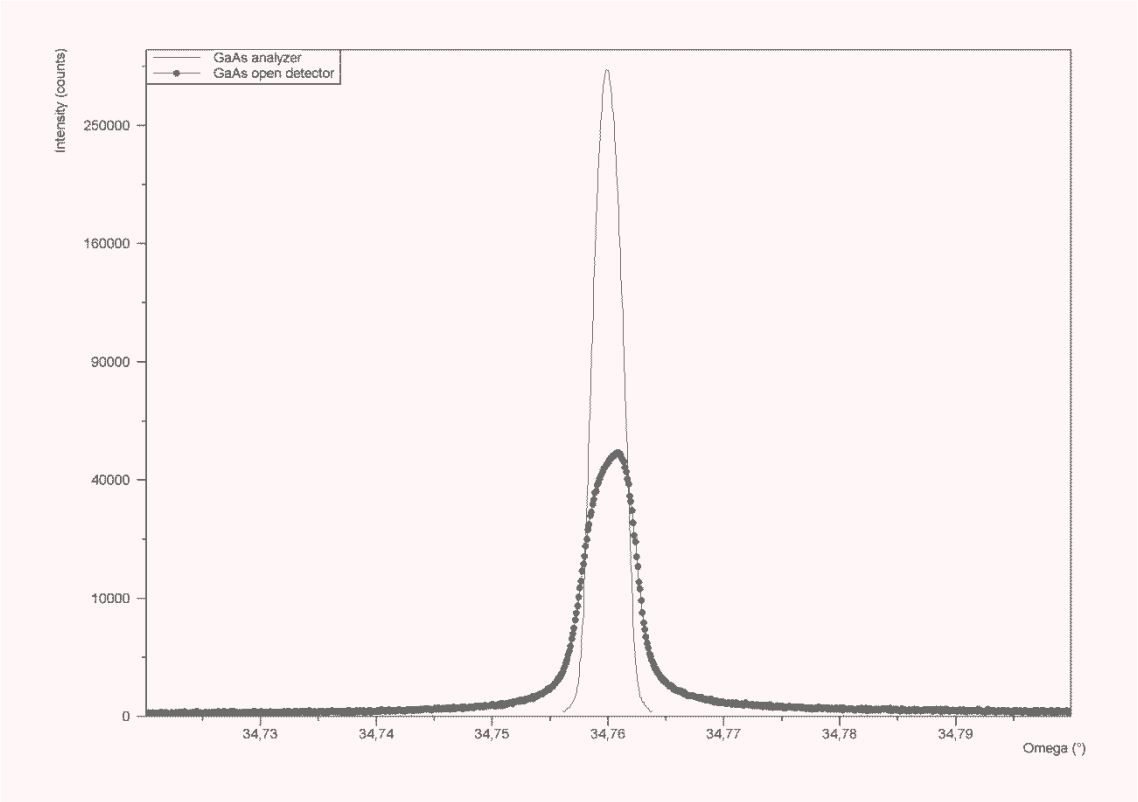

Figure 2.13: RCs obtained on a GaAs sample in open detector mode (black dotted line) and with analyzer (black line) by using the HRXRD at SSL.

2.2. Beamline ID15A at European Synchrotron Radiation Facility (ESRF)

At European Synchrotron Radiation Facility (ESRF, Grenoble, France, see Fig. 2.14), beamline ID15A has been used to carry out experiments of X-ray diffraction on curved crystals of Si and Ge material.

The working principle of synchrotron light source is very different from that of an X-ray tube. A synchrotron is a storage ring for electrons, which are contained by magnetic fields to prevent excessive divergence and consequent energy loss. When the electrons are deviated from a straight line using auxiliary components such as bending magnets and insertion devices (undulators or wigglers), the consequent acceleration towards the centre of the curve creates an energy orbital jump thus producing electromagnetic radiation. If this energy change is large, then X rays can be produced. The X-rays from the synchrotron are emitted tangentially from the radius and concentrated into a narrow cone with the electric field vector predominately confined to the plane of the orbit, i.e., the beam is horizontally polarised.

Figure 2.14: European Synchrotron Radiation Facility (Grenoble, France)

On beamline ID15A, high energy, high flux and flexibility in the energy tuning are well combined with significantly high spatial and spectral beam definition. For X-ray characterization of curved Si and Ge crystals, a highly monochromatic and quasi-parallel beam (50×50 μm^2 or 100×50 μm^2) was tuned to the desired energy, ranging from 150 to 700 keV. This was done thanks to a two-reflection Laue Si (111) unbent monochromator with a sharp monochromaticity of the order of $\Delta E/E = 2 \times 10^{-3}$. A high-purity Ge detector was used to reveal X rays. The beam intensity was constantly monitored by the current of electrons in the storage ring of the synchrotron. The experimental setup at beamline ID15A is shown in Fig. 2.15.

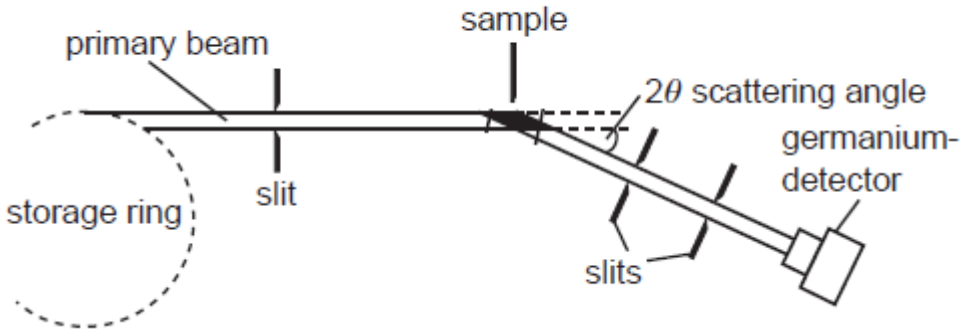

Figure 2.15: experimental set-up at the beam line ID15A at the ESRF

The characterization of the samples was carried out by performing RCs in Laue geometry, i.e., by recording either the transmitted or diffracted beam intensity while the crystal was rotated in the beam around the position where the Bragg condition is satisfied. Transmitted beam intensity was recorded by keeping the sample in diffraction condition and shifting the detector in such a way to measure the beam intensity passing through the crystal without undergoing diffraction. Moreover, the sample holder was set far enough from the detector in order to allow for sufficient separation of diffracted and transmitted beams even at highest energy. Diffraction and transmission RCs were recorded one after the other, resulting in two complementary curves as a function of the beam incidence angle (Fig. 2.16). An advantage of this configuration is that diffracted and

transmitted RCs exhibited diffraction efficiency of the sample under analysis. Efficiency is defined as in Ref. [2.3, 2.4] (see also chapter 1), namely the ratio of diffracted beam intensity over the transmitted one.

The FWHM of the RC is a direct measurement of the angular distribution of diffracting planes (hereinafter referred to as angular spread), namely the bending angle of the crystal. In Laue geometry the Bragg angles are small and therefore a possible broadening of the RCs due to a variation of the lattice parameter can be negligible. Furthermore, the shape of the RCs was not modified by extinction phenomena, which were negligible in such curved crystals.

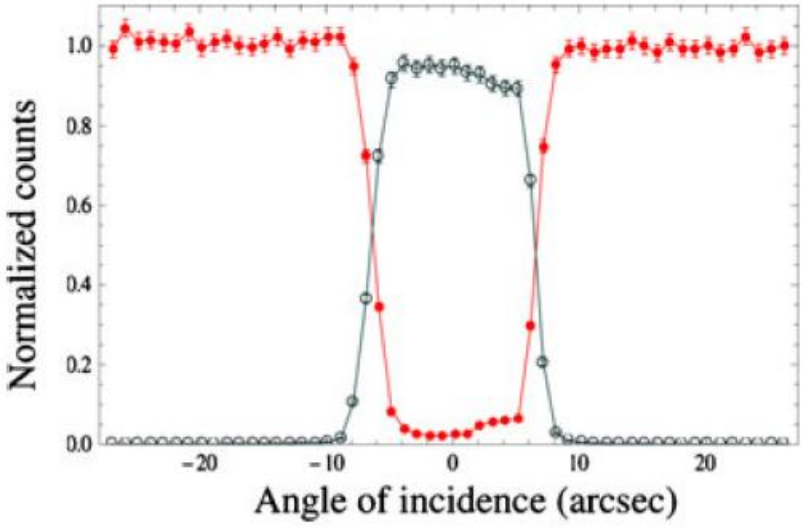

Figure 2.16: RCs obtained at beamline ID15A on a Si CDP crystal [2.5]. The energy of the photon beam was 150 keV. Filled circles plot the intensity of the transmitted beam, whereas the empty circles plot the intensity of the diffracted beam. The FWHM of the RCs is of the order of crystal bending.

2.3. Hard X-ray diffractometer at Institute Laue Langevin (ILL)

At Institute Laue Langevin (ILL, Grenoble, France) X-ray characterization on two stacks of Si curved crystals has been carried out by using a hard X-ray diffractometer (see Fig. 2.17) based on the method of X-ray focusing for transmission (Laue) geometry [2.6-2.9]. A schematic diagram of this technique is shown in Fig. 2.18. The diffractometer uses a polychromatic and divergent X-ray beam (energy range between 80 and 450 keV) emitted from a high-voltage and fine-focus X-ray tube commonly used for industrial radiographs. Since Bragg angles were small (0.5 – 1 degree), diffraction peaks were located close to the direct beam, thus allowing the observation of peaks from several crystallographic planes. These latter were observed thanks to a high-resolution and sensitive X-ray image intensifier coupled with a CCD camera, featuring a spatial resolution of about 0.35 mm (pixel size).

For the experiment on curved Si multi-crystals, the distance between sample and generator focus, this latter being 1×1 mm^2, was set to be 4.45 m, thus determining a lattice tilt maximum

sensitivity of 8.1 arcsec. Moreover, a slit with variable size positioned just before the sample delimited the width of the X-ray beam.

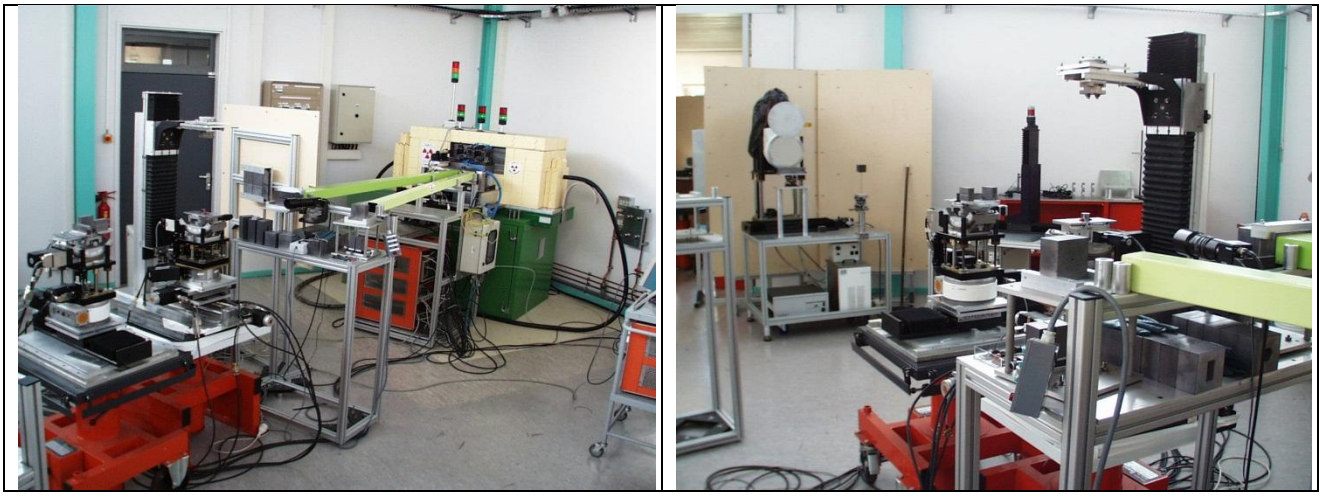

Figure 2.17: left side: X-ray generator and diffractometer. Right side: sample orientation table and detector.

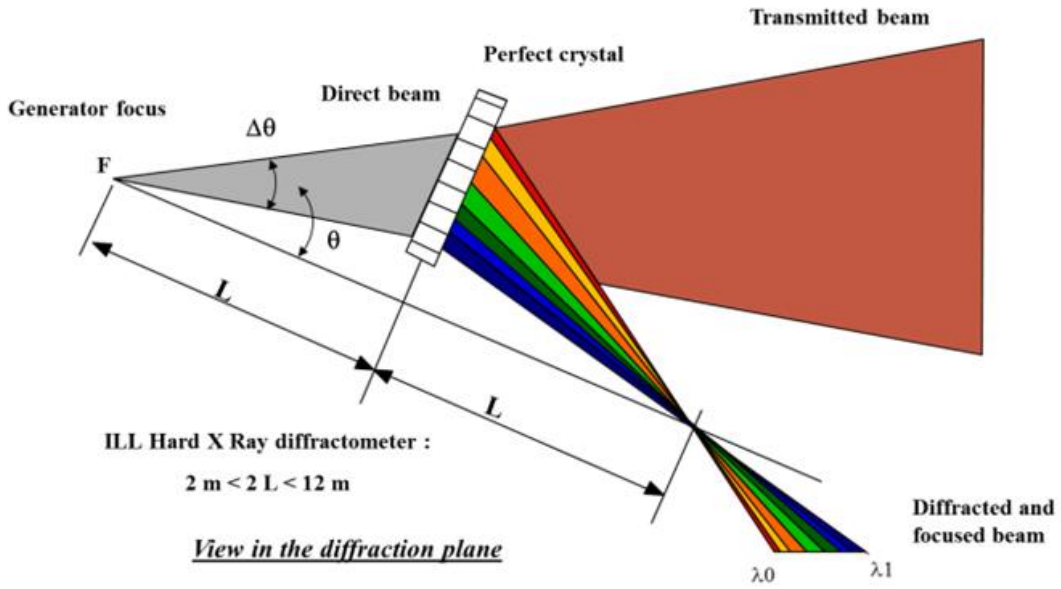

Figure 2.18: schematic representation of the in-plane focusing of a divergent polychromatic x-ray beam by a crystal in Laue geometry. If the distance from the source to the crystal is equal to that from the crystal to the focal point, all diffracted rays converge to a point and a distribution of wavelengths is selected [2.10].

Under the assumptions highlighted in Ref. [2.11], for a diffractometer based on the method of X-ray focusing in Laue geometry with a divergent and polychromatic beam, all diffracted rays converge to a point (Fig. 2.18) and a distribution of wavelengths from the white beam is selected. The focusing effect only occurs in the scattering plane while in the perpendicular direction the radiation propagates straight. In fact, scattering from a perfect thin crystal will result in a line profile onto a detector located at the focusing position. The FWHM of the intensity Gaussian profile perpendicular to the line is solely determined by the size of the X-ray source and the thickness of the crystal. Conversely, for a curved crystal the width of the intensity profile is also related to the

deformation of diffracting planes, i.e., to its bending angle [2.5]. In particular, from a crystal with CDP the width of a converging or diverging beam at the detector (small-angle approximation) is given by

$$\delta = a + \left|\left(2t\theta_B + t\theta_B \pm f\frac{l}{R}\right)\right| \qquad 2.1.$$

where the ± sign holds for the converging or diverging mode of diffraction, a is the size of the X-ray source, t is the thickness of the crystal (traversed by radiation), f is the sample-to-detector distance, l is the length of the crystal which undergoes bending and R is the curvature radius of the crystal. The term $2t\theta_B$ is the contribution of broadening due to the thickness of the sample, $t\theta_B$the broadening due to the variation of incidence angle while $f\frac{l}{R}$ represents the bending contribution. This result has been obtained by revisiting the formulas of the focal spot size in Refs. [2.11, 2.12].

A typical diffraction pattern produced by the hard X-ray diffractometer is shown in Fig. 2.19.

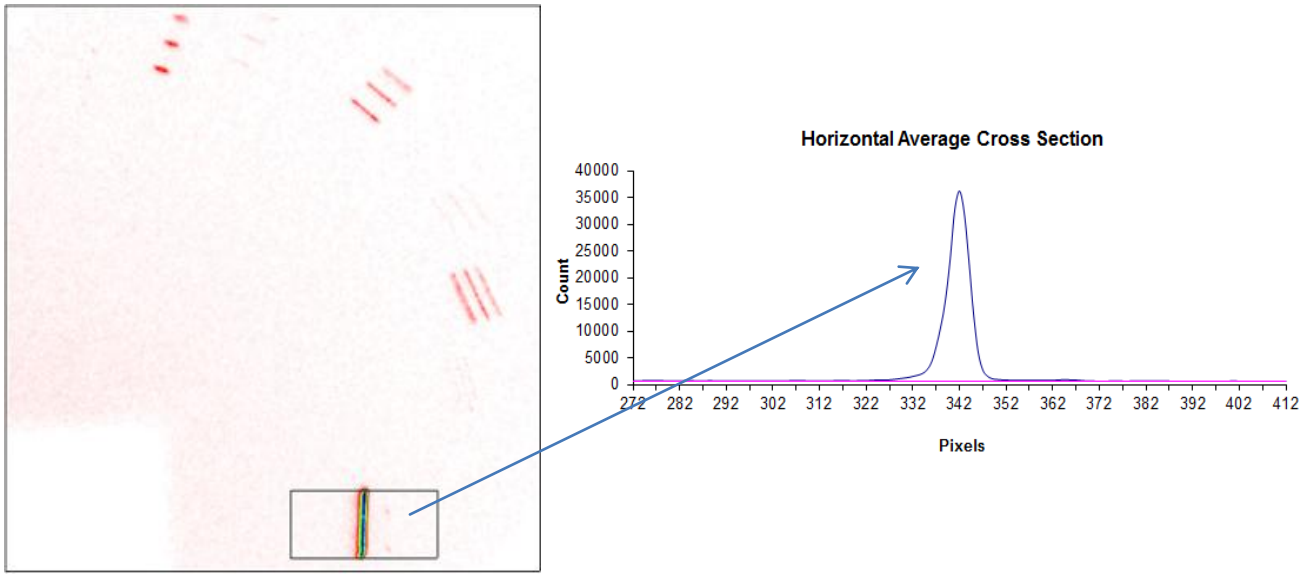

Figure 2.19: Diffraction patterns recorded from a Si crystal with CDP (a). Horizontal average cross-section of the focal spot corresponding to (111)-diffraction is highlighted (b).

2.4. References

[2.1] P. F. Fewster, *X-ray Scattering from Semiconductors*, London: Imperial College Press (2003)

[2.2] J. E. Ayers, *Heteroepitaxy of semiconductors: Theory, Growth and Characterization*, CRC Press (2007)

[2.3] A. Authier, *Dynamical Theory of X-ray Diffraction*, Oxford University Press (2001).

[2.4] N. Barriere et al., *J. Appl. Crystallogr*., **42** (5), 834 (2009)

[2.5] V. Bellucci et al., *Exp. Astron*., **31**, 45-58 (2011)

[2.6] A. Guinier, J. Tennevin, *Acta Crystallogr*. **2**, 133-138 (1949)

[2.7] P. Bastie and B. Hamelin, *J. Phys. IV*., **6**, (1996)

[2.8] B. Hamelin and P. Bastie, *J. Phys. IV*., **8**, 3-8, (1998)

[2.9] B. Hamelin and P. Bastie, *Proceeding of Spie*, **5168**, 471-481 (2002)

[2.10] I. Neri et al., *Ordered stacking of crystals with adjustable curvatures for hard x- and gamma-ray broadband focusing*, submitted to *J. Appl. Cryst*., (2012)

[2.11] M. Stockmeier and A. Magerl, *J. Appl. Crystallogr*., **41**, 754-760 (2008)

[2.12] M. Th. Rekveldt, *Nucl. Instrum. Meth*., **215**, 521-527 (1983)

3. X-ray characterization of curved Si and Ge crystals for realization of a Laue lens

3.1. A Laue lens for astrophysics

A Laue lens is an optical component to focus hard X- and soft gamma-ray photons through Bragg diffraction in Laue geometry within a properly arranged array of crystals disposed as concentric rings with radii spanning a certain range [3.1-3.3] (see Fig. 3.1). For a Laue lens a significantly important field of application is represented by astrophysics. In fact, in hard X-ray astronomy many celestial sources emitting high-energy photons are very interesting candidates for investigation. As an example, a hot topic in astrophysics that may benefit from usage of a Laue lens is high-precision mapping of celestial positron sources [3.4], through the study of the e+ - e− annihilation line at 511 keV. Despite a 511 keV emission has been observed for more than 30 years towards the Galactic center [3.5], the origin of the positrons still remains a mystery. Stellar nucleosynthesis [3.6-3.8], accreting compact objects [3.9-3.12], and even the annihilation of exotic dark matter particles [3.13] have all been suggested, thus a deeper investigation has to be done. A Laue lens would enable the study of the location of positron sources in our Galaxy by concentrating the annihilation line at 511 keV with high resolution, thus bringing new clues concerning these still elusive sources of antimatter. As another, the focalization of 847-keV photons produced by the decay chain of the radionuclide 56Ni would enable the study of Type Ia Supernovae events, thus unveiling the physical processes in these cosmological standard candles [3.14].

It is widely acknowledged by the scientific community that a Laue lens would achieve a gain in sensitivity by one or two orders of magnitude with respect to existing telescopes in the hard X-ray/soft gamma-ray domain (>100 keV). In fact, in order to improve our knowledge of the violent celestial processes responsible of the emission of high-energy photons more sensitive telescopes are needed. Current instruments operating in this part of the electromagnetic spectrum do not use focusing optics. They reconstruct the incidence direction of detected events thanks to either an aperture modulation (coded mask) or by tracking the multiple (Compton) interactions of photons in a sensitive volume [3.15]. The common point of these two techniques is that the signal is collected onto an area which is itself the sensitive area. With the existing kind of telescopes more sensitive means larger in order to collect more signal. However, the improvement of sensitivity only scales with the square root of the collection surface since the instrumental background scales with the volume of detectors. This is why it appears impossible to achieve the required sensitivity leap of a factor 10-100 with the existing principles of soft gamma-ray telescopes. On the other hand, by concentrating photons from a large collection area of a crystal diffraction lens onto a very small detector volume, background noise would be extremely low leading to a significantly high gain in sensitivity.

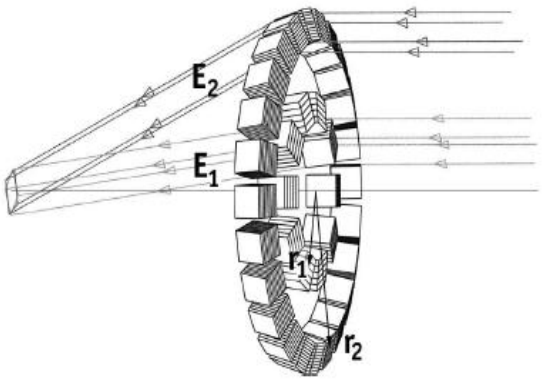

Figure 3.1: sketch of a Laue lens. X- and gamma-ray photons are diffracted by an array of crystals, disposed as concentric rings spanning a certain energetic range, towards a common focal point [3.15].

Since in most cases a Laue lens is requested to concentrate radiation over a broad energy range, a typical component for wide-passband focusing is a mosaic crystal [3.16]. However, this latter suffers a 50%-limit in diffraction efficiency. With this aim, crystals with curved diffracting planes (CDP) have been deeply studied as high-efficiency optical components for the realization of a Laue lens for satellite-borne experiments. CDP crystals exhibit a uniform energy distribution with a passband proportional to the curvature and their diffraction efficiency can ideally reach the unity [3.17, 3.18].

For fabrication of a CDP crystal, several techniques have been worked out. Bending can be accomplished by mechanical means, i.e., by deforming a perfect single crystal [3.19] through an external device. As an example, mechanically bent crystals have been used in synchrotrons for many years as high-efficiency monochromators. However, the usage of an external device leads to excessive weight, which is to be avoided especially in satellite-borne experiments with a Laue lens. Thus, self-standing CDP crystals are mandatory for practical implementation of a focusing telescope as a Laue lens. Such curved crystal can be produced by applying a thermal gradient to a perfect single crystal [3.20] but, this method is energy consuming and not adapted to a space-borne observatory as well. CDP crystals can also be obtained by concentration-gradient technique, i.e., by growing a two-component crystal with graded composition along the growth axis [3.20–3.23]. However, crystals bent by such a method are not easy to manufacture, this making the technique hardly applicable for a Laue lens application, for which serial production of crystals should be envisaged.

It was proven that a promising technique for bending crystals is surface grooving [3.24, 3.25]. Grooves manufactured on the surface of a crystal by a diamond saw induce a permanent curvature within the crystal, with no need for external device. This technique is based on plastic deformation of the crystal induced by the grooves. As a result of deformation, a permanent curvature is produced, resulting in self-standing CDP crystals. Such method is cheap, simple and very reproducible, thus compatible with mass production.

Within the framework of the "Laue project" as financed by the Italian Space Agency, at Sensor and Semiconductor Laboratory (SSL, Ferrara, Italy) silicon and germanium plates are plastically deformed by grooving one of their major surfaces with very good control of the curvature. Grooved crystals were characterized at ESRF (Grenoble, France) under X-ray diffraction experiments and exhibited significantly high performance up to 700 keV, peaking 95% at 150 keV [3.18]. Moreover, it resulted that measured angular spread of the diffracted beam was always very close to the morphological curvature of the sample under investigation, proving that the energy passband of CDP crystals can be controlled by simply imparting a selected curvature to the sample.

Next sections describe the possible arrangements of CDP crystals in a Laue lens, their fabrication through surface grooving technique and experimental results of X-ray characterization obtained on Si and Ge grooved crystals, showing their functionality as optical elements for a Laue lens.

3.2. Configurations of crystals in a Laue lens

For the sake of better understanding, some concepts about diffraction in curved crystals are reviewed.

CDP crystals are innovative for the realization of a Laue lens because they offer a continuum of possible diffraction angles, directly owing to their curvature. Thus, it becomes possible to diffract X-rays over a broad energy passband. According to dynamical theory of diffraction [3.26], their reflectivity can be significantly high [3.17, 3.18], being

$$r_{curved} = \left[1 - e^{\left(\frac{-\pi^2 T_0 d_{hkl}}{\Omega {\Lambda_0}^2}\right)}\right] e^{\left(\frac{-\mu T_0}{\cos\theta_B}\right)} \qquad 3.1.$$

where the first factor is for diffraction efficiency, and the latter is the attenuation factor due to linear absorption μ throughout the crystal. T_0 is the crystal thickness traversed by radiation, d_{hkl} the d-spacing of diffracting planes (hkl) and Ω the angular spread, i.e., the bending angle of the crystal. θ_B is the Bragg angle and Λ_0 the extinction length as defined in Ref. [16]. For curved Si (111) crystal with radius of curvature of the order of 10^2 meters, $T_0 \approx 1\text{cm}$ and photon energy of the order of 10^2 keV, a reflectivity about 70 - 80% can be obtained.

In Ref. [3.25], a model, which completely relies on the theory of elasticity, has been developed to predict the curvature of grooved samples, thus obtaining the appropriate value of Ω that maximizes the reflectivity of a Laue lens.

3.2.1. Geometry 1: stack of equally curved crystal plates

With the aim of wide-passband focusing, CDP crystals must be disposed vs. impinging photons as in Fig.3.2a, hereinafter called ”geometry 1”. In particular, in order to maximize diffraction efficiency of the whole lens, self-standing curved crystal plates thicker than some millimeters are required. However, realization of such thick CDP crystals is technologically demanding.

A possible solution can be a multi-crystal, i.e., a stack of equally curved crystal plates, aligned with each other with high accuracy (Fig. 3.2a) [3.27, 3.28]. In a Laue lens scheme, the stack should be positioned with the diffracting planes parallel to the major surface of the crystalline plate and perpendicular to the lens surface. Photons enter the stack nearly parallel to the diffracting planes, suffer diffraction and undergo focusing onto the detector. This technique opens up a viable way to build up optical components for X- or gamma-ray diffraction without any size constraint, which may be useful in Laue lens application, where weight constraint is mandatory.

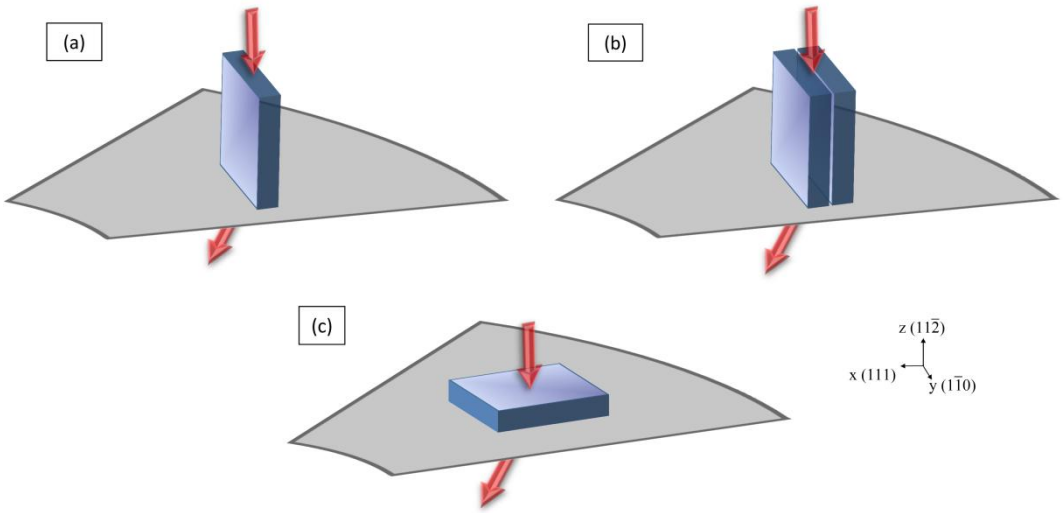

Figure 3.2: (a) Geometry 1. (b) A stack of plate-like curved crystals is proposed as an optical component for a Laue lens in geometry 1. (c) Geometry 2 with a quasi-mosaic crystal as optical element for focusing through a Laue lens. Arrows represent X-ray beam. In both geometries, curved diffracting planes are the (111) due to their high reflectivity.

3.2.1.1. Misalignment effects

Proper bonding of neighboring plates in a stack (Fig 3.3a) is mandatory to ensure a good alignment of the diffracting planes and thus a well-defined focal spot on the detector. In fact, neighboring plates can be affected by a misalignment with respect to each other as shown in Figs. 3.3b, c and d. With this regard, let us consider a parallel x-ray beam undergoing Laue diffraction from curved crystalline planes (parallel to the major surface of the plates), which are misoriented by a constant angle φ with respect to each other. In the case of Fig. 3.3b, if a photon with wavelength λ is diffracted at Bragg angle, θ_B, by one of the crystalline plates, another photon impinging onto the other plate at the same point is being diffracted provided that its wavelength is

$$\lambda' = \frac{\lambda \sin(\theta_B - \varphi)}{\sin \theta_B} \sim \lambda(1 - \varphi \cot \theta_B) \qquad 3.2.$$

where φ is the angle of misalignment between the plates under small-angle approximation. If instead one considers the misalignment as depicted in Fig. 3.3c, if a photon with wavelength λ is diffracted at θB by one of the crystalline plates, another photon impinging onto the other plate at the same point is being diffracted provided that its wavelength is

$$\lambda' = \frac{\lambda}{\cos \varphi} \sim \lambda \left(1 + \frac{\varphi^2}{2}\right) \qquad 3.3.$$

For the case of photons impinging onto the plates misaligned as in Fig. 3.3d, the relationship between wavelengths reads

$$\lambda' = \lambda \text{ for all } \varphi \qquad 3.4.$$

It turns out that misalignment is unimportant for an x-ray beam impinging as in Fig. 3.3d, less important for the configuration in Fig. 3.3c, while critical for the case in Fig. 3.3b. Therefore, for fabrication of a stack of plate-like curved crystals, special care must be paid to avoid this latter misalignment.

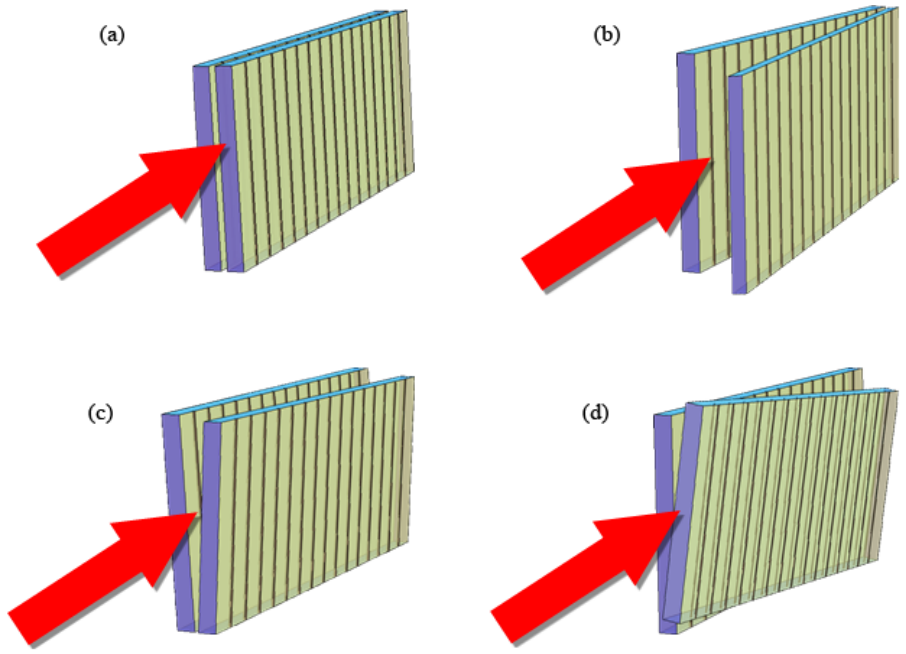

Figure 3.3: perfect bonding of neighboring plates in a stack is mandatory to ensure a good alignment of the diffracting planes and thus a well-defined focal spot on the detector (a). For a parallel x-ray beam (red arrow) undergoing diffraction from curved crystals with plates misoriented of an angle φ, the misalignment is critical (b), less important (c) and indifferent (d).

3.2.2. Geometry 2: quasi mosaic crystals

The "geometry 2" as in Fig.3.2c has been proposed in [3.29] because of the larger crystal surface exposed to the photon flux, which means fabrication of about 10^2 samples vs. 10^3-10^4 samples for geometry 1. The necessary curvature to yield CDP is provided by quasi-mosaic (QM) effect as a secondary curvature.

Quasi-mosaicity is an anisotropic effect that manifests itself when a properly oriented crystal plate is bent along a given direction, i.e., quasi-mosaicity depends on the crystallographic orientation of the plate undergoing bending. Indeed, a primary curvature imparted to a crystal results in a secondary (quasi-mosaic) curvature of a different plane direction due to the quasi-mosaic effect. The curvature induced by the phenomenon of quasi mosaicity has been studied in the framework of linear elasticity and can be predicted [3.29].

Historically, quasi-mosaicity was discovered by Sumbaev in a seminal work [3.30]. More recently, this phenomenon was introduced by Ivanov [3.31] to bend Si crystals for steering high-energy particles via coherent effects in crystals [3.32, 3.33].

The use of QM crystals allows positioning of the crystals in a Laue lens in the same way as for mosaic crystals, i.e., with the diffracting planes perpendicular to the major faces of the crystal (Fig. 3.4). However, in Ref. [3.29] it has been shown that the signal-to-noise ratio attained for QM crystals can be about an order of magnitude larger than that for mosaic crystals, highlighting the functionality of exploitation of QM crystals in efficient focusing of high-energy photons in a Laue lens.

For a Laue lens composed of crystals with diffracting planes perpendicular to the major face of the crystal, focusing can be fully provided by bending the crystals to a primary curvature equal to that of the whole lens. However, even for such a curved crystal, if the diffracting planes were perfectly flat, the reflectivity of the whole lens would be the same as that for an unbent single crystal, i.e., a relatively low figure. By using QM crystals, it is possible to combine the focusing action due to primary curvature with the high reflectivity of CDP built up by quasi-mosaicity. Due to quasi mosaicity, the photon flux can be focused down to a spot smaller than the size of the diffracting crystal, in contrast to diffraction by a traditional crystal, the spot of which is no smaller than its size exposed to the photons. Thus, since the size of the focal spot of the photons diffracted can be controlled by secondary curvature, QM crystals allow focusing with high resolution, increasing the sensibility of the Laue lens.

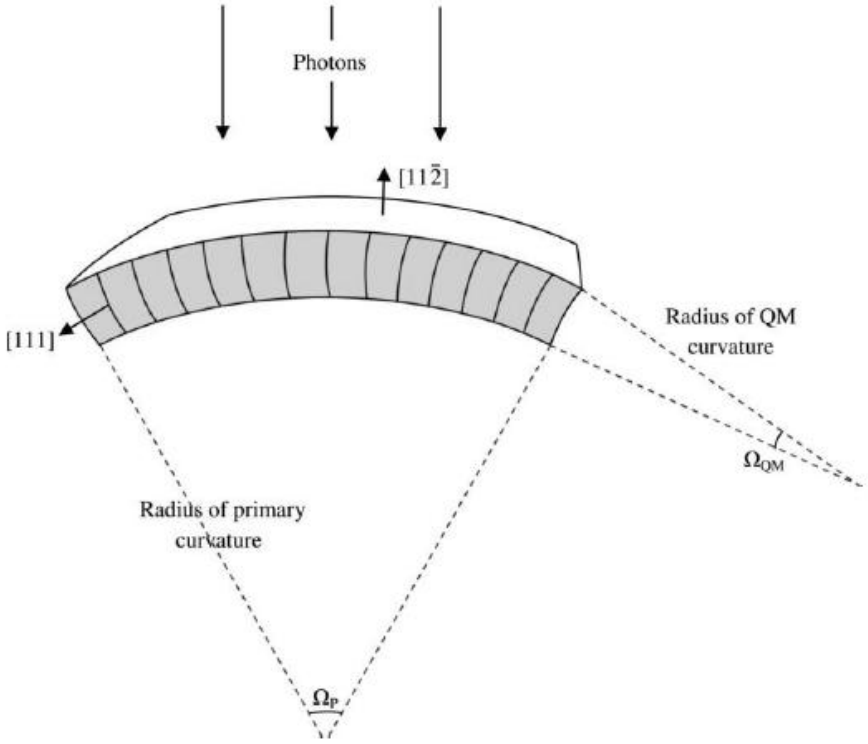

Figure 3.4: the primary curvature of a properly oriented crystal leads to a secondary curvature owing to quasi-mosaicity. For a Laue lens, quasi-mosaic curvature of the (111) lattice planes resulting from primary bending of the (112) crystal plates is proposed for diffraction. In this configuration the (111) diffracting planes are perpendicular to the main surface of the plate; thus positioning of the crystals in the lens would be the same as for mosaic crystals. Ω_P and Ω_{QM} are the primary and secondary bending angles, respectively [3.29].

3.3. Material and methods

3.3.1. Surface grooving technique

Grooves manufactured on the surface of a Si plate by a diamond saw is known to deform the whole crystal, leading to a net and permanent curvature [3.17, 3.18]. The origin of permanent deformation can be intuitively interpreted in terms of irreversible compression of the crystal beside and beneath the grooves. This region is rich in dislocations, partly amorphous and its extent is generally limited to some microns, depending on dicing parameters, e.g., grit and advance speed of the blade [3.24, 3.25]. Such a highly defected region acts as a solid wall for the crystalline material between the grooves and prevents it from full mechanical relaxation. Thus, the array of elastically compressed regions behaves as an "active plasticized layer", imparting internal forces to the whole crystal, thus bending the remaining crystal below them. It ultimately results in a net and uniform curvature within the crystal without the usage of any external device. In Ref. [3.25], a model based on the theory of elasticity has been developed to foresee measured curvature of grooved samples. The model is based on the assumption that the plasticized layer behaves as a compressive film. Indeed, the Stoney approach was used to determine the curvature of grooved samples.

Fabrication of curved Si and Ge crystals has been developed through the method of surface grooving by the usage of a high precision dicing machine (DISCO^{TM} DAD3220), equipped with a rotating blade of various width, geometry and diamond grit size. Depending on the geometry of CDP crystals, grooves were manufactured on the surface of the plates along either one or two perpendicular directions.

In order to verify the possibility to deform a sample through the grooving method, a preliminary test was done on a 10×10×2 mm^3 silicon sample. A single groove, 160 μm wide and 1680 μm deep, was done parallel to the sides passing through the center of its surface (see left side of Fig. 3.5). Analysis of the deformation of the crystal, i.e., of its crystallographic planes, has been investigated at several positions along x axis, by usage of the high-resolution X-ray diffractometer at Sensor and Semiconductor Laboratory (Ferrara, Italy) in Bragg geometry (Cu Kα radiation, λ = 1.54 Å). For every step, the crystal was rotated around the angle where Bragg diffraction occurs, thus recording the so-called rocking curve (RC) (see right side of Fig. 3.5). As can be noticed, the Si plate takes the shape of a dihedron bent by 30 arcsec just beneath the groove. If instead of an individual groove, a regular grid of grooves is done on the same surface, a net curvature can be achieved. This is the key idea about deformation of a Si plate by the method of surface grooving.

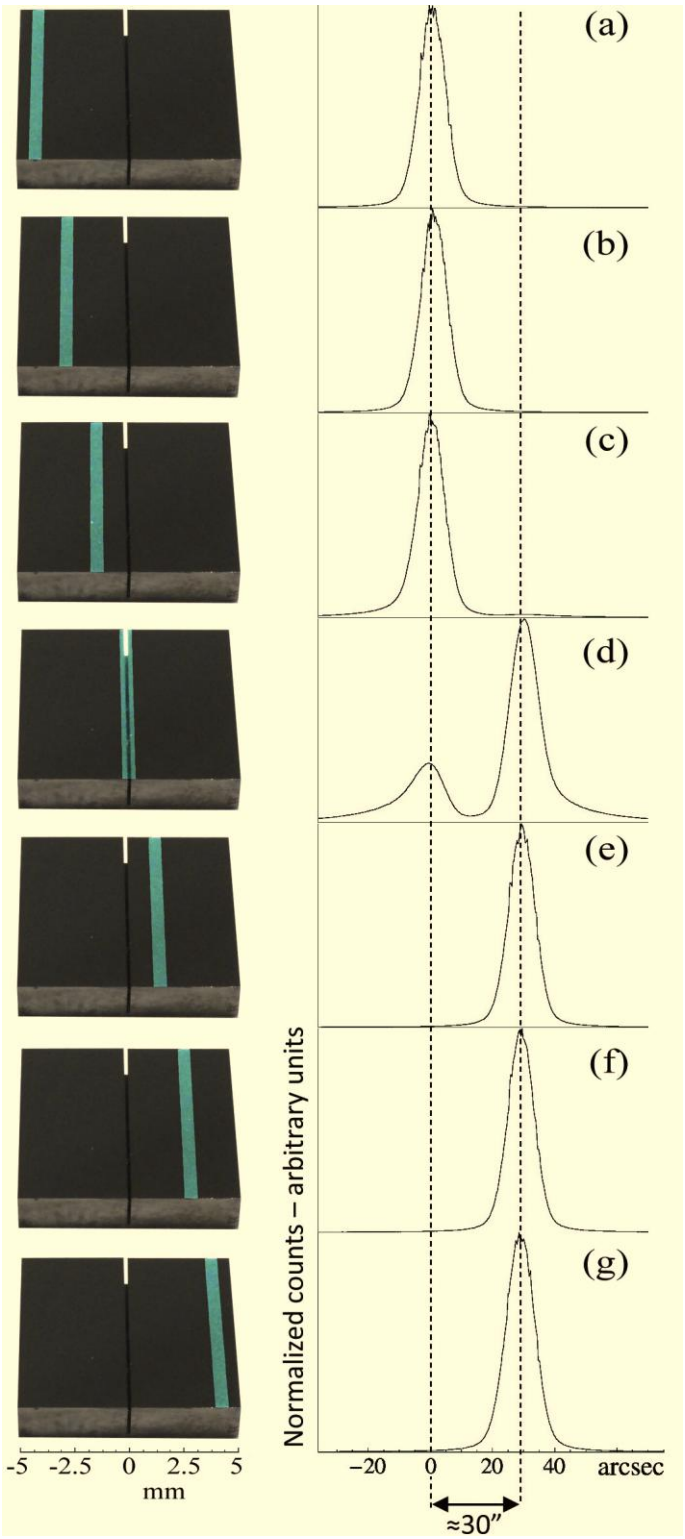

Figure 3.5: Left side: photos of the 10×10×2 mm^3 Si plate. The clearer rectangles represent the areas where X-ray beam impinges and diffracts. The groove is centered at x = 0 mm. Seven measures was done, at (a) = -4 mm, (b) = -2.5 mm, (c) = -1 mm, (d) = 0 mm, (e) = 1 mm, (f) = 2.5 mm, (g) = 4 mm. Right side: Rocking curves relative to each position as specified by the photo on the left. X-axis is the angle between X-rays and crystallographic planes [3.25].

3.3.2. Fabrication of single Si and Ge curved crystals for X-ray characterization at ESRF

With regard to "geometry 1", production of single curved crystals has been carried out. Commercially available pure Si and Ge wafers were diced to form plates using a high precision dicing saw, equipped with rotating diamond blades of various width and grain size.

Grooves were manufactured on the surface of the plates along one direction, i.e., either x or y (Fig. 3.6a). Si and Ge single plates were 1 mm and 2 mm thick, respectively, and their orientation was the (111), these planes being normally selected for X/gamma-ray focusing because of their high reflectivity. Fabrication parameters of all the samples are reported in Table 1 and an image of one of the samples is shown in Fig. 3.7.

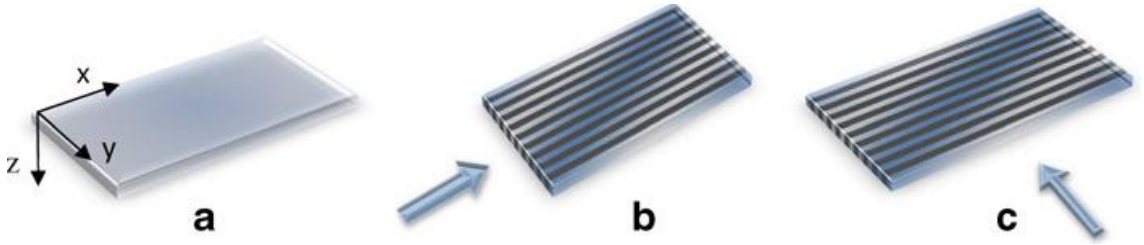

Figure 3.6: Grooves were manufactured on the surface of a Si or Ge plate along one direction, either x or y (a). The probe x-ray beam enters the sample parallel (b) or perpendicular (c) to the grooves [3.18].

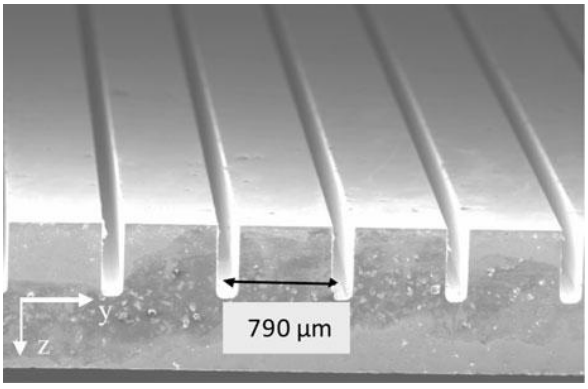

Figure 3.7: Side view of sample S71 with a series of grooves as taken by scanning electron microscope. The black arrow indicates the pitch of the grooves [3.18].

For every crystal, the curvature induced by grooves was measured using an optical profilometer (VEECO^{TM} NT1100) with 1 µm lateral and 1 nm vertical resolution. The profilometer is equipped with a stitching system that allows scanning over as wide an area as 10 × 10 cm^2. In order to account for the initial morphological non-planarity of the samples (wafers are generally not perfectly flat), subtraction of profile before and after the grooves was done. Moreover, since the profile of a surface with grooves is altered by their presence, thus making the analysis more difficult, profilometric characterization was carried out on the back face of each sample. As a result of the grooving process, an ellipsoidal surface appeared, with the shortest radius of curvature perpendicular to the grooves. A typical profilometric pattern of one of the samples is shown in Fig. 3.8. Production and optical characterization of all samples have been carried out at Sensor and Semiconductor Laboratory (Ferrara, Italy).

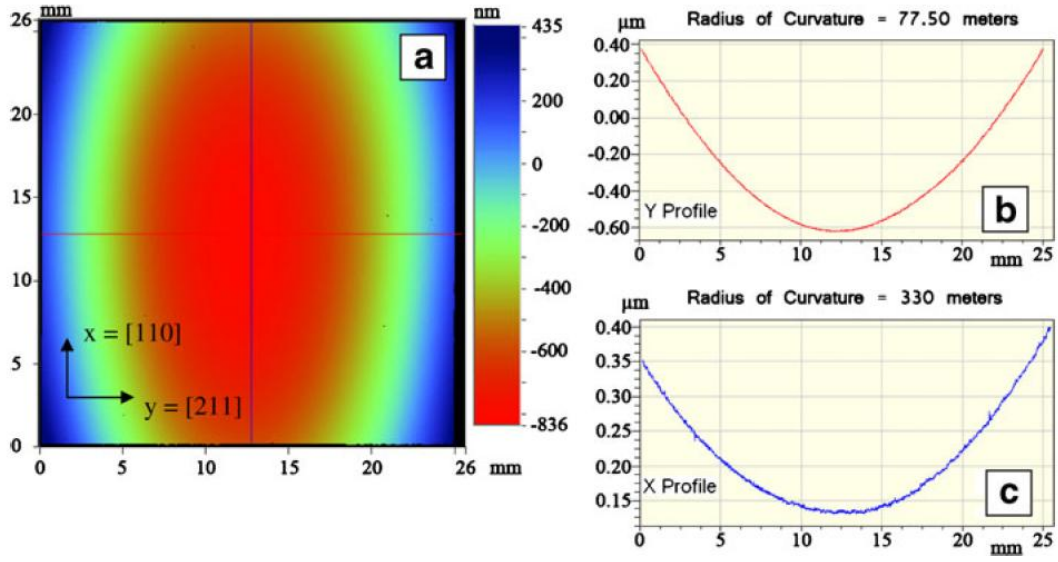

Figure 3.8: Optical profilometry scanning of the surface without grooves of crystal S71 (a). Falsecolor epresentation of deformation is highlighted. Cross sections of the deformation pattern along y = [211] (b) and x = [110] (c) directions as taken on the center of the sample with indications of the two main curvature radii [3.18].

Single Si and Ge grooved crystals were tested under X-ray diffraction experiment at European Synchrotron Radiation Facility (Grenoble, France). At beamline ID15A, a highly monochromatic and quasi-parallel beam was tuned to the desired energy, ranging from 150 to 700 keV. All samples were analyzed by diffraction of their (111) planes, the pencil beam entering the sample at different depths from the grooved surface (coordinate z). Two different configurations were used, i.e., the beam was set quasiparallel (hereinafter referred to as parallel) or perpendicular to the grooves, its size being 50 × 50 µm^2 and 100 × 50 µm^2, respectively. A sketch of the two configurations is shown in Figs. 3.6b and c.

3.3.3. Fabrication of stacks of Si curved crystals for X-ray characterization at ILL

3.3.3.1. Stack_1

Commercially available pure Si wafer was diced to form three plates by using the dicing machine at Sensor and Semiconductor Laboratory. The plates were 1 mm thick and their orientation was (111), these planes being normally selected for X/γ-ray focusing because of their high reflectivity. Once cleaved from the same wafer, grooves were manufactured on the surface of the plates along one direction. Preliminary characterization of every plate through optical profilometry guaranteed that they were morphologically equivalent (Figs. 3.9a and b). In order to account for the initial morphological non-planarity of the samples (wafers are generally not perfectly flat), subtraction of the profiles before and after the grooving process was done for every plate. Profilometric characterization was carried out on the back face of each plate. As a result of grooving, an ellipsoidal surface appeared, with the smallest curvature radius perpendicular to the grooves. The crystals were finally mounted on a hot plate and bonded one over the other to form a stack (Fig. 3.9c) by using a low-stress thermal paste. At nominal temperature, the glue melts and solidifies on cooling, yielding a stack of plates in a stable way. To verify that bonding has not altered the morphology of the crystals, subtraction of the morphological profiles before and after the

bonding was done to the crystal on the top of the stack. Fabrication parameters of the multi-crystal are reported in Table 1.

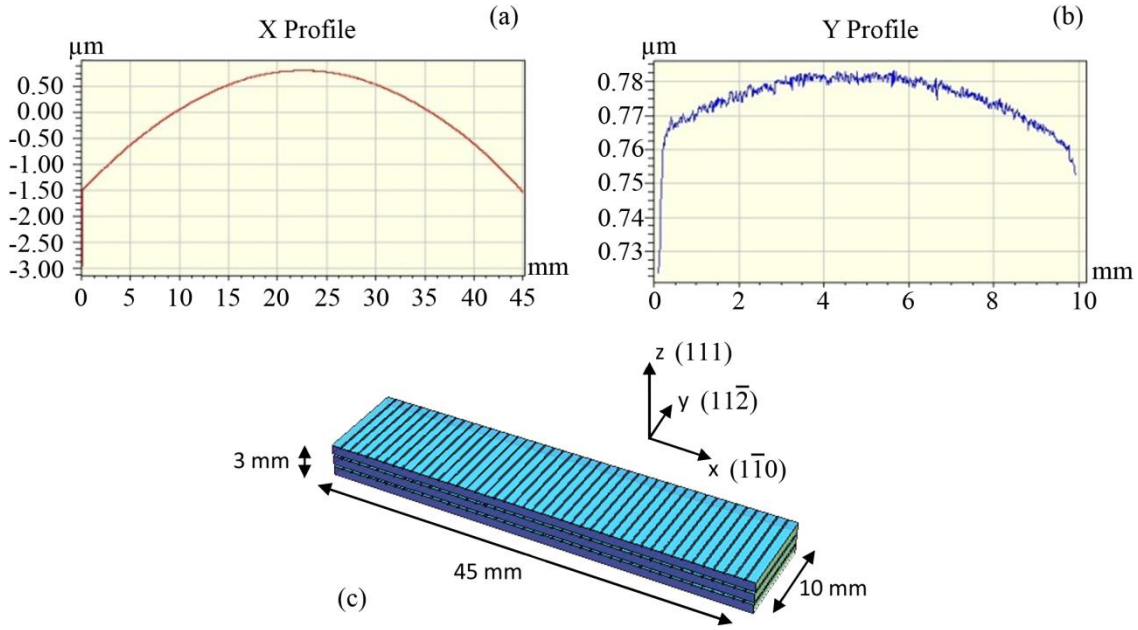

Figure 3.9: Stack_1. Optical profilometric scanning of the surface without grooves of one of the Si plates. Cross sections of the deformation pattern along x (a) and y (b) directions are highlighted, as taken on the center of the sample. Two main curvature radii are 110 m and 540 m along *x* and *y*, respectively. Stacking of Si crystals was obtained by bonding the plates one over the other thanks to a low-stress thermal paste. As visible, grooves were manufactured on the surface of each plate along *y* direction (c) [3.27].

3.3.3.2. Stack_2

Fabrication of a stack of two Si curved crystal plates, coded as stack_2, was carried out in the same way as for stack-1. At Sensor and Semiconductor Laboratory commercially available pure Si wafer was diced to form two plates by using the dicing machine. The plates were 1 mm thick and their orientation was (111). Once cleaved from the same wafer, grooves were manufactured on the surface of the plates along one direction. In order to guarantee that the plates were morphologically equivalent, a preliminary characterization of every plate (on their back face) was carried out by optical profilometry (Figs. 3.10a and b). Moreover, to account for the initial morphological non-planarity of the samples, subtraction of the profiles before and after the grooving process was done for every plate. As a result of grooving, an ellipsoidal surface appeared, with the smallest curvature radius perpendicular to the grooves. Then, the crystals were finally mounted on a hot plate and bonded one over the other to form a stack (Fig. 3.10c) by using the low-stress thermal paste. Finally, to verify that bonding has not altered the morphology of the crystals, subtraction of the morphological profiles before and after the bonding was done to the crystal on the top of the stack. Fabrication parameters of stack_2 are reported in Table 1.

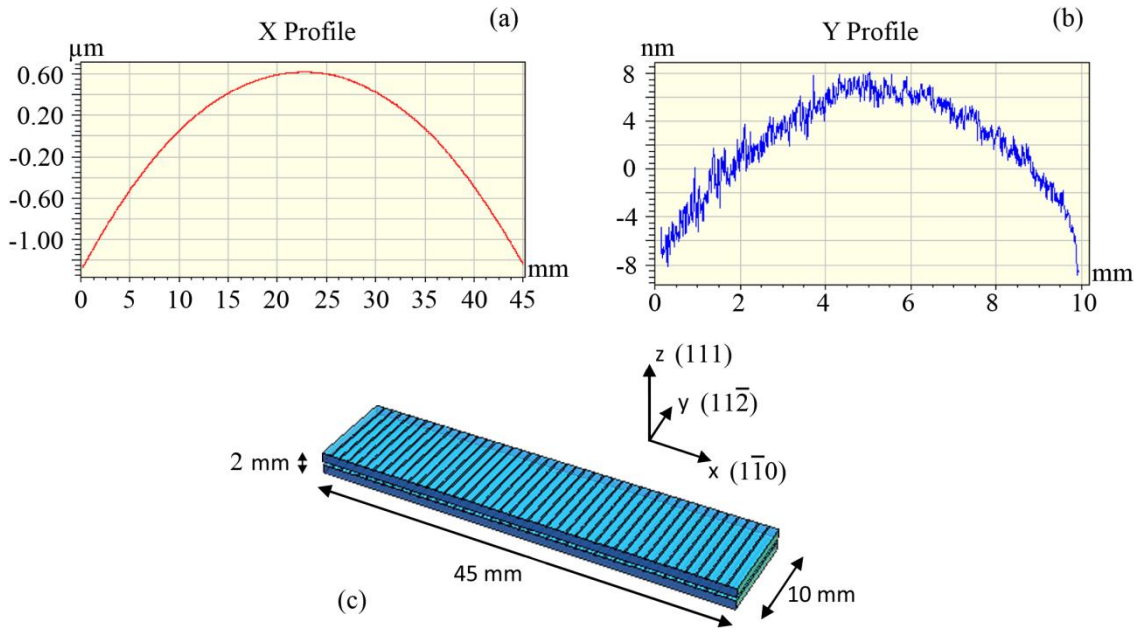

Figure 3.10: Stack_2. Optical profilometric scanning of the surface without grooves of one of the Si plates. Cross sections of the deformation pattern along x (a) and y (b) directions are highlighted, as taken on the center of the sample. Two main curvature radii are 130 m and 940 m along *x* and *y*, respectively. Stacking of Si crystals was obtained by bonding the plates one over the other thanks to a low-stress thermal paste. As visible, grooves were manufactured on the surface of each plate along *y* direction (c).

The stacks were tested through X-ray diffraction at Laue Langevin Institute (ILL, Grenoble, France) by using a hard X-ray diffractometer based on the method of X-ray focusing for transmission (Laue) geometry. The diffractometer used a polychromatic and divergent X-ray beam having energy between 80 and 450 keV, emitted from a high-voltage and fine-focus X-ray tube. Main features of the instrument can be found in Chapter 2. The multi-crystals were measured in two different configurations, i.e., the beam was set parallel to the (2$\bar{2}$0) or (111) planes, its size being chosen 10×1 mm^2 and 10×0.5 mm^2, respectively. A sketch of the two configurations is shown in Figs. 3.11a and b.

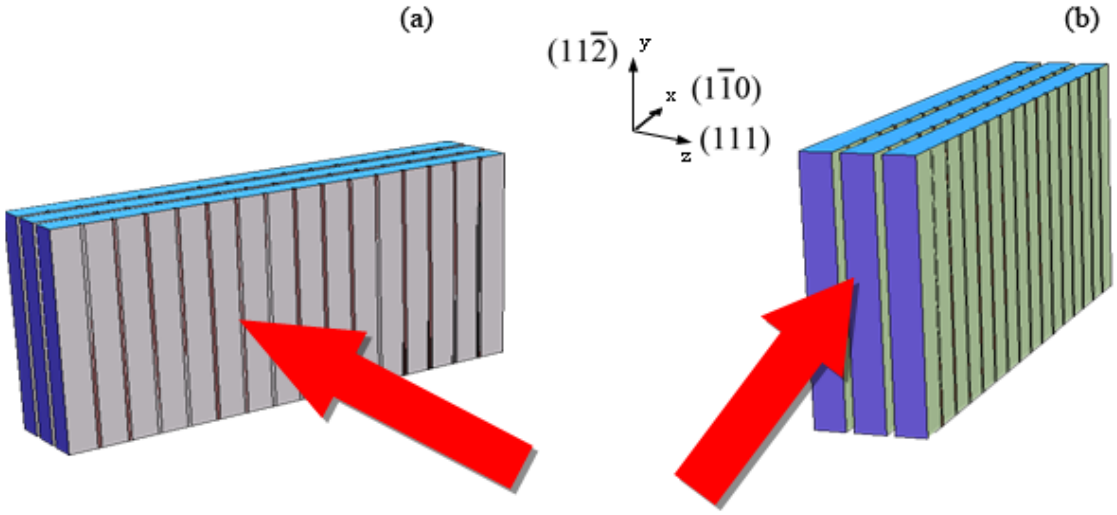

Figure 3.11: Probe x-ray beam (red arrow) enters the stack quasi-parallel to the (2$\bar{2}$0) (a) or to the (111) crystallographic planes (b). In case (a), collimated-beam size dimension was 1 mm on the diffraction plane *xz* and 10 mm on the plane *yz*. In case (b), beam size was 0.5 mm on *xz* plane and 10 mm on *yz* plane [3.27].

With the aim to check the reciprocal alignment of the (111) diffracting planes in the stack, the multi-crystal was measured in the configurations sketched in Figs. 3.10a and b. Indeed, X-ray diffraction by both $(2\bar{2}0)$ and (111) planes are most sensitive to the critical misalignment of the (111) planes because the photons impinging onto such misoriented planes would be diffracted according to Eq. (1.38). In case of (111) planes misaligned as in Fig. 3.3d, the relationship between two diffracted photons satisfies Eq. (1.39), thus $(2\bar{2}0)$-diffraction is less sensitive to this misorientation. On the other hand, X-ray diffraction by $(2\bar{2}0)$ planes cannot reveal the less important misalignment depicted in Fig. 3.3c, this behavior being described in Eq. (1.40). X-ray diffraction by (111) planes is less sensitive to the misalignment in Fig. 3.3c, while no detection of the misorientation in Fig. 3.3d can be obtained. For both the configurations in Fig. 3.11, analysis with the beam undergoing Laue diffraction by $(11\bar{2})$ planes is most sensitive to the misalignment shown in Fig. 3.3c, while it is less sensitive to the misorientation as in Fig. 3.3d. Finally, no detection of the misorientation in Fig. 3.3b can be observed.

Table 1 (i): Fabrication parameters of the samples

Code	S24	S31	S71	S72
Size (mm^3)	9.8×9.8×1	12.2×12.2×1	25.5×25.5×1	25.5×36.6.×1
Material	Silicon	Silicon	Silicon	Silicon
Number of grooves	15	15	31	25
Grooves step (μm)	650	780	790	1000
Depth of grooves (μm)	500	500	500	400
Blade	Very Hard	Hard	Hard	Hard

Table 1 (ii): Fabrication parameters of the samples

Code	S81	2_G32	Stack_1	Stack_2	G3
Size (mm^3)	54.2×30.6×1	18.6×9.8×2	45×10×3	45×10×2	15×15×1
Material	Silicon	Germanium	Silicon	Silicon	Silicon
Number of grooves	30	11	43	43	15×15
Grooves step (μm)	1000	800	1050	1050	1000
Depth of grooves (μm)	400	1000	120	120	500
Blade	Hard	Hard	Hard	Hard	Hard

3.3.4. Fabrication of a quasi mosaic Si crystal for X-ray characterization at ILL

On the basis of "geometry 2" for Laue lens, a quasi-mosaic Si crystal has been produced through the manufacture of a grid of superficial grooves on one of the largest surfaces of the crystal at Sensor and Semiconductor Laboratory (Ferrara, Italy). Crystallographic orientations are indicated in Fig. 3.2c. In fact, commercially available pure Si wafer was diced to form a plate using the high-precision dicing saw at Sensor and Semiconductor Laboratory, equipped with rotating diamond blades of 150 μm width and 5 μm diamond grain size (G1A 320). Thanks to the grooving method, a permanent primary curvature was induced. This latter was morphologically measured by optical profilometry and then its crystallographic structure was verified through X-ray diffractometry at Sensor and Semiconductor Laboratory. Main features of the crystal are reported in Table 1.

The sample, coded as G3, was tested through X-ray diffraction at the Institute Laue-Langevin (ILL) at DIGRA facility, with a γ-ray beam with energy = 181.931 keV and monochromaticity $\Delta E/E \approx 10^{-6}$. The γ-ray flux was produced by neutron capture in a gadolinium target inserted close to the nuclear reactor of ILL at a temperature of about 400℃. Beam divergence after the Si (220) monochromator was 1 arcsec, as measured by recording a rocking curve (RC) of the monochromator itself. Collimated-beam size dimension was 1 mm on the diffraction plane (xz) and 3 mm on the plane (yz), z being the direction of the beam. The detector was a 25% HPGe from Canberra.

3.4. Experimental results and discussion

3.4.1. Si crystals S71, S72 and S81

The main characteristics of each measured sample are summarized in Table 2. As an example, the features of samples S71 and S81 are extensively described.

The crystal S71 was initially measured at 150 keV with the beam penetrating the sample through its 25.5 × 1 mm^2 surface at different depths from the grooved side, parallel and perpendicular to the grooves. Bending angles of the sample, as measured by optical profilometry, averaged 15.7 and 66.6 arcsec along the [110] and [211] directions, respectively. Figure 3.12 shows both diffracted and transmitted RCs as normalized to transmitted beam intensity (so that diffraction efficiency is readily displayed). All RCs exhibited flat-topped and uniform shapes with FWHM of the order of crystal bending, i.e., it averaged 14.1 and 57.1 arcsec for parallel and perpendicular cases, respectively. This sample features significantly high efficiency when the beam is parallel to the grooves, highlighting very homogeneous diffraction pattern with efficiency about 93.4% over the whole depth. This performance highlights that a bent crystal can amply break the 50%-efficiency limit. With the beam perpendicular to the grooves, diffraction efficiency is still a good performance though it varies over the crystal depth, i.e., it is nearly 50% close to the grooved region, and raises up to 71% deeper into the crystal.

Table 2: Main performance of all the samples under analysis

Code	S24	S31	S71	S71	S72	S81
Photon Energy (keV)	150	150-500	150-700	150-700	150-600	300
Beam configuration	Perp. to the grooves	Perp. to the grooves	Par. to the grooves	Perp. to the grooves	Perp. to the grooves	Par. to the grooves
Bending angle (arcsec)	32.2	35.1	15.7	66.6	55.0	29.5
Angular spread (arcsec)	26.2	23.6	14.1	57.1	49.9	25.7
Max diffraction efficiency at lowest energy	81.7%	69.1%	94.9%	71.1%	79.4%	86.4%
Averaged diffraction efficiency at lowest energy	54.9%	51.1%	93.4%	56.1%	60.3%	81.8%

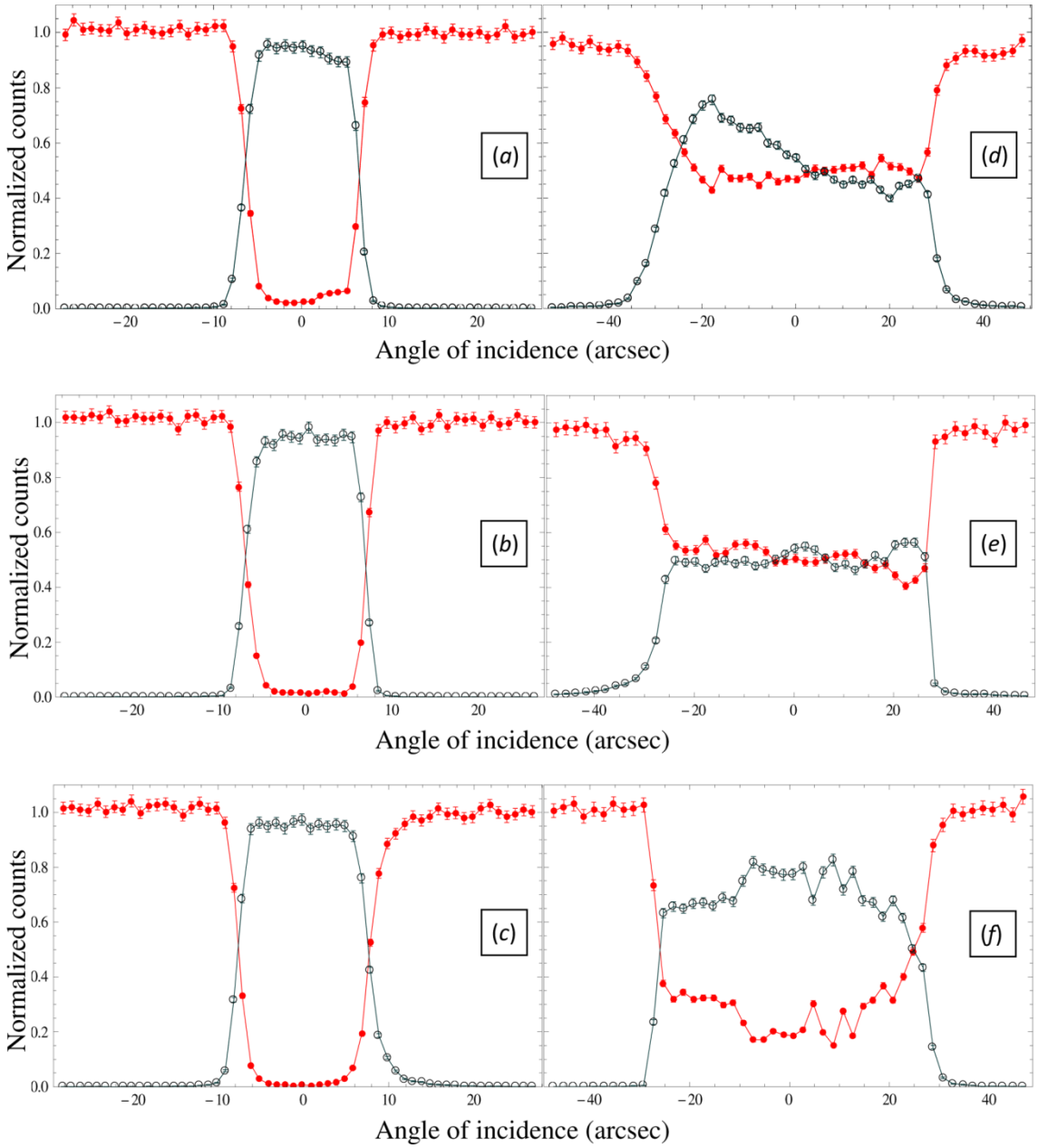

Figure 3.12: RCs of crystal S71 with the beam parallel to the grooves at several distances from the indented face, i.e., at (a) z = 0.4 mm, (b) z = 0.6 mm, (c) z = 0.8 mm; all the RCs were recorded at y = 13.9 mm. RCs of the same crystal with the beam perpendicular to the grooves at (d) z = 0.15 mm, (e) z = 0.55 mm, (f) z = 0.85 mm; all the RCs were recorded at x = 15 mm. The filled red circles plot the intensity of the transmitted beam, whereas the empty blue circles plot the intensity of the diffracted beam. RCs with rectangular and homogenous shapes were achieved in all cases, with an energy passband of the order of crystal bending (about 16 arcsec for the parallel case and 57 arcsec for the perpendicular case). Efficiency is significantly high in all cases and close to the unity in the parallel case. Notice that in (d) the sum of the transmitted and diffracted beams is bigger than 1 in the left part of the RCs. This artefact is due to the proximity of the surface where the diffracted beam leaves the crystal through its large face before reaching the edge. Thereby, the path of the diffracted beam does not cross the whole thickness of the crystal, resulting in smaller absorption [3.18].

Such features are better pointed out in Fig. 3.13a and b, where diffraction efficiency is shown as a function of coordinates z and y (z and x), for the parallel (perpendicular) case. Efficiency results constantly close to the unity in the parallel case while it smoothly varies over the whole depth in the other configuration. However, no dependence on coordinate y (or x) was recorded in any case. The same dependence was recorded for angular spread for parallel and perpendicular

cases (Fig. 3.13c and d, respectively). It follows that the curvature is uniform along coordinate y (or x), though its dependence on coordinate z shows different profile. Indeed, as the distance from the grooved face increases, the angular distribution slightly increases for the parallel case. Perpendicularly to the grooves, the variation of the angular spread within the crystal is stronger, i.e., it increases across the groove depth and decreases outside. This evidence can be ascribed to the fabrication process of indentations. In fact, generation of mosaicity perpendicularly to the advance speed of the blade is easier to form than longitudinally because of the stronger action exerted by the blade on the side walls of the groove. This effect leads to an increase in angular spread, and consequently in energy bandwidth, resulting in efficiency decrease throughout the whole depth of the grooves. Indeed high efficiency is restored beneath the grooves, meaning that the curvature of diffracting planes is homogeneous and its structure is not significantly affected by mosaicity.

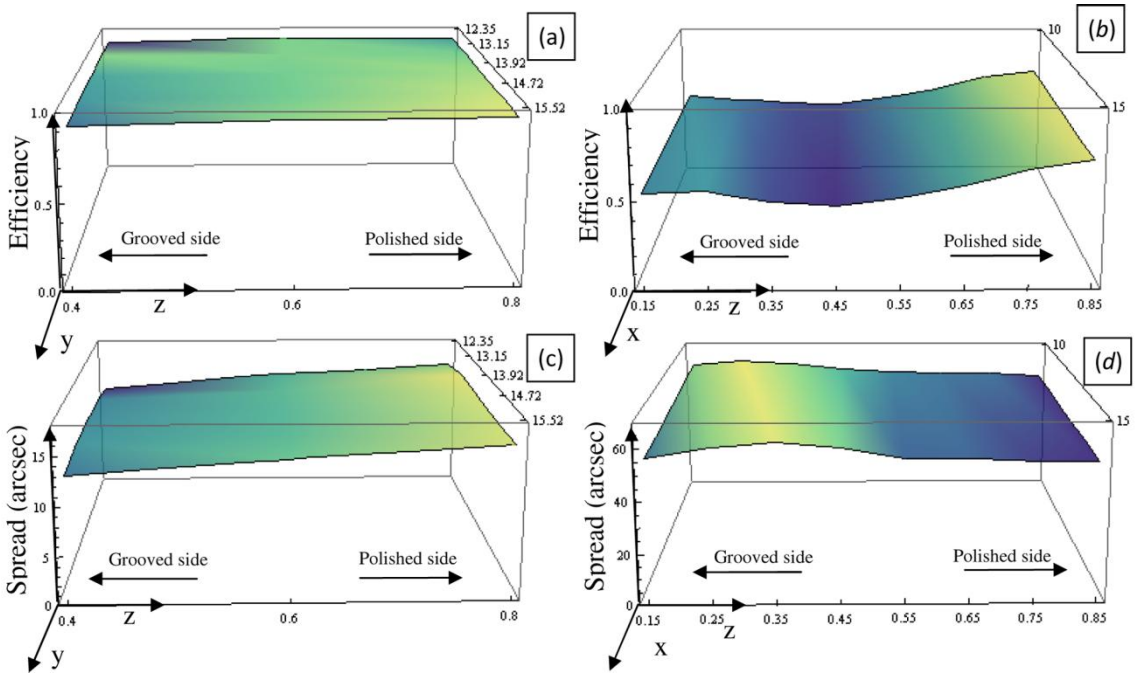

Figure 3.13: Diffraction efficiency of crystal S71 vs. coordinate z (mm) at several positions within the crystal (coordinate *y* or *x*) for parallel (a) and perpendicular (b) cases. Same dependence of angular spread is shown for parallel (c) and perpendicular (d) cases. No dependence on coordinate *y* (or *x*) was recorded in any case. Efficiency near the polished side of the sample is close to the unity while it gently decreases close to the grooved side in the parallel case and more strongly in the perpendicular case [3.18].

Finally the sample was measured at several energies, the beam entering the crystal far from the grooved region, parallel and perpendicular to the grooves. RCs are shown here for parallel case (Fig. 3.14). The sample features significant diffraction efficiency up to 700 keV, ranging from 92% down to 29%. With the beam perpendicular to the grooves, efficiency keeps lower than 60% above 200 keV. Next section compares experimental performance to theoretical expectations, showing that the decrease in efficiency with energy is completely in agreement with the dynamical theory of diffraction.

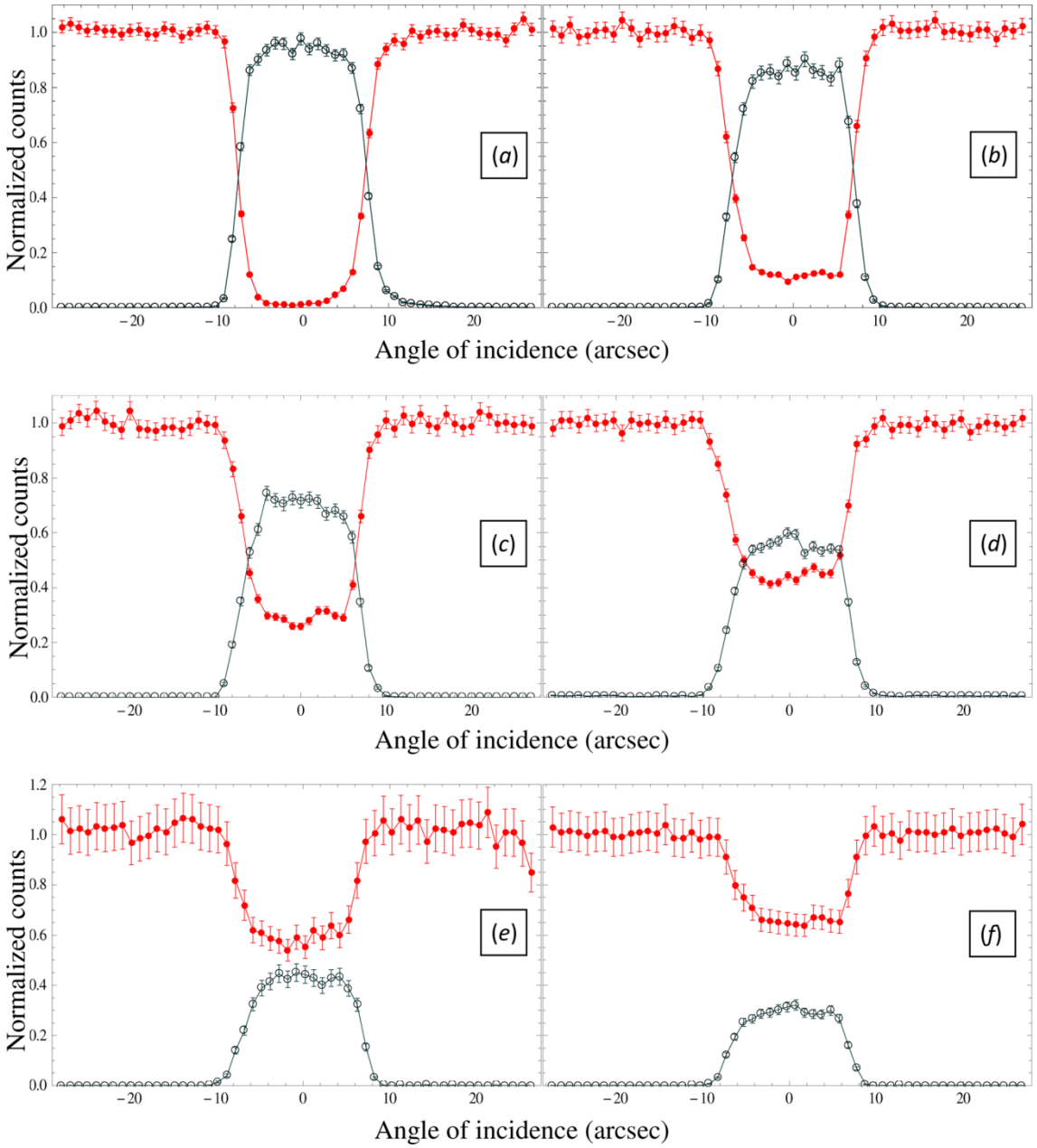

Figure 3.14: RCs of crystal S71 with the beam parallel to the grooves, measured at *z* = 0.8 mm and *y* = 13.9 mm. Beam energy was set at 200 keV (a), 300 keV (b), 400 keV (c), 500 keV (d), 600 keV (e) and 700 keV (f). The filled red circles plot the intensity of the transmitted beam, whereas the empty blue circles plot the intensity of the diffracted beam. Efficiency falls off with photon energy according to the dynamical theory of diffraction though a rectangular shape of the distribution is preserved [3.18].

Si crystal S81 was measured at 300 keV with the beam penetrating the sample through its 30.6 × 1mm^2 surface, at fixed depth from the grooved side (coordinate z) and at different coordinates y. The beam was set parallel to the grooves. Bending angle of the sample, as measured by optical profilometry, averaged 29.5 arcsec along [110] direction. Figures 3.15a, b and c show both diffracted and transmitted RCs as normalized to transmitted beam intensity, so that diffraction efficiency is readily displayed. RCs exhibited flat-topped rectangular and uniform shapes with a FWHM of 26 arcsec, close to the optically determined crystal bending. This sample features a significantly high efficiency, about 82% constantly over the whole sample, showing that a curved crystal can amply break the 50%-efficiency limit, which holds true for an unbent crystal. No

dependence on coordinate y was recorded, meaning that curvature is homogeneous throughout the sample.

With the beam perpendicular to the grooves of sample S72, efficiency showed different behavior from the previous case. This sample was measured at 150 keV with the beam entering the Si crystal through its 25.5×1 mm^2 at different depths from the upper grooved side. Bending angle of the sample was measured by optical profilometry to be 55 arcsec along [211] direction. The RCs in figs. 3.15d, 4e and 4f still highlight flat-topped and uniform shapes though efficiency varies over the crystal depth, i.e. it is nearly 50% close to the grooved region, and raises up to 79% deeper into the crystal. As for sample S71, this feature is ascribed to the fabrication process of grooves and in particular to the generation of mosaicity perpendicularly to the advance speed of the blade. This leads to an efficiency decrease throughout the whole depth of the grooves while outside the grooved area, high efficiency is restored, meaning that crystal structure is not significantly affected by mosaicity.

Sample S72 was also characterized vs. energy, the beam entering the crystal far from the grooved region and perpendicular to the grooves (fig. 3.16). The sample features significant diffraction efficiency up to 600 keV, ranging from 80% down to nearly 20%.

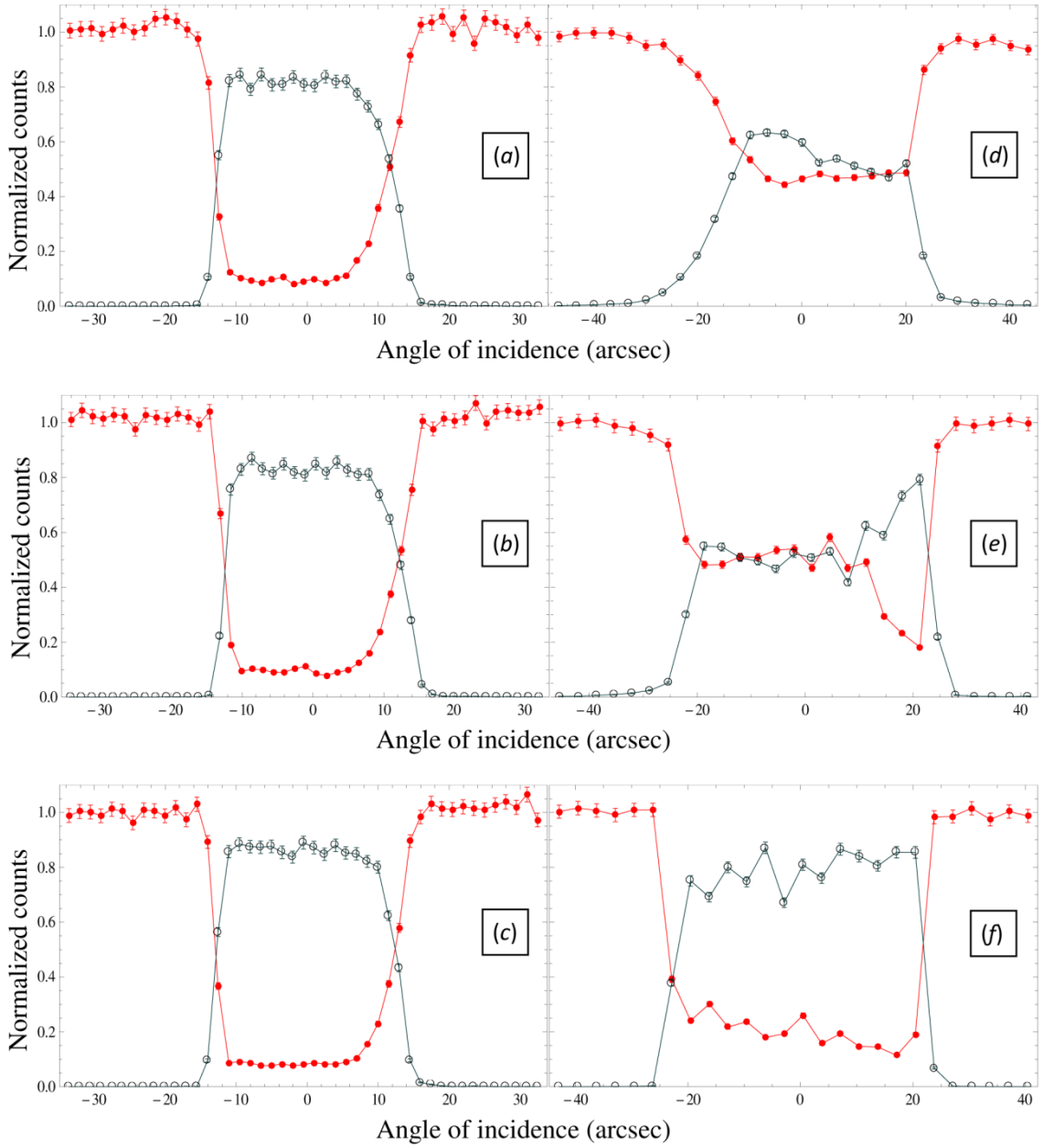

Figure 3.15: The left-hand side shows RCs of crystal S81 with the beam parallel to the grooves at a fixed distance from the grooved face and at y = 5.0 mm (a), y = 5.9 mm (b), y = 6.8 mm (c). The right-hand side shows RCs of crystal S72 with the beam perpendicular to the grooves at different depths from the grooved surface, i.e. at z = 0.05 mm (d), z = 0.55 mm (e), z = 0.75 mm (f). RCs with rectangular and homogenous shapes were achieved in all cases, with an energy passband of the order of crystal bending (about 26 arcsec for the sample S81 and 55 arcsec for S72). Efficiency is significantly high in all cases and up to 82% for sample S81 [3.35].

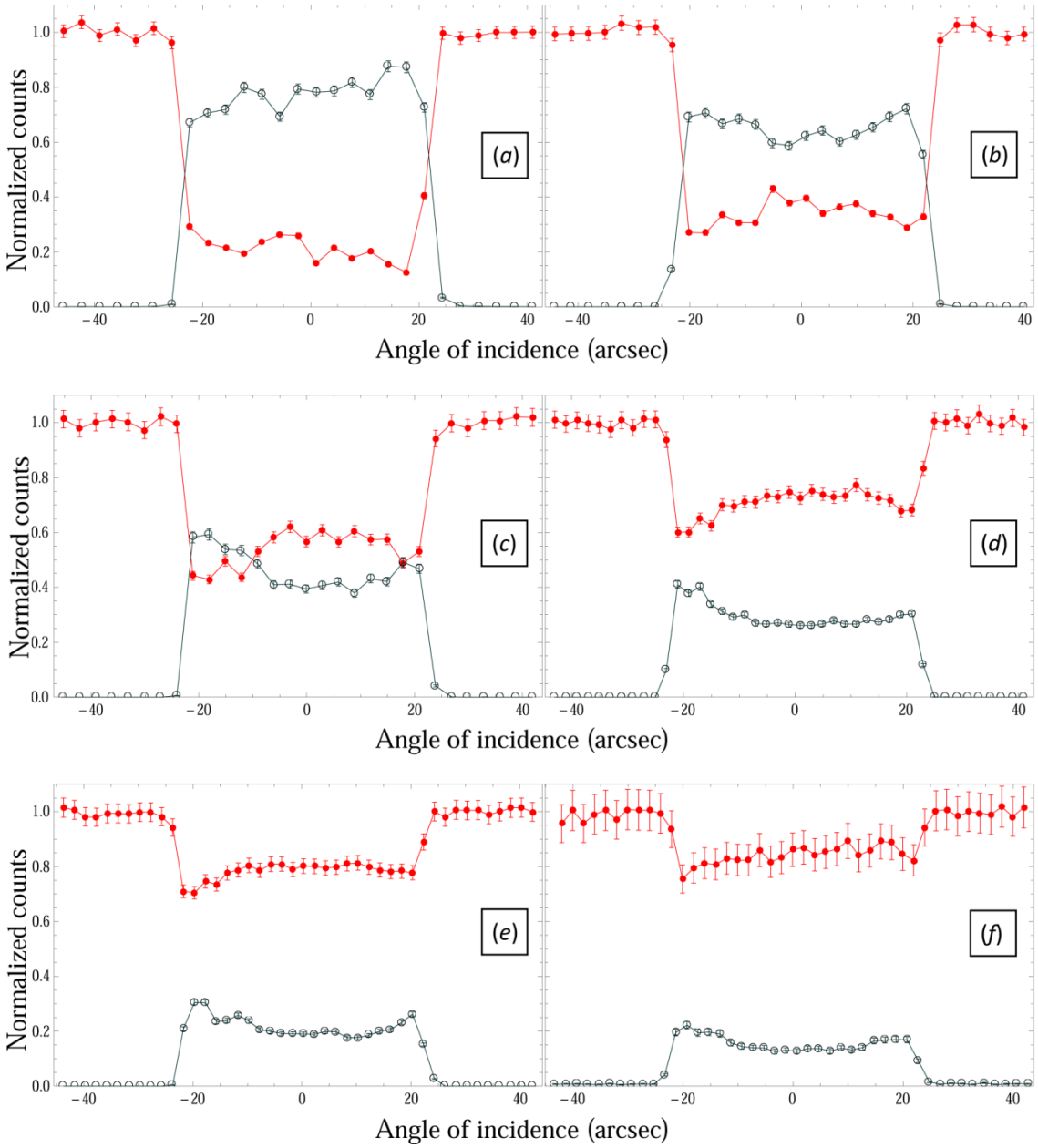

Figure 3.16: RCs of crystal S72 with the beam perpendicular to the grooves, measured at z = 0.75mm and x = 0.15 mm. Beam energy was set at 150 keV (a), 200 keV (b), 300 keV (c), 400 keV (d), 500 keV (e) and 600 keV (f). Efficiency falls off with photon energy according to dynamical theory of diffraction though a rectangular shape of the distribution is preserved [3.35].

3.4.1.1. Simulations

In order to deepen the understanding of diffraction properties of the samples, a custom-made software specifically designed for CDP crystals and inspired to the code in Ref. [3.3] has been developed. This latter was developed through Python programming language, which takes advantage of a very large and comprehensive standard library and is largely used by the scientific community.

The software describes diffraction in both curved and mosaic crystals and generates the physical quantities of interest. Such quantities, typically used to qualify the diffraction properties of a crystal, are diffraction efficiency and reflectivity as defined in Chapter 1. For any set of parameters such as crystalline material, set of reflection planes and thickness of curved or mosaic

crystal, the code computes reflectivity and diffraction efficiency as a function of photon energy and angular spread (or mosaicity). Expected performance is then compared to experimental data.

The results of the simulations will be shown here for sample S71. In Fig. 3.17, experimental diffraction efficiency vs. z is compared to the theoretical efficiency in case of a perfectly curved crystal and a mosaic crystal. These latter were calculated taking into account the FWHM of the RCs, thus an experimental uncertainty is included. Due to generation of mosaicity perpendicularly to the grooves, measured efficiency varies over the crystal depth, being always lower than the theoretical limit for a perfectly bent crystal, especially within the groove depth. However, this performance keeps always higher or at worst equal to the theoretical efficiency for a mosaic crystal, meaning that the grooves allow obtaining a homogeneous curvature with no significant damage of the crystal.

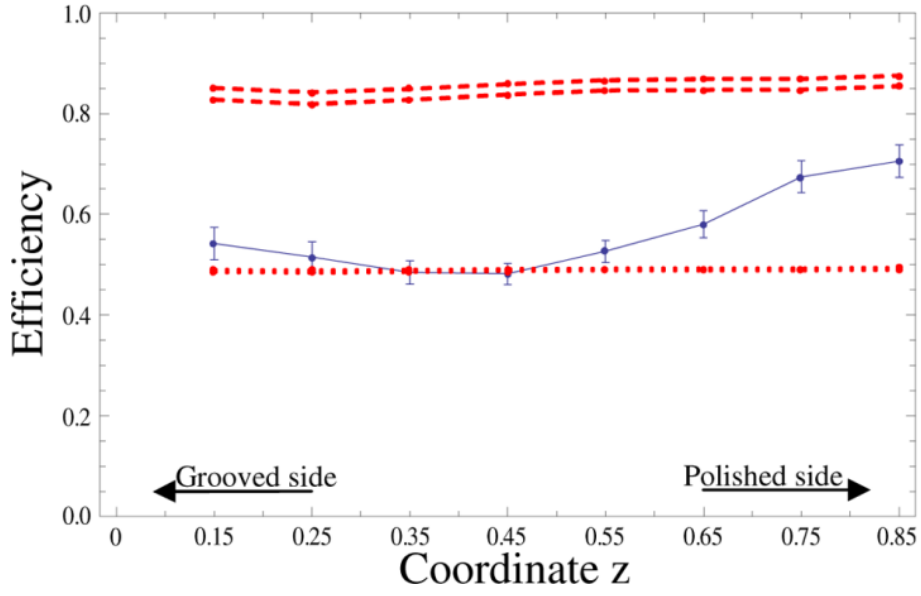

Figure 3.17: Experimental efficiency (blue circles) vs. coordinate *z* (mm) for crystal S71 with the 150 keV probe beam perpendicular to the grooves. Red dashed and dotted lines represent theoretical efficiencies in case of a curved and of a mosaic crystal, respectively. An experimental uncertainty is included in both cases. Due to generation of mosaicity, experimental efficiency varies within the crystal, being lower over the whole groove depth and increasing outside. However, diffraction efficiency is always higher or at worst equal to the theoretical contribution given by a mosaic crystal [3.18].

In order to better understand the behavior of diffraction response, the crystal has been modeled as it were made by two coexisting structures at any coordinate z, i.e., a mosaic crystal and a perfectly curved crystal. Based on this model, diffraction efficiency was considered as the superposition of the contributions of the two kinds of crystal. Here, C(*z*) is the fraction of perfectly curved crystal-like behavior and [1-C(*z*)] the contribution of mosaicity, such that

$$\varepsilon(z) = C(z)\varepsilon(c) + [1 - C(z)]\varepsilon(m) \qquad 3.5.$$

where $\varepsilon(z)$ is the experimental diffraction efficiency obtained at a given distance from the top of the crystal, $\varepsilon(c)$ the expected diffraction efficiency for a perfectly curved crystal and $\varepsilon(m)$ the expected diffraction efficiency in case of a mosaic crystal. As a result, for the perpendicular case, the fraction of mosaicity [1-C(z)] is close to the unity in the region of the grooves, and vanishes outside (see Fig. 3.18). For the parallel configuration the mosaicity fraction keeps about 8% throughout the entire thickness of the sample. Indeed, in the parallel case, experimental efficiency is constantly close to the theoretical limit of a perfectly curved crystal.

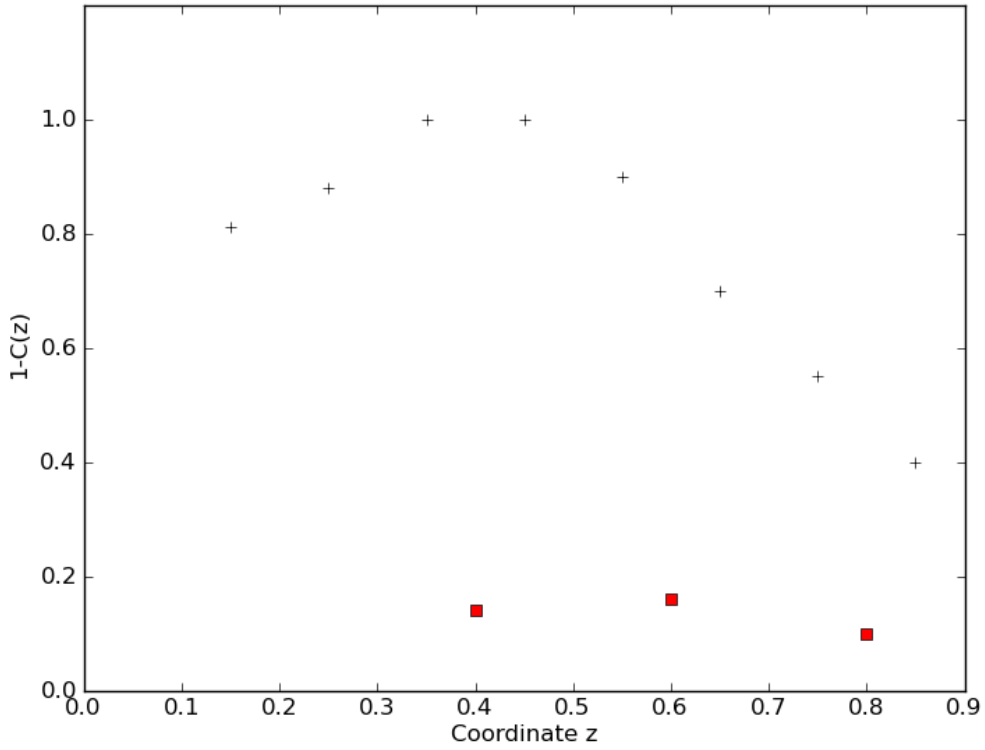

Figure 3.18: Contribution of mosaicity vs. depth for perpendicular (black crosses) and parallel cases (red squares), respectively.

Diffraction efficiency was studied vs. photon energy. Figures 3.19 and 3.20 show the response of sample S71, measured with the beam parallel and perpendicular to the grooves. In the parallel case (Fig. 3.19), experimental efficiency is very close to its theoretical limit over about 15 arcsec angular spread, namely the morphological curvature of the sample. With the beam perpendicular (Fig. 3.20) to the grooves, efficiency is slightly lower than its theoretical limit but still higher than the theoretical efficiency for a mosaic crystal.

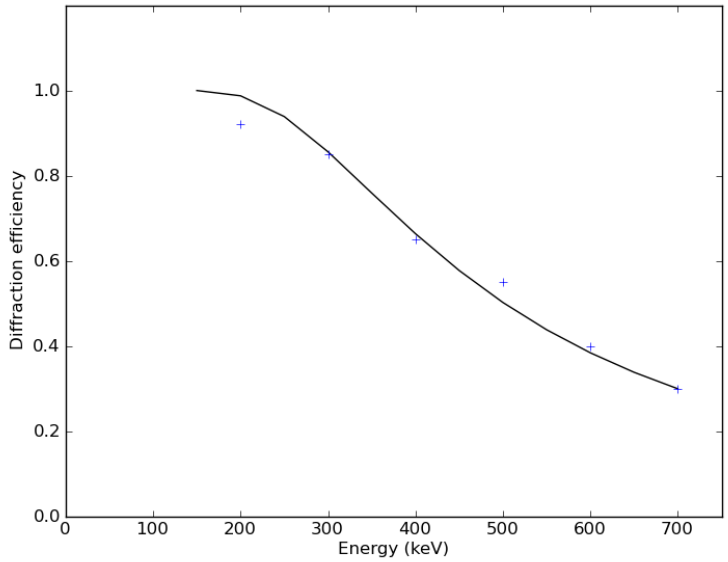

Figure 3.19: Experimental (black crosses) and theoretical (black line) diffraction efficiencies vs. energy, for parallel case for crystal S71. RCs were carried out at 0.8 mm from the grooved face.

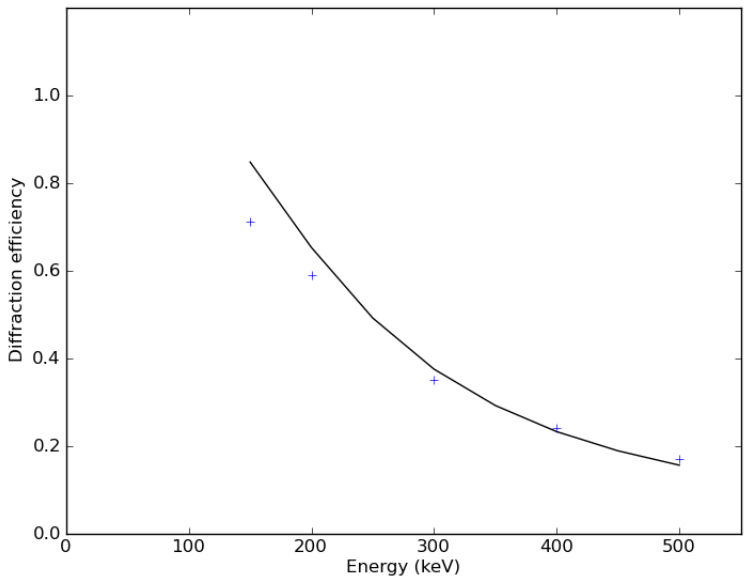

Figure 3.20: Experimental (black crosses) and theoretical (black line) diffraction efficiencies vs. energy, for perpendicular case for crystal S71. RCs were carried out at 0.85 mm from the grooved face.

3.4.2. Ge crystal 2_G32

Ge crystal 2_G32 was measured at 300 keV with the beam penetrating the sample through its 9.8×2 mm^2 surface at different depths from the grooved side and quasi-parallel to the (111) planes. Morphological bending angle of the sample was 42.4 arcsec along beam direction. RCs of the sample in Fig. 3.21 show that diffraction efficiency was about 61%. Though this is still a good performance, it is less than the 93% theoretically expected, this fact being probably due to a non-perfect crystalline quality of the base material.

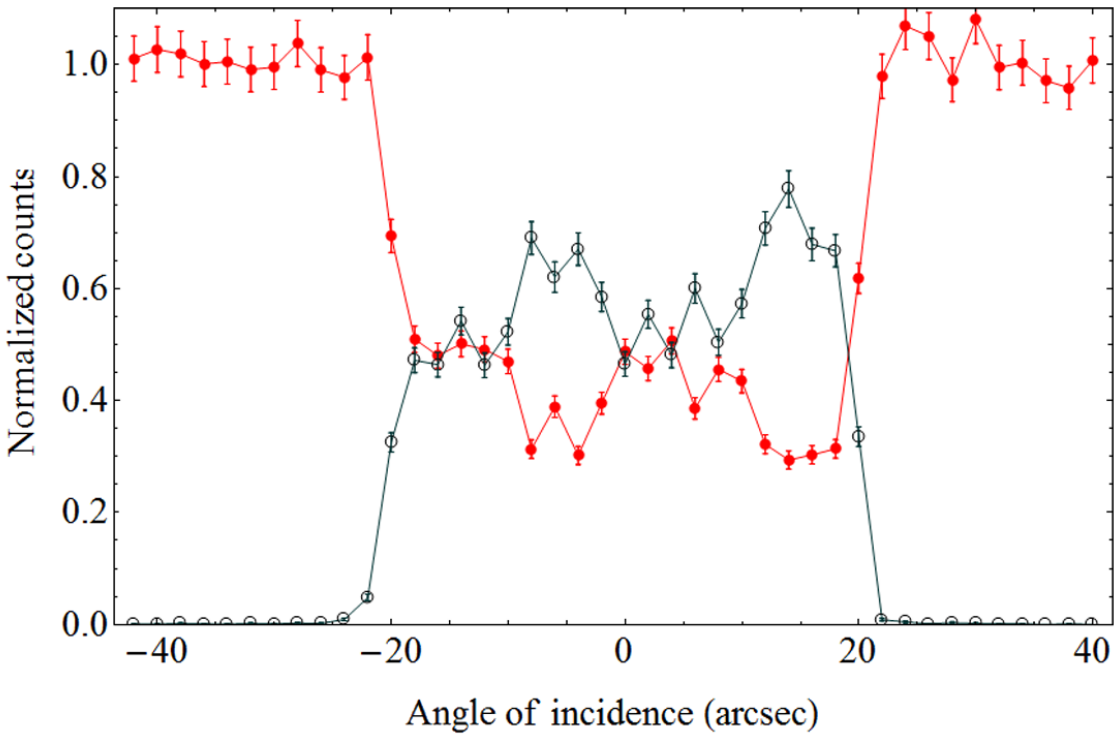

Figure 3.21: RCs of Ge crystal 2_G32 measured at z = 0.65 mm, in "geometry 1" with respect to the beam. Beam energy was set at 300 keV. Diffraction efficiency was 61% [3.30].

3.4.3. Stack-1

In order to verify the alignment of the (111) diffracting planes in the stack, the multi-crystal was initially analyzed with the beam penetrating through its 45×10 mm^2 surface at different distances from the edge of the sample, parallel to the $(2\bar{2}0)$ planes (see Fig. 3.11a) and in diverging mode, i.e., the beam left the concave side of the stack and diverged. Figs. 3.22a, b, c, d and e show the diffraction patterns while Figs. 3.22f, g, h, i and j highlight the cross-section area of the focal spot due to diffraction by $(2\bar{2}0)$ planes. As can be seen, a single and well-defined spot on the detector is shown up to 10 mm from the other side of the stacking, i.e., under X-ray diffraction the stack of plates behaves as it were a single crystal. Thus, it turned out that $(2\bar{2}0)$ planes are coplanar, this fact meaning that the critical misalignment of the (111) crystallographic planes can be excluded. Moreover, at each position, the FWHM of the Gaussian intensity profile satisfies Eq. (1.36.) for the case of diverging mode. At nearly 8 mm from the other edge of the multi-crystal and throughout its remaining side, the profile of the focal spot was no longer a single Gaussian but another diffraction peak appeared at an angle shifted by nearly 27 arcsec (1.15 mm), meaning that Bragg angle depends on each plate in the stack. In fact, two of the plates were misaligned by nearly 27 arcsec probably because they were not properly bound near the edge of the stack.

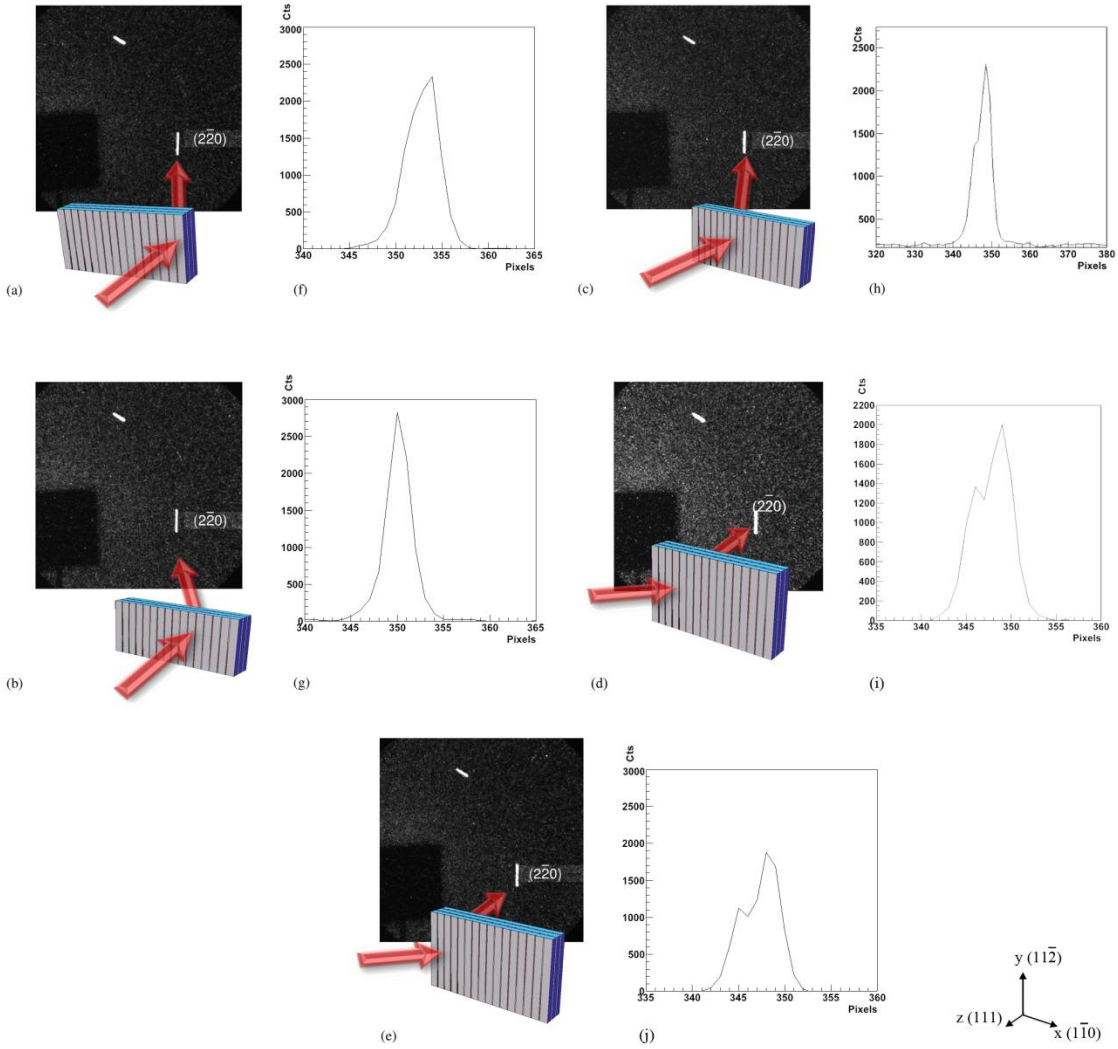

Figure 3.22: Diffraction patterns obtained with the beam (10×1 mm^2) quasi-parallel to the (2$\bar{2}$0) crystallographic planes at several distances from the edge of the sample, i.e., at (a) x = 1 mm, (b) x = 21 mm, (c) x = 35 mm, (d) x = 39 mm, (e) x = 43 mm, associated with horizontal average cross-sections corresponding to the (2$\bar{2}$0)-diffraction (f, g, h, i and j). A single and well-defined focal spot is recorded up to 35 mm from the edge of the Si stack. Misalignment of (2$\bar{2}$0) planes, as visible by the presence of another diffraction peak, starts at nearly 8 mm from the other edge of the multi-crystal and keeps constant throughout its remaining side [3.27].

Although bending of (111) diffracting planes induces a shift of the peak position with respect to the position on the stack, no detection of the bending angle of the stack was obtained because higher accuracy should be needed.

The stack was then investigated with the beam parallel to the (111) diffracting planes (see Fig. 3.11b), penetrating the sample through its 3×10 mm^2 surface. The first analysis was done with the beam 10×10 mm^2, in converging mode with respect to the (111) planes, i.e., the beam left the convex side of the (111) planes and converged. In fact, this measurement represents the scheme for functional operation of a multi-crystal as an optical component in a Laue lens, through diffraction by (111) planes (see Fig. 3.2b). Results in Figs. 3.23a and b show the diffraction spots from several crystallographic planes and the cross-section area corresponding to the (111) planes. As can be noticed, diffraction from (111) planes results in a single and well-defined focal spot on the detector, meaning that these planes are coplanar and that the critical misalignment can be excluded throughout the whole volume of the sample. The multi-crystal behaves as it were a single crystal

from the point of view of diffraction by (111) planes, hence this performance highlights that the stack of grooved Si crystals can efficiently work as optical element for satellite-borne experiments with a Laue lens. Furthermore, the FWHM of the intensity profile due to (111) planes is in agreement with Eq. (1.36.), i.e., 1.75 mm (5 pixels).

When the beam impinged onto the stack in diverging mode with respect to the (111) planes, X-ray diffraction from CDP resulted in a nearly well-defined focal spot on the detector (Fig. 3.23c), the width of the intensity profile (Fig. 3.23d) being approximately 4 mm (10.5 pixels).

Nevertheless, although (111) planes are not critically misaligned, diffraction from $(11\bar{2})$ planes resulted in three focal spots, meaning that all the plates probably suffer from some misalignment as depicted in Figs. 3.3c and d. In fact, all the plates were misaligned by nearly 30 arcsec each other probably because they were not perfectly bound. However, this misorientation did not affect the efficiency of the (111) diffraction, showing that a tolerance is allowed in the alignment of the CDP crystals inside the stack while non affecting the total performance.

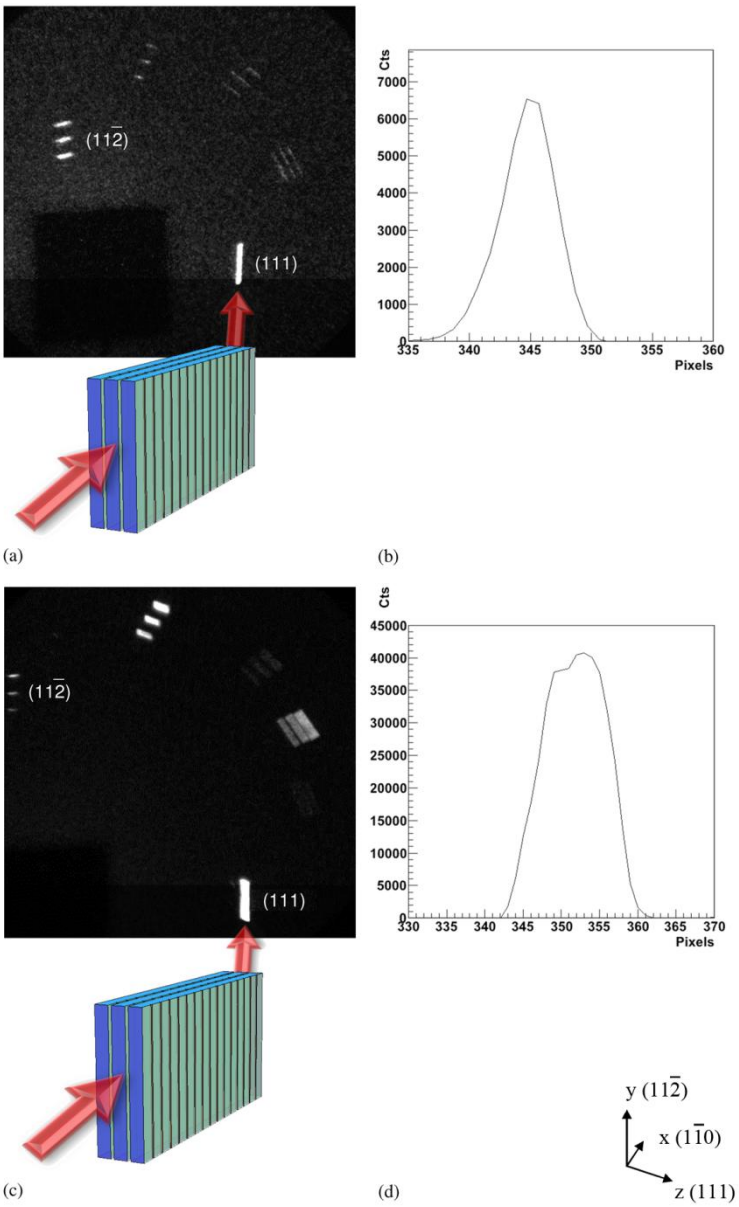

Figure 3.23: Diffraction patterns recorded with the beam 10×10 mm^2, quasi-parallel to the convex side of (111) crystallographic planes (a). Horizontal average cross-section of the focal spot corresponding to (111)-diffraction is highlighted (b). Notice that diffraction from (111) planes results in a single and well-defined focal spot (FWHM = 1.75 mm) on the detector. As the beam (10×10 mm^2) is in diverging mode with respect to the CDP (c and d), the focal spot from (111) planes is nearly well-defined, its FWHM being approximately 4 mm. Here the diffraction peaks correspond to energies of 247 keV and 169 keV for converging and diverging mode, respectively. On the other hand, diffraction from (11$\bar{2}$) planes results in three focal spots, thus all the plates probably suffer from some misalignment as depicted in Figs. 5c and d. However, this misalignment does not affect the efficiency of X-ray diffraction by (111) planes [3.27].

It is worth noting that for the converging configuration the focal spot on the detector was smaller than for the diverging case. This result is representation that the stack should be positioned with the beam impinging onto the convex side of CDP for focusing in a Laue lens.

The alignment of the plates in the stack was also investigated by X-ray characterization of the multi-crystal with the beam being 10×0.5 mm^2, quasi-parallel to the convex side of (111) planes and at several distances from the edge of the sample. Results in Figs. 3.24a, b, c and d confirm that the

stacking of Si crystals behaves as it were a single crystal and no critical misalignment of the CDP occurs.

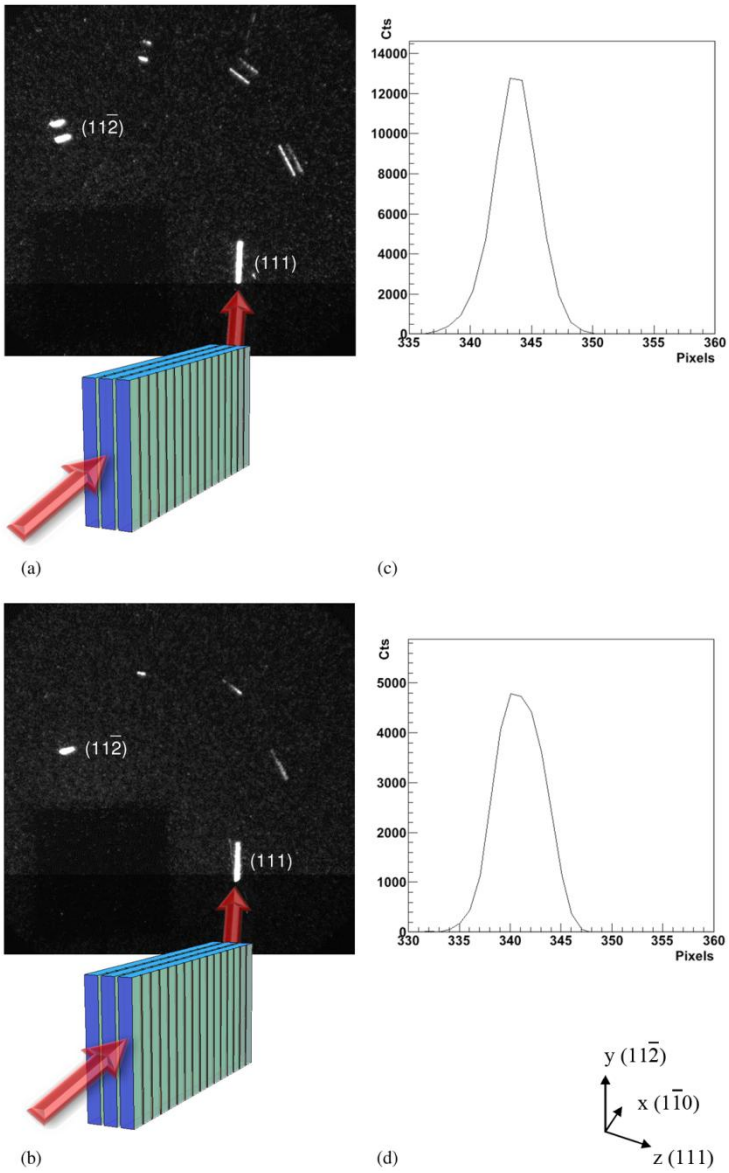

Figure 3.24: Diffraction patterns recorded with the beam 10×0.5 mm^2, incident quasi-parallel to the convex side of (111) planes at several distances from the edge of the stack, i.e., at (a) z = 1.5 mm, (b) *z* = 2.5 mm. The horizontal cross-sections (c and d) of the profile due to (111)-diffraction confirm that the stack behaves as it were a single crystal. For both cases, the energy at which diffraction by (111) planes occurs is about 250 keV [3.27].

3.4.4. Stack-2

The alignment of the (111) diffracting planes in stack_2 has been verified by measuring the multi-crystal with the beam penetrating through its 45×10 mm^2 surface at different distances from the edge of the sample, parallel to the (2$\bar{2}$0) planes (see Fig. 3.11a) and in diverging mode. Figs. 3.25a, b, c, d, e, f, g and h show the diffraction patterns while Figs. 3.25i, l, m, n, o, p, q and r highlight the cross-section area of the focal spot due to diffraction by (2$\bar{2}$0) planes. As can be seen, a single and well-defined spot on the detector is shown up to nearly 20 mm from the edge of the

stack, i.e., under X-ray diffraction the stack of plates behaves as it were a single crystal. Hence, it resulted that $(2\bar{2}0)$ planes are coplanar, meaning that the critical misalignment of the (111) crystallographic planes can be excluded at least up to nearly the middle of the sample. Moreover, at each position, the FWHM of the Gaussian intensity profile satisfies Eq. (1.36.) for the case of diverging mode. At nearly 24 mm from the other edge of the multi-crystal and throughout its remaining side, the profile of the focal spot was no longer a single Gaussian but another diffraction peak appeared. In fact, the plates were misaligned by nearly 40 arcsec probably because they were not perfectly bound, thus Bragg angle depends on each plate in the stack.

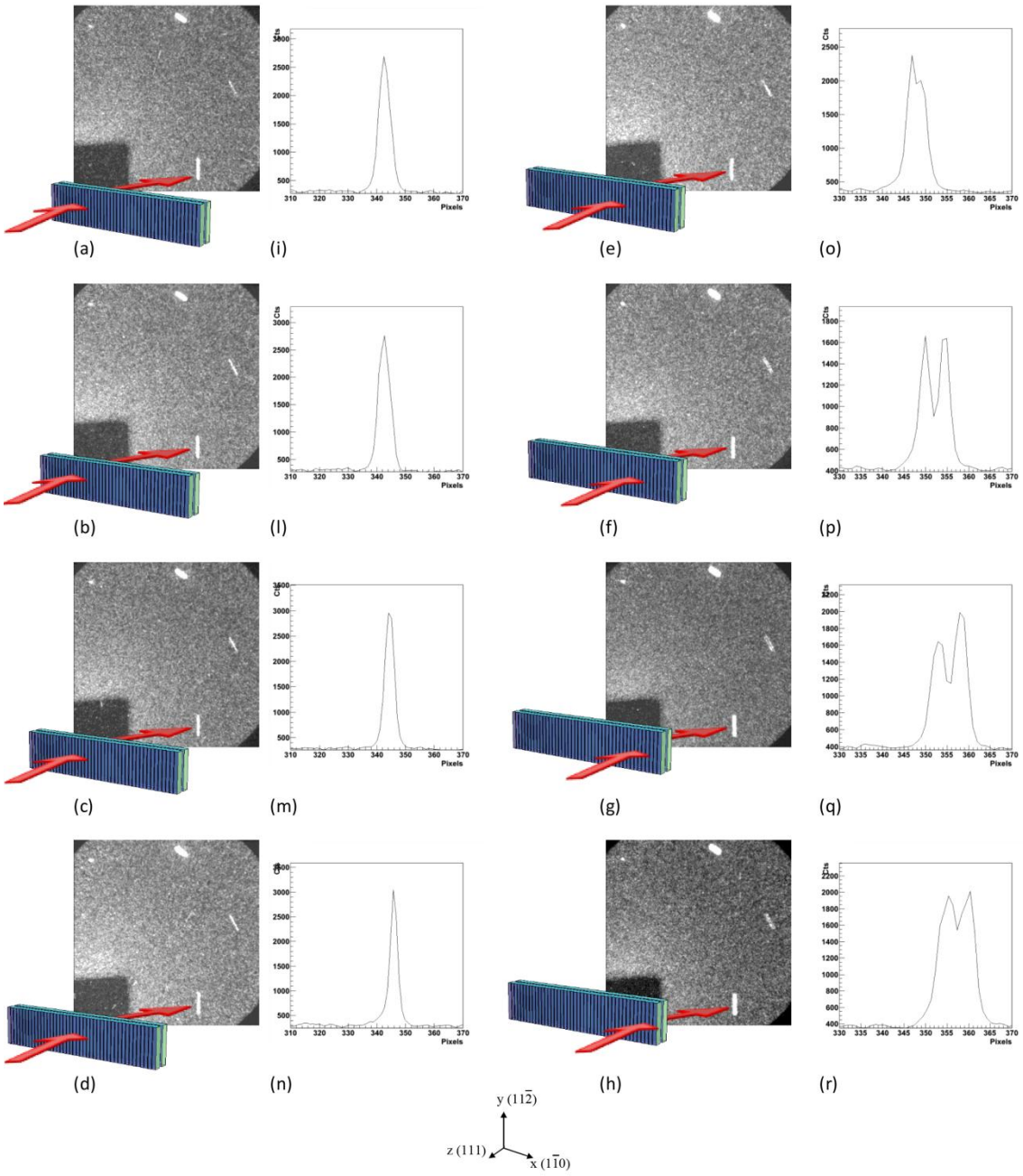

Figure 3.25: Diffraction patterns obtained with the beam (10×1 mm^2) quasi-parallel to the $(2\bar{2}0)$ crystallographic planes at several distances from the edge of the sample, i.e., at (a) x = 1 mm, (b) x = 4 mm, (c) x = 12 mm, (d) x = 16 mm, (e) x = 20 mm, (f) x = 26 mm, (g) x = 32 mm, (h) x = 44 mm, associated with horizontal average cross-sections corresponding to the $(2\bar{2}0)$-diffraction (i, l, m, n, o, p, q and r). A single and well-defined focal spot is recorded up to 20 mm from the edge of the Si stack. Misalignment of $(2\bar{2}0)$ planes, as visible by the presence of

another diffraction peak, starts at nearly 24 mm from the other edge of the multi-crystal and keeps constant throughout its remaining side.

This stack was then analyzed with the beam parallel to the (111) diffracting planes (see Fig. 3.11b), penetrating the sample through its 2×10 mm^2 surface. In order to demonstrate the functionality of the stack as optical component onto a Laue lens (see Fig. 3.2b), the first analysis was done with the wide beam 10×10 mm^2, in converging mode with respect to the (111) planes. Results in Figs. 3.26a and b show the diffraction spots from several crystallographic planes and the cross-section area corresponding to the (111) planes. As can be seen, diffraction from (111) planes results in a single and well-defined focal spot on the detector, showing that the stack behaves as it were a single crystal from the point of view of diffraction by (111) planes. This performance is a further representation that a stack of grooved Si crystals can efficiently work as optical element for satellite-borne experiments with a Laue lens. Furthermore, the FWHM of the intensity profile due to (111) planes is in agreement with Eq. (1.36.).

As for the previous case, although (111) planes are not critically misaligned, diffraction from $(11\bar{2})$ planes resulted in two spots on the detector, meaning that Bragg angle depends on each plate in the stack. In fact, all the plates probably suffer from some misalignment as depicted in Figs. 3.3c and d. However, this misalignment did not affect the performance of the (111)-diffraction, showing that a tolerance is allowed in the alignment of the CDP crystals inside the stack.

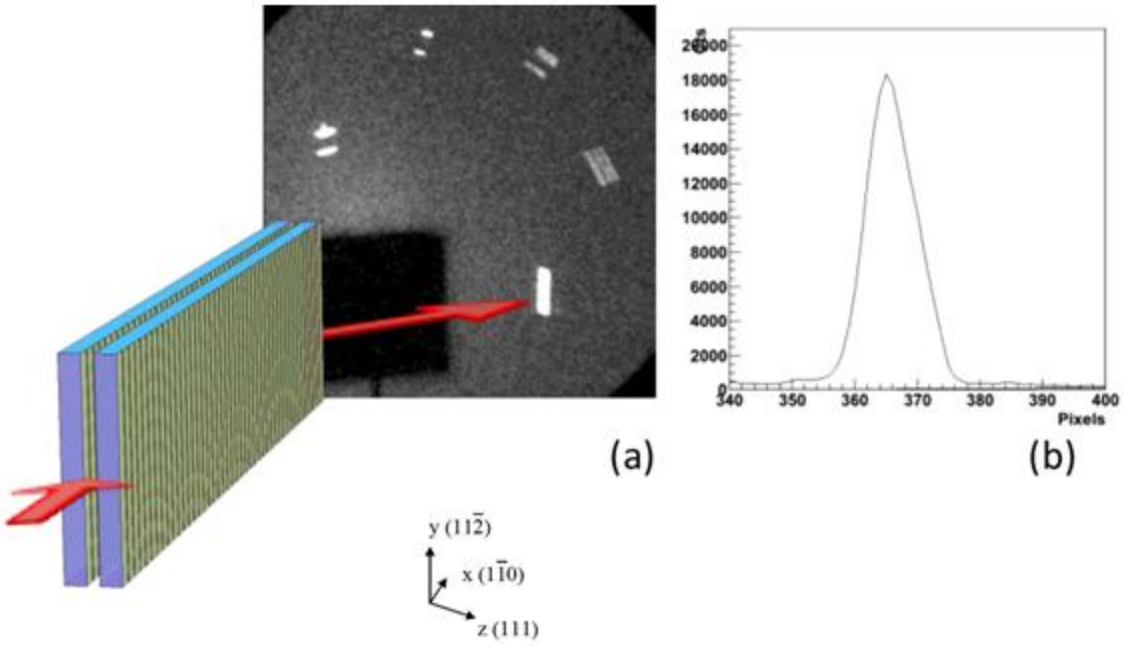

Figure 3.26: Diffraction patterns recorded with the beam 10×10 mm^2, quasi-parallel to the convex side of (111) crystallographic planes (a). Horizontal average cross-section of the focal spot corresponding to (111)-diffraction is highlighted (b). Notice that diffraction from (111) planes results in a single and well-defined focal spot on the detector. On the other hand, diffraction from $(11\bar{2})$ planes results in two focal spots, thus all the plates probably suffer from some misalignment as depicted in Figs. 5c and d. However, this misalignment does not affect the efficiency of X-ray diffraction by (111) planes.

The alignment of the plates in the stack was then investigated by X-ray characterization of the sample with the beam being 10×0.5 mm^2, quasi-parallel to the convex side of (111) planes and at several distances from the edge of the sample. Results in Figs. 3.27a, b, c, d and e show the diffraction patterns from several crystallographic planes while the cross-section area of the spot due to (111)-diffraction is highlighted in Figs. 3.27f, g, h, i and j. As pointed out by the presence of the double peak, critical misalignment of the CDP occurred up to nearly 0.75 mm from the edge of the sample while the stack behaved as it were a single crystal throughout its remaining side. Indeed, a well-defined and single spot was produced.

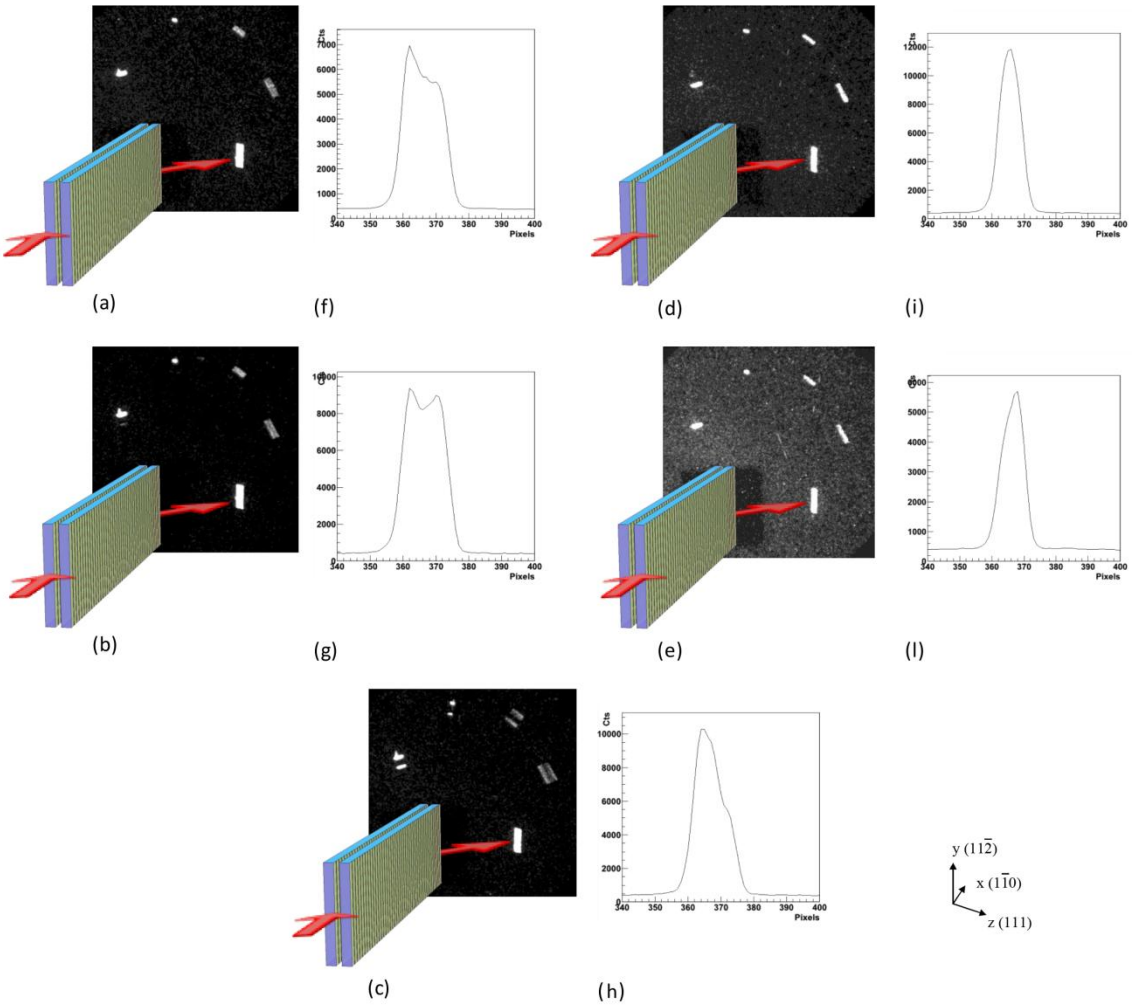

Figure 3.27: Diffraction patterns recorded with the beam 10×0.5 mm^2, incident quasi-parallel to the convex side of (111) planes at several distances from the edge of the stack, i.e., at (a) z = 0 mm, (b) z = 0.5 mm, (c) z = 1 mm, (d) z = 1.5 mm (e) z = 2 mm. The horizontal cross-sections (f, g, h, i and l) of the profile due to (111)-diffraction show that critical misalignment of the CDP occurred up to nearly 0.75 mm from the edge of the sample while the stack behaved as it were a single crystal throughout its remaining side.

3.4.5. Quasi mosaic Si crystal G3

A square crystal plate subject to mechanical moments applied along x- and y-axis directions undergoes primary deformation as depicted in Fig. 3.28.

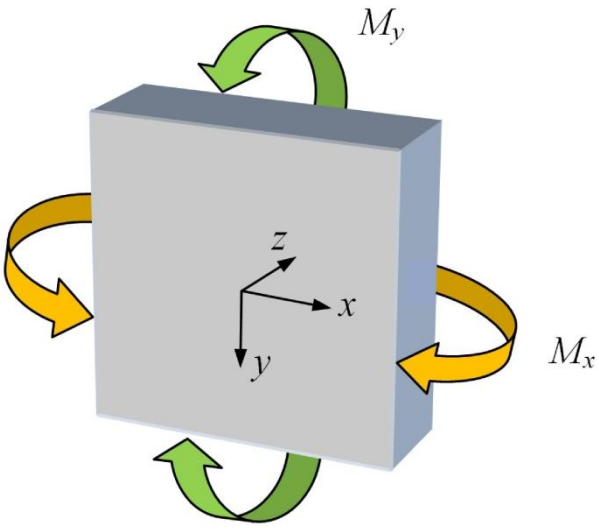

Figure 3.28: Schematic representation of a square crystal plate. Bent arrows symbolize applied moments M_x and M_y [3.29].

In order to verify the primary curvature of the quasi mosaic sample as a result of surface grooving, analysis of its $(11\bar{2})$ crystallographic planes has been investigated at several positions along x and y axes, by usage of the high-resolution X-ray diffractometer at SSL. For every step, the crystal was rotated around the incidence angle where Bragg diffraction occurs, thus recording the RC. As can be noticed in Figs. 3.29 and 3.30, due to CDP of the crystal, a shift of the peak position occurs with respect to the position on the sample along x and y axes, respectively. It resulted that the whole angular spread, along both directions, was very close to the morphological curvatures of the crystal, as measured by optical profilometry. Since primary curvature is responsible for focusing, this evidence is a representation that the capability of quasi mosaic crystals to focalize diffracted radiation can be very well controlled by simply imparting a selected curvature to the sample.

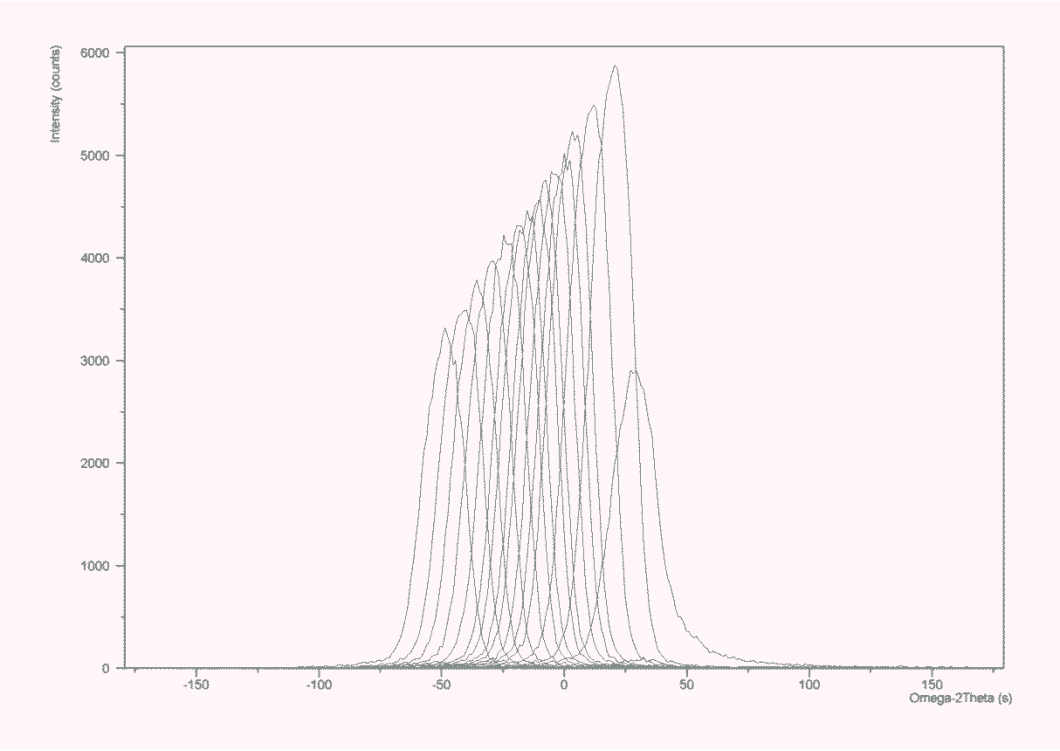

Figure 3.29: Series of RCs of the QM sample vs. *x* obtained with the HRXRD at SSL . As can be noticed, a shift of the peak position occurs with respect to the position on the sample. The whole angular spread was very close to the morphological primary curvature of the crystal along *x*-direction, as measured by optical profilometry on the $(11\bar{2})$ face.

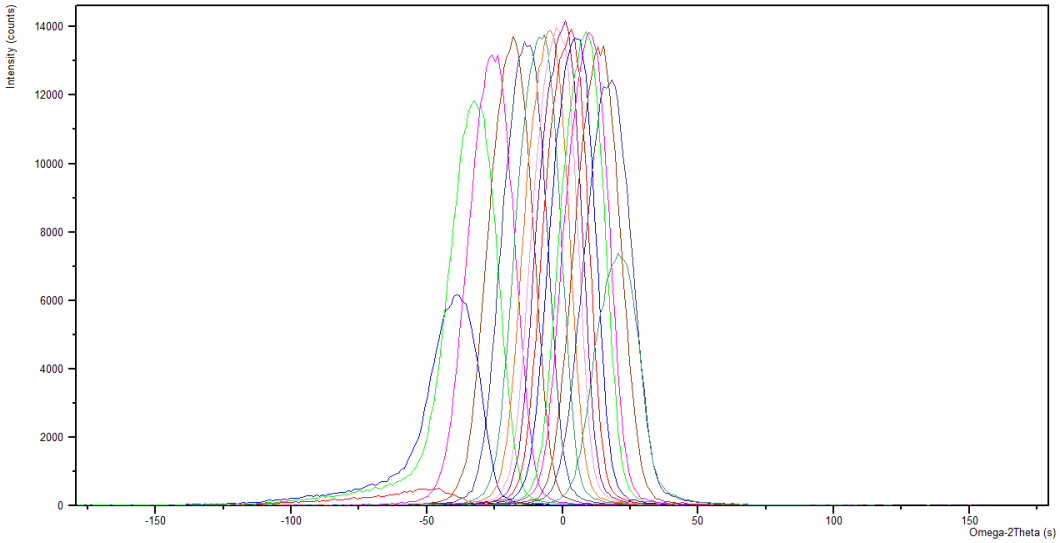

Figure 3.30: Series of RCs of the QM sample vs. *y* obtained with the HRXRD at SSL. As can be noticed, a shift of the peak position occurs with respect to the position on the sample. The whole angular spread was very close to the morphological primary curvature of the crystal along *y*-direction, as measured by optical profilometry on the $(11\bar{2})$ face.

As highlighted in Ref. [3.30], characterization of the quasi-mosaic Si sample at Digra facility aimed to measure diffraction efficiency of the crystal due to quasi mosaic curvature of the (111) diffracting planes. Hence, the sample was tested by performing RCs, with the photon beam hitting the $(11\bar{2})$ surface of the sample and being diffracted by curved (111) planes. Diffraction efficiency

was calculated on the center of the sample and the experimental diffracted RC is reported in Fig. 3.31. The gray area represents the expected result as calculated by taking into account the experimental uncertainties. Instead, dashed black line represents diffraction efficiency if quasi-mosaic curvature were absent. As highlighted, due to quasi mosaic curvature of diffracting planes, a raise in diffraction efficiency occurs. This fact confirms the presence of quasi mosaicity within the sample as a result of surface grooving.

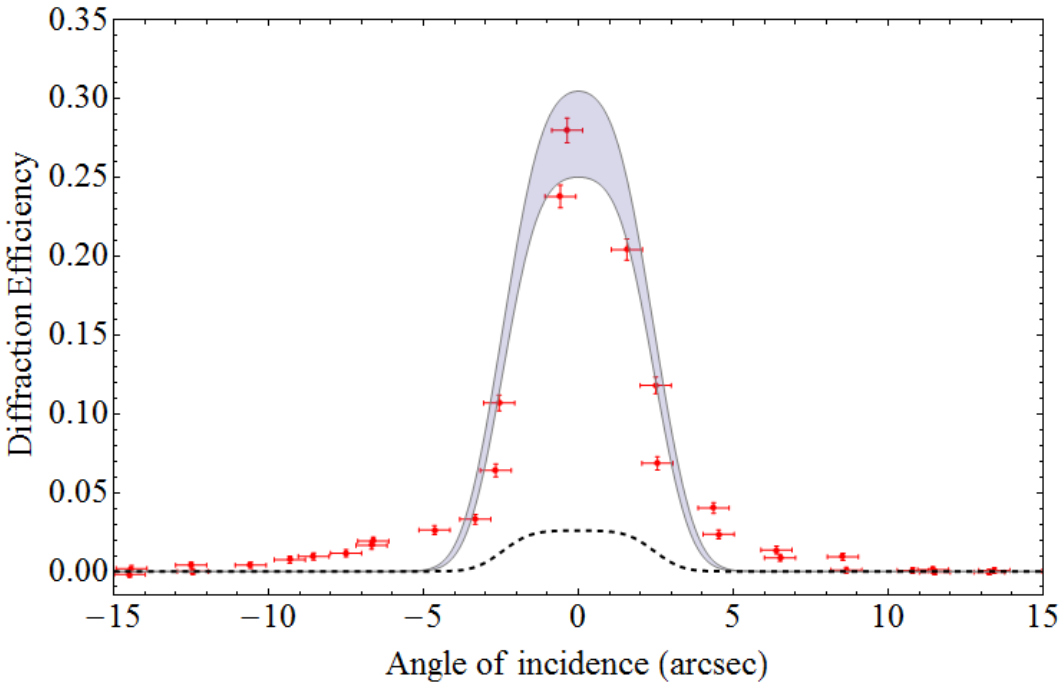

Figure 3.31: Experimental and theoretical RCs for the QM Si sample in "geometry 2" vs. impinging photons (see Fig. 3.2c). Red circles plot the intensity of measured diffracted beam with their uncertainty bar. The gray area represents the expected result as calculated by taking into account the experimental uncertainties. Dashed black line represents diffraction efficiency if QM curvature were absent [3.30].

In previous sections main experimental results on Si and Ge curved crystals fabricated by surface grooving technique, for realization of a high-resolution focusing Laue lens have been shown and discussed. The technology of fabrication of the crystals is currently well-established for Si and Ge, thereby it can be readily applied to build up a Laue lens.

Two different geometries of the CDP crystals for Laue lens have been highlighted. Both geometries have been tested vs. experiment, yielding significant performance. Indeed, a stack of grooved crystals was shown to efficiently work as optical element for wide-passband focusing through a Laue lens, thus demonstrating the functionality of "geometry 1". On the other hand, a quasi-mosaic crystal, useful for "geometry 2", proved to highlight very high diffraction efficiency due to QM curvature. In this case, the size of the focal spot of the photons diffracted can be significantly small. Thus, QM crystals of this kind are proposed for high-resolution focusing through a Laue lens.

3.5. Preliminary study of a Laue lens for nuclear medicine

3.5.1. General background and experimental layout for medical imaging

Nowadays, radioactive materials used as a diagnostic tool can identify the status of a disease and minimize the need for surgery by reducing the risks from postoperative infection. Nuclear imaging is usually performed by injecting a radiopharmaceutical into the patient and measuring the intensity distribution of gamma radiation emitted from the patient's body.

Short-lived radioisotopes are preferred for use in these tracers to minimize the radiation dose to the patient. In most cases, these radioisotopes decay to stable elements within minutes, hours, or days, allowing patients to be released from the hospital in a relatively short time. The radioisotope used in about 80 percent of nuclear diagnostic procedures is Tc-99m, emitting gamma rays with a characteristic energy of 140 keV. The penetrating properties of its gamma rays and its short half-life (6-hours) help in reducing risk to the patient from more prolonged radiation exposure. Short-lived radionuclides such as technetium-99m, gallium-67, and thallium-201 are often used to diagnose the functioning of the heart, brain, lung, kidney or liver. Cancerous cells have high growth rate and multiply very rapidly. The radioactive isotope injected into the body of the patient normally migrates to high growth rate locations and will incorporate in this new growth, thus the tumour location can be identified from the region of high radioactivity.

Diagnostic techniques in nuclear medicine usually involves usage of a gamma camera which can view organs from many different angles. The camera builds up an image from the points from which radiation is emitted; this image is enhanced by a computer and displayed on a monitor for indications of abnormal conditions.

The development of CDP crystals for focusing of gamma rays will find significant application in the field of medical imaging. Indeed, CDP crystals are expected to have both high diffraction efficiency and relatively broad energy bandwidth and would be capable of detecting the radiopharmaceuticals that emit 50–200 keV gamma rays which are generally used in diagnostic molecular imaging. CDP crystals would be positioned as optical elements onto a Laue lens which would improve gamma-ray detection with better resolution and lead to a lower radioactive dose imparted to the patient because tomography scanning would not be needed. As an example, Fig. 3.32 shows the experimental arrangement of a treatment method based on a Laue lens.

Development of Laue lens in focusing gamma rays in nuclear imaging has already been studied by Roa [3.36]. In his experimental approach CDP crystals, obtained by concentration-gradient technique, were used to diffract gamma rays from a radioactive source and it was found that with the help of this approach one can increase the diffraction efficiency and energy bandwidth by a factor of 5 compared to mosaic crystals.

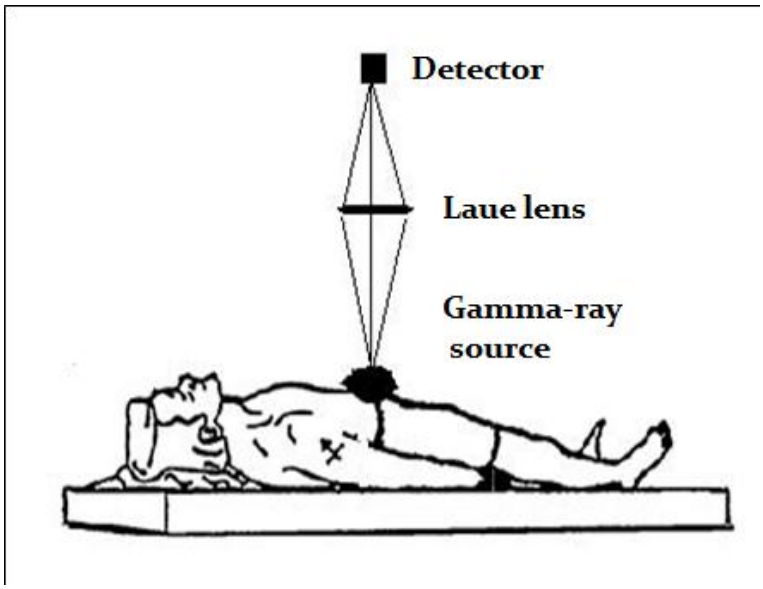

Figure 3.32: Pictorial representation of the clinical treatment method. A biological compound carrying a radioactive nucleus is injected in the human body and is readily incorporated in cancer cells. Emitted gamma radiation is then diffracted by a Laue lens toward a small focal point on a detector's sensitive area [3.37].

3.5.2. Fabrication of bent crystals by Low Energy Plasma Enhanced Chemical Vapor. Deposition and preliminary results by optical profilometry

In the present study curved crystals were obtained by Low Energy Plasma Enhanced Chemical Vapour Deposition (LEPECVD) technique. The significant features of this technique are wide range of epitaxial growth rate at low substrate temperature and high reproducibility [3.38]. More details of this method will be given in next chapter.

With the use of LEPECVD, a crystalline germanium film was grown on the surface of a silicon substrate (100) which is tilted 6˚ towards [111]. The thickness of the silicon substrate was 400 μm. Sample details are given in Table 3. The importance of this method was to produce intrinsically curved crystals without the usage of any mechanical means. The sample got curved due to the lattice mismatch between Si and Ge and the different thermal expansion coefficients [3.39]. Thanks to this technique, curved crystals can be obtained by depositing tensile or compressive films over bulky substrates. This technique was chosen for its reproducibility and its capability to bend the crystal to the desired curvature. Bending is strong due to high stress imparted which can be matched with stability without delamination.

Table 3: Details of the samples with the different thickness of Ge

Sample	Film thickness (nm)
1	505
2	762
3	1122
4	1800

The radius of curvature was measured with the help of surface profilers Wyko NT1100. As an example, the optical surface profilometry of sample 4 is shown in Fig. 3.33. The curvature has a significant effect on the diffraction efficiency of the crystal.

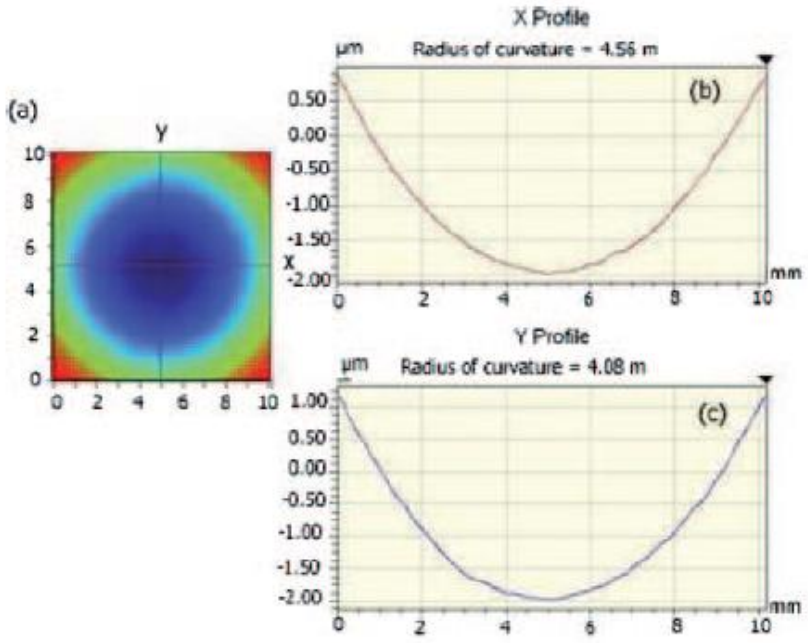

Figure 3.33: Optical surface profilometry of sample 4. (a) gives the false-colour representation of the deformation. The deformation pattern cross-section along the x (b) and y (c) directions is seen with the two curvatures. The isotropic bending was achieved.

The bent crystal samples of different thickness of germanium over the silicon substrate were grown and characterized. As the thickness of deposition of Ge is increased, the radius of curvature is decreased. Table 4 shows the variation of the curvature radius along the y direction with respect to the different thickness of Ge.

Table 4: Variation of the curvature radius with respect to the different thickness.

Sample	Radius of curvature (m)
1	24.68
2	10.83
3	9.21
4	4.08

The significance of this study is that it is easy to tailor the curvature to a wanted curvature after deposition of a suitable thickness and highly bent crystals can be produced by such a technique. All the samples have been produced and optically characterized at Sensor and Semiconductor Laboratory (Ferrara, Italy).

3.5.3. Simulation to optimize crystal diffraction properties

Performance of Laue medical lens relies on crystals as its most important elements. Hence, in order to maximize diffraction properties of the lens, crystal parameters have to be optimized. For this aim, a simulation code has been developed. This has been worked out through Python high-level programming language, and it is specifically designed for bent crystals. Indeed, the software describes diffraction in crystals with CDP and generates the physical quantities which are typically used to characterize the diffraction properties of a crystal, i.e., diffraction efficiency and reflectivity as defined in [3.15]. The former is the ratio of the diffracted beam intensity over the transmitted one when no diffraction condition occurs and the latter is the ratio of the diffracted beam intensity to the incident beam intensity. Reflectivity can be determined by simply multiplying efficiency to the attenuation factor due to linear absorption in the sample. Moreover, for a given atomic number and reflection plane, the software code computes the thickness maximizing reflectivity and efficiency as a function of photon energy and angular spread, this latter being the bending angle of the crystal. Crystal thickness is a crucial parameter for optimization of a Laue lens. In Laue geometry, this is considered as the part of the crystal which is totally traversed by the radiation, giving the contribution to photon diffraction. In medical imaging applications of Laue lens, the thickness of crystal element gives the spatial resolution of the whole lens. Thus, this feature has to be taken into account when maximizing reflectivity and diffraction efficiency of the crystals composing the lens.

As a result of simulations, 5 mm thickness of sample 1 would diffract 140.5 keV of Tc-99m featuring 83% diffraction efficiency (which turns into a reflectivity of 42%), over 42 arcsec angular spread. Crystalline planes of Ge have been considered for diffraction. Hence, provided that the crystalline planes of the sample are curved, high-efficiency diffraction of gamma rays would be attained, with higher spatial resolution than for currently operating devices.

3.6. References

[3.1] N. Lund, *Exp. Astron.* **2**, 259–273 (1992)
[3.2] D. Pellicciotta et al., *IEEE Trans. Nucl. Sci.* **53**, 253–258 (2006)
[3.3] A. Pisa et al., *Exp. Astron*. **20**, 219–228 (2005)
[3.4] G. Weidenspointner et al., *NewAR*. **52**, 454–456 (2008)
[3.5] M. Leventhal et al., *Astrophys. J.* **225**, L11 (1978)
[3.6] D. D. Clayton, *Nat. Phys. Sci.* **244**, 137 (1973)
[3.7] D. D. Clayton and F. Hoyle, *Astrophys. J.* 187, L101 (1974)
[3.8] N. Prantzos, and M. Casse, *Astrophys. J.* **307**, 324 (1986)
[3.9] R. Ramaty and R.E. Lingenfelter, *Nature.* **278**, 127 (1979)
[3.10] N. Guessoum et al., *Astron. Astrophys.* **457**, 753 (2006)
[3.11] K. S. Cheng et al., *Astrophys. J.* **645**, 1138 (2006)
[3.12] T. Totani, *Astron. Soc. Jpn*. **58**, 965 (2006)
[3.13] C. Boehm et al., *Phys. Rev. Lett.* **92**, 101301/1 (2004)
[3.14] N. Barrière et al., PoS(INTEGRAL 2010), 108
[3.15] N. Barriere et al., *J. Appl. Crystallogr*. **42** (5), 834 (2009)
[3.16] W. H. Zachariasen, *Theory of X-ray Diffraction in Crystals*. New York: J. Wiley and Sons, (1945), and references therein.
[3.17] N. Barriere et al., *J. Appl. Crystallogr*. **43**, 1519 (2010)
[3.18] V. Bellucci et al., *Exp. Astron*. **31**, 45-58 (2011)
[3.19] H. Kawata et al., *Nucl. Intrum. Meth. A*, **404**, 467–468 (2001)
[3.20] R. K. Smither et al., *Exp. Astron.* **20**, 201 (2005)
[3.21] N. V. Abrosimov, *Exp. Astron.* **20**, 185 (2005)
[3.22] A. Erko et al., *Nucl. Instrum. Meth. A*, **374**(3), 408 (1996)
[3.23] S. Keitel et al., *Acta Cryst. A*, **55**, 855 (1999)
[3.24] V. Bellucci et al., *Thin Solid Films*, **520** (3), 1069-1073 (2011)
[3.25] R. Camattari et al., *Experimental analysis and modeling of self-standing curved crystals for focusing of x-rays*, submitted to Meccanica (2012)
[3.26] A. Authier, *Dynamical Theory of X-ray Diffraction*, Oxford University Press (2001)
[3.27] I. Neri et al., *Ordered stacking of crystals with adjustable curvatures for hard x- and gamma-ray broadband focusing*, submitted to *J. Appl. Cryst*., (2012)
[3.28] I. Neri et al. *Proceeding of Spie*, 844334, doi:10.1117/12.926191 (2012)
[3.29] V. Guidi et al., *J. Appl. Cryst*. **44**, 1255–1258 (2011)
[3.30] V. Guidi et al., *accepted for publication in Nucl. Instrum. Meth. B* (2013)
[3.31] O. Sumbaev, *Soviet Phys. JETP*, **5**, 1042–1044 (1957)
[3.32] Y. Ivanov et al., *JETP Letters*, **81**, 99–101 (2005)
[3.33] W. Scandale et al., *Phys. Rev. Lett*. **98**, 154801 (2007)
[3.34] W. Scandale et al., *Phys. Rev. ST Accel. Beams*, **11**, 063501 (2008)
[3.35] V. Bellucci et al., *Il Nuovo Cimento*, **34** C , 503-511 (2011)
[3.36] D. Roa et al., *Exp. Astron*., **20**, 229 (2005)
[3.37] I. Neri et al., *Il Nuovo Cimento*, **34** C , 461-467 (2011)
[3.38] C. Rosenblad et al., *Thin Solid Films* **336**, 89-91 (1998)
[3.39] V. Guidi et al., *Thin Solid Films* **520**, 1074-1079 (2011)

4. X-ray characterization of heteroepitaxial Ge layers as virtual substrates for solar cell applications

4.1. Ge virtual substrates

Nowadays, the strong technological development and continuous research in photovoltaic solar energy have led to significant advances for solar cells. Currently, the technology that provides the best prospects is represented by the concentration photovoltaics systems based on spectral separation of the solar radiation, which focalize the different wavelengths of the electromagnetic radiation toward small cells having high efficiency: the reduced amount of photovoltaic material, the better exploitation of solar radiation and the potential of reducing the cost of optical collectors make these systems excellent candidates for power generation on a large scale.

The cells used in these systems are typically made with different materials belonging to the family of compounds III-V, because these are the ones that present the higher yields: as an example with the multijunction structure InGaP-InGaAs-Ge, with energy gap equal to 1,84-1,42-0,7 eV, one can achieve a conversion efficiency of about 40%.

The realization of the cells, whether they are single junction or multiple, takes place by deposition of materials on a substrate of germanium. In the single-junction cells the substrate in Ge has solely the function of mechanical support and matrix for growth of monocrystalline active layers, while in the multijunction cells the substrate participates in the realization of the junction with the lowest energy gap.

Due to high price of Ge material, since twenty years there have been attempts to epitaxially integrate III-V compounds with Si substrates, this latter material being low-cost and easier to manufacture with respect to Ge [4.1, 4.2]. In particular, this has been the key idea of virtual substrates (VS). A thick, uniform buffer layer on a mismatched substrate can be called a virtual substrate. As an example, a thick epitaxial layer of Ge on a silicon substrate can serve as a virtual Ge substrate, even though conventional Ge substrates are not available in high quality at this time. If the Ge buffer layer is very thick, it will behave as a conventional Ge substrate in some respects.

An important goal has been the realization of silicon wafer with only a thin surface film of Ge, having a crystal structure and lattice parameter suitable for the subsequent chemical vapor deposition of GaAs and InGaP.

The realization of these VS, reducing the amount of germanium to be used, allows a reduction of costs and moreover the deposition process would give the possibility to realize substrates with specific intermediate lattice parameters that is not possible with other techniques.

Besides, the usage of Ge VS for the integration of high-efficient III-V concentrator solar cells, in the last few years, Ge VS have been employed into strain-engineered microelectronic devices (HFET, BiCMOS) in order to enhance the electrical transport properties of Si [4.3].

In this chapter, the aim is to evaluate the crystalline quality of a deposition of a Ge layer on a Si substrate, in order to realize virtual substrates with optimal characteristics to allow the subsequent deposition of GaAs or other semiconductor compounds with lattice parameter similar to that of Ge.

4.2. Heteroepitaxial deposition by LEPECVD

The basis for the realization of a Ge virtual substrate is represented by heteroepitaxy, which can be defined as the single-crystal growth of one semiconductor on another [4.4]. In particular it consists in deposition of a thin layer of crystalline material on a substrate massive, also crystalline, which directs the growth and determines the structural properties of the whole structure. The thickness of the heteroepitaxial layer can vary from the fraction of a nanometer to hundreds of microns.

At Sensor and semiconductor Laboratory (Ferrara, Italy) a crystalline Ge film can be grown on the surface of a Si crystal by using Low Energy Plasma Enhanced Chemical Vapour Deposition (LEPECVD) method. Fig. 4.1 shows an image of the LEPECVD reactor at SSL. LEPECVD is a deposition technique developed for the epitaxy of Si, Ge and SiGe alloys at very high deposition rates, up to 10 nm/sec, more than 10 times faster than other growth techniques [4.5, 4.6]. To enhance the growth rate while maintaining low substrate temperatures non thermal energy has to be provided for the dissociation of the reactive molecules: in LEPECVD this energy is furnished by a plasma. The plasma generates highly reactive radicals and energetic ions which strike the sample surface and cause a great enhancement of the hydrogen removal rate, which lead to an increased grow-rate. The arrival of energetic ions on the sample surface also cause an enhancement in the particles mobility, which is of great importance when epitaxial growth is performed at low thermal budgets.

The LEPECVD process at SSL is based on a inductively coupled radio-frequency (RF) excitation inside a quartz chamber embedded in the high vacuum reactor. This process is also known as radio frequency plasma enhanced chemical vapor deposition (RF-PECDV) and differs from other LEPECVD techniques because the substrate is not biased and ions are accelerated in every direction. In order to start the plasma reaction the growth chamber have to be filled in with H_2 (or another suitable gas) while precursor gases are added in a subsequent moment, when plasma is already presents in the chamber. The plasma source is positioned in the bottom part of the growth chamber and the samples have to be introduced in the reactor facing down, so to avoid dust to fall and accumulate on the active surface. A few centimeters above the wafer a graphite heater heat the sample at the selected temperature, which is measured with a thermocouple.

Precursor gases (SiH_4 and GeH_4) are introduced just below the sample and an additional H_2 flow is used to control the pressure inside the growth chamber and to drive precursor gases. With a

turbo molecular pump and a rotary prevacuum pump the chamber is pumped at a pressure of about 10^{-7} mbar, while during the deposition process the working pressure is typically in the range of 5×10^{-4} to 5×10^{-3} mbar.

A load lock prevent contamination of the growth chamber during wafer loading and promote desorption of water from the sample surface before the epitaxial growth. Moreover, a scroll prevacuum pump and a turbo molecular pump maintain the load lock at the same pressure of the growth chamber in order to avoid chamber contamination from external environment. Although ion-energies are low (less than 15 eV), the wafer is exposed to a very high intensity plasma, leading to epitaxial growth rates of several nm/s through the efficient decomposition of the precursor gases and an enhancement of the surface kinetics. The substrate is totally immersed in the plasma and it is heated from the backside by a resistance heater: operating temperatures are typically in the range of 400 to 600°C.

Figure 4.1: LEPECVD reactor in the clean room at SSL.

4.2.1. Mismatched heteroepitaxial growth and strain relaxation

This section is concerned with several important aspects of mismatched heteroepitaxial growth: mismatch, strain, lattice relaxation, the critical layer thickness, and the introduction of dislocation defects as well as few basic concepts on their dynamics.

In almost cases of interest, heteroepitaxial growth is rarely lattice-matched. Indeed, the difference between lattice constants of the substrate and the epitaxial layer, is a direct cause of mismatch between the materials. This latter can be defined as

$$m = \frac{a_L - a_s}{a_s} \qquad 4.1.$$

where a_S is the relaxed lattice constant of the substrate and a_L is the relaxed lattice constant of the epitaxial layer. The mismatch may take on either sign, i.e., $m > 0$ or $m < 0$, thus the systems where mismatch occurs being tensile or compressive respectively. The same quantity can be also defined perpendicularly (or out-of-plane)

$$m_{\perp} = \frac{a_L{}^{\perp} - a_s}{a_s} \qquad 4.2.$$

or parallel (in-plane) to the interface between the materials

$$m_{\parallel} = \frac{a_L{}^{\parallel} - a_s}{a_s} \qquad 4.3.$$

If the lattice mismatch between the epitaxial layer and substrate is small and if the growth mode is two-dimensional, i.e., layer-by-layer, the initial growth will be coherently strained to match the atomic spacings of the substrate in the plane of the interface. This situation is schematically depicted in Fig. 4.2a, where the epitaxial layer has a larger lattice constant than the substrate ($a_L > a_S$ and $f < 0$). The substrate is also assumed to not constrain the epitaxial layer in the growth direction and to be sufficiently thick with respect to the layer so that it can be considered unstrained by the growth of the epitaxial layer [4.4]. Hence, in heteroepitaxial systems with low mismatch, during the initial growth, a thin epitaxial layer takes on the relaxed lattice constant of the substrate within the growth plane and the growth is usually referred to as pseudomorphic. The pseudomorphic layer matches the substrate lattice constant in the plane of the interface ($a_L{}^{\parallel} = a_S$) and therefore experiences in-plane biaxial compression. The in-plane strain is defined as

$$\varepsilon_{\parallel} = \frac{a_L{}^{\parallel} - a_0}{a_0} = m - R \qquad 4.4.$$

where a_0 is the relaxed lattice constant of the layer at equilibrium condition and R represents the lattice relaxation. This latter is an important parameter that denotes the state of growth of the epitaxial layer with respect to the substrate and can be defined as

$$R = \frac{{a_L}^{\parallel} - a_S}{a_L - a_S} = \frac{m_{\parallel}}{m_{\perp}} \qquad 4.5.$$

It is worth noting that for a pseudomorphic layer, where no lattice relaxation has occurred, $R = 0$, thus $\varepsilon_{\parallel} = m$. On the other hand, the out-of-plane strain is given by

$$\varepsilon_{\perp} = \frac{{a_L}^{\perp} - a_0}{a_0} = -R_B \varepsilon_{\parallel} = -\frac{2C_{12}}{C_{11}} \varepsilon_{\parallel} \qquad 4.6.$$

where R_B is the biaxial relaxation constant relative to the growing epitaxial layer and C the elastic stiffness constants as tabulated in [4.4]. During the initial pseudomorphic growth, the unit cell of the epitaxial layer is tetragonally distorted with an out-of-plane lattice constant c being greater than a_L.

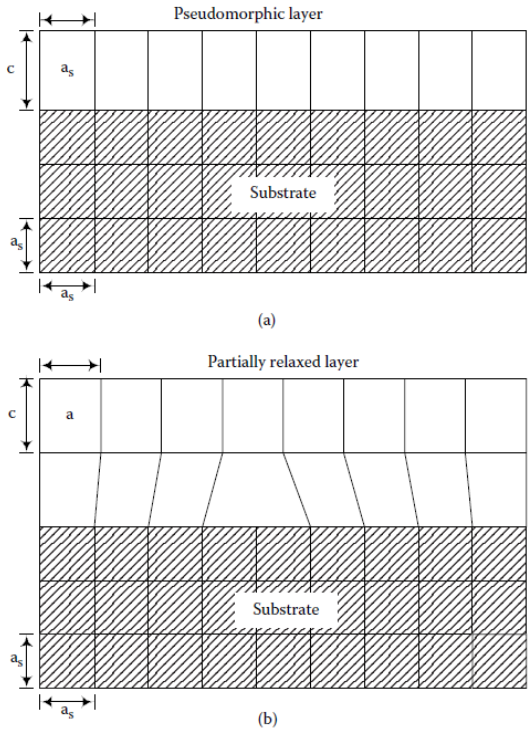

Figure 4.2: Growth of a heteroepitaxial layer on a mismatched substrate: (a) pseudomorphic layer; (b) partially relaxed layer [4.4].

According to the model given by Matthews and Blakeslee [4.7], as the epitaxial layer thickness increases, so does the strain energy which is stored in the layer. At a certain thickness, which is called *critical layer thickness*, the heteroepitaxial structure becomes energetically favorable for the introduction of *misfit dislocations* which relax some of the mismatch strain at the interface between the materials, thus acting as a plastic strain. Indeed, *misfit* dislocations form at (or near) the interface to relieve strain in a mismatched heteroepitaxial layer, once this latter exceeds the *critical layer thickness*. This new phase of growth is thus characterized by a partial or total relaxation of the in-plane lattice constant of the layer to its unstrained value. Associated with these *misfit dislocations* are *threading dislocations*, which run through the thickness of the heteroepitaxial layer. In fact, **threading dislocations** are typically present in bulk diamond and zinc blende crystals due to thermal or mechanical stresses which act on the crystal during growth or cooling. A heteroepitaxial layer grown on such a wafer will typically inherit the threading dislocations from the substrate, which then propagate through the heteroepitaxial layer to a free surface, gliding to create misfit dislocations at the interface. In this case, only if this relaxation mechanism is active, the epitaxial film must have a threading dislocation density equal to or less than that of the starting substrate. Indeed, the amount of lattice mismatch that may be relieved by this phenomenon depends on the substrate dislocation density and the average length for the misfit segments of the dislocations.

All these aspects contribute together to affect the properties of heteroepitaxial semiconductors in different ways: as an example, strain can change the band structure of a semiconductor or its energy gap, or it can also excites the motion of dislocations during the operation of laser devices, thus causing catastrophic failure. For solar cell applications, the presence of dislocations in the

material tends to degrade its electrical properties, affecting device performance and lifetime. The control of these defects is therefore of considerable interest and represents the aim of next section.

4.3. X-ray analysis applied to heteroepitaxial SiGe structures

The characterization of heteroepitaxial structures by high resolution X-ray diffractometer is a non-destructive technique that allows to reveal the structural properties of samples under analysis. In fact, application of this method requires an understanding of how the diffraction profile of the specimen relates to the crystal structure of the sample. From the rocking curve obtained through the HRXRD it is possible to determine the lattice constants (both parallel and perpendicular to the interface between layer and substrate) of the cubic cell of the heteroepitaxial layer, the density of dislocations present either in the layer or within the substrate and the thickness of the layer deposited. All these parameters are very important for the realization of virtual substrates and for their applications. Indeed, for multi-junction structures or for the integration of VSs within electronic devices, it is mandatory that the layer of Ge at the end of the deposition process features high crystalline quality and contains a low density of defects and that the obtained sample is not deformed neither structurally nor morphologically.

4.3.1. Strain

By considering Eqs. 1.45. and 1.47., in order to calculate out-of-plane and in-plane strains in a heteroepitaxial structure it is necessary to determine the lattice constant of the layer perpendicular and parallel to the interface between substrate and film. With this regard, it is usually appropriate to assume that the strain is constant as a function of depth. In this case, for a binary heteroepitaxial layer such as Ge (over Si substrate), the relaxed lattice constant is known so that there is only one independent unknown. Moreover, once the in-plane or out-of plane lattice constant is known, the other may be calculated. Another assumption is that the substrate, having Bragg angle θ_{BS}, can be considered unstrained, i.e., it is thick with respect to the layer.

If crystallographic planes of the film are parallel to the surface, symmetric rocking curves are normally used to obtain a diffraction profile of the sample under investigation. In particular, for a Ge film grown over a (001) Si substrate, the (004) are thus the planes used for symmetric diffraction.

The out-of-plane lattice constant of the epitaxial layer can be determined from the Bragg angle for the layer in the rocking curve. For a diamond heteroepitaxial layer, e.g., Ge film, using the (00m) reflection it results

$$a_{\perp} = md \tag{4.7.}$$

where $d = {}^{a}/_{\sqrt{h^2+k^2+m^2}}$ is the d_spacing of (00m) planes for the layer. From Bragg's law one obtains

$$a_{\perp} = \frac{m\lambda}{2\sin(\theta_{B00m,substrate} + \Delta\theta_{B00m})} \qquad 4.8.$$

where $\Delta\theta_{B00m}$ is the difference in 00m Bragg angles between the epitaxial film and the substrate, i.e., $\Delta\theta_{B00m} = \theta_{B00m,layer} - \theta_{B00m,substrate}$. It is worth noting that in real heteroepitaxial structures a crystallographic tilt between the normals to the surfaces of the epitaxial layer and the substrate may occur. Hence, in order to find the strain in the epitaxial film, it is necessary to measure rocking curves at two or more azimuths φ. As an example, if RCs are measured at azimuths φ =0° and φ =90°, then the angular separation between the epitaxial layer and substrate diffraction peaks turns out to be

$$\Delta\theta_{B00m} = \frac{\Delta\theta(\varphi = 0°) + \Delta\theta(\varphi = 90°)}{2} \qquad 4.9.$$

Finally, the out-of-plane strain can be simply obtained from Eq. 1.47, which also gives the in-plane strain under assumptions of biaxial stress and tetragonal distorsion.

An alternative way to measure the strain, both perpendicular and parallel to the interface, is to carry out an asymmetric RC, i.e., by recording diffracted intensity from planes which are not parallel to the surface. For the case of Ge (001) layer, one can use (224) crystallographic planes as sketched in Fig. 4.3. As can be seen, the distance between planes d_{hkl} is directly related to the in-plane lattice constant, thus allowing for an easy determination of all the strain parameters.

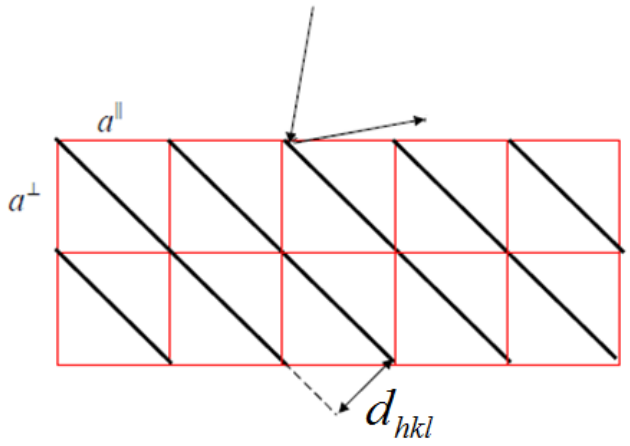

Figure 4.3: X-ray diffraction from planes which are not parallel to the surface, thus resulting in asymmetric RC.

4.3.2. Dislocation density

X-ray diffraction has been employed to determine the average dislocation density in the volume of heteroepitaxial binary SiGe samples. Indeed, as reported in [4.7], in single-crystal semiconductor specimens misfit and threading dislocations broaden the RC in two ways: (i) the dislocation introduces a rotation of the crystal lattice, thus directly broadening the FWHM of the RC (angular broadening); (ii) the dislocation is bounded by a strain field, in which the Bragg angle of the crystal is nonuniform (strain broadening).

The experimental X-ray rocking curve is assumed to be Gaussian in shape, with FWHM $\beta_m(hkl)$, and to represent the convolution of a number of Gaussian intensity distributions. Hence, results from the convolution of Gaussian intensity functions lead to

$$\beta^2{}_m(hkl) = \beta^2{}_0(hkl) + \beta^2{}_d(hkl) + \beta^2{}_\alpha(hkl) + \beta^2{}_\varepsilon(hkl) + \beta^2{}_L(hkl) + \beta^2{}_R(hkl) \quad 4.10.$$

where $\beta_0(hkl)$ represents the Darwin width for the heteroepitaxial sample under analysis, $\beta_d(hkl)$ is the instrumental broadening, $\beta_\alpha(hkl)$ is the broadening due to angular rotation at dislocations, $\beta_\varepsilon(hkl)$ being the width due to strain which surrounds dislocations, $\beta_L(hkl)$ the broadening due to crystal thickness and $\beta_R(hkl)$ the spread due to curvature of the specimen. According to Ref. [4.7], if the effects of the crystal size broadening and curvature can be considered negligible, then the broadening contribution due to dislocations $\beta^2{}_{disl}(hkl)$ can be found from the following formula

$$\beta^2{}_{disl}(hkl) = \beta^2{}_m(hkl) - \beta^2{}_d(hkl) = \beta^2{}_\alpha(hkl) + \beta^2{}_\varepsilon(hkl) = K_\alpha + K_\varepsilon \tan^2\theta_B \quad 4.11.$$

where ${\beta^2}_{\alpha}(hkl) \approx (2\pi\, ln\, 2)b^2D = K_\alpha$, b being the length of the Burger vector [4.4] and D the dislocation density. The strain broadening due to dislocations has been modeled by Warren, Hordon and Averbach as ${\beta^2}_{\varepsilon}(hkl) = (8\, ln\, 2)\overline{\varepsilon_N^2}\, tan^2\, \theta_B$, where $\overline{\varepsilon_N^2}$ represents the mean square strain in the direction of the normal to the diffracting planes.

Hence, in order to calculate dislocation density of SiGe heteroepitaxial samples, the FWHM $\beta_m(hkl)$ of the RC has been measured for a number of hkl reflections and the extracted value ${\beta^2}_{disl}(hkl)$ has been plotted as a function of $\tan^2 \theta_B$. Then, the values of K_α and K_ε represent the intercept and slope of the obtained function, respectively. Finally, the dislocation density can be simply found by using the following equation

$$D = \frac{K_\alpha}{4.36b^2} \qquad 4.12.$$

It should be highlighted that the measurement of as few as three rocking curves allows accurate determination of dislocation density. For most (001) semiconductor crystals, e.g., SiGe heteroepitaxial samples, since the (004) RC width is mostly related to the angular broadening of dislocations while the (113) width is primarily determined by the strain broadening, then it is sufficient to measure the (004), (113) and (115) RCs for the application of this approach. Fig. 4.4 shows an example of the application of this method.

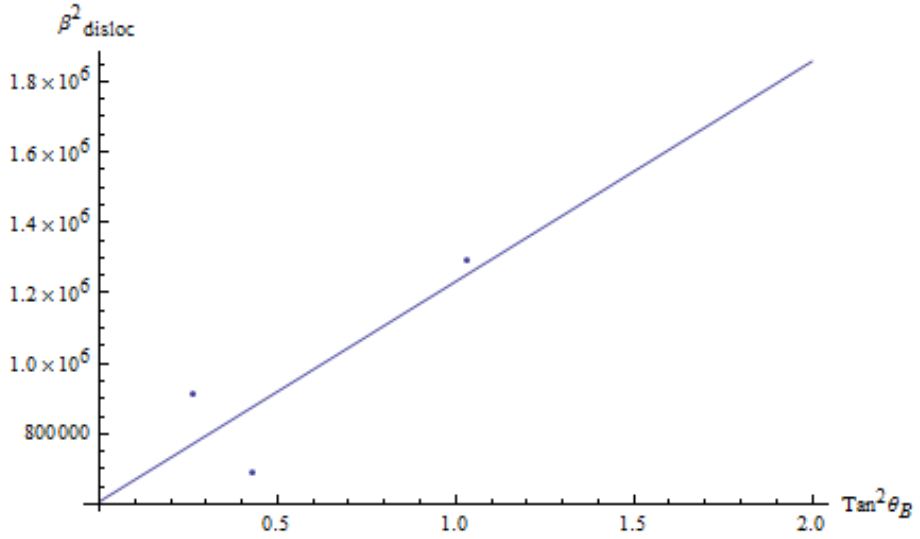

Figure 4.4: ${\beta^2}_{disl}(hkl)$ vs. $\tan^2 \theta_B$ for a 1.5-μm thick layer of Ge over Si (100), grown by LEPECVD technique. ${\beta^2}_{disl}(hkl)$ is the square of the dislocation broadening, extracted from measured rocking curve widths for various *hkl* reflections. $\theta_B$is the Bragg angle. The filled circles represent the data extracted from measurements, and the line is the least squares fit.

4.4. Data analysis

The deposition of Ge films of variable thickness was performed on wafers of Si (100), 400 µm thick and tilted of 6° towards [111] direction. The growth parameters of Ge films are shown in Table 1.

Table 1: Experimental parameters of growth of Ge films

Precursor gas	GeH_4
Temperature on wafer	600°
Deposition pressure	10^{-3} mbar
Flux of the precursor gas	50 sccm
Flux of the activation gas (H_2)	50 sccm
Power of the plasma source	1600 W
Ion energy	15 eV

X-ray characterization of the heteroepitaxial samples was carried out by using the high-resolution X-ray diffractometer available at SSL. Here, experimental results are shown for samples coded 130, 132 and 166, respectively. All the samples have been analyzed by measuring RCs and calculating the parameters of strain, mismatch, relaxation and density of dislocations. In particular, for the analysis of strain, mismatch and relaxation, symmetric RCs have been performed by X-ray diffraction of (400) planes at two azimuths φ. On the other hand, for calculation of dislocation density the method described in previous section has been followed. Thus, asymmetric RCs have been carried out by diffraction of (113) and (115) planes of the SiGe samples.

It is worth noting that in order to assess the crystalline quality of all the samples, the open detector mode of the diffractometer has been used for the analysis, because this is the configuration which allows to obtain a FWHM of the RC that depends on all the contributions of lattice defects.

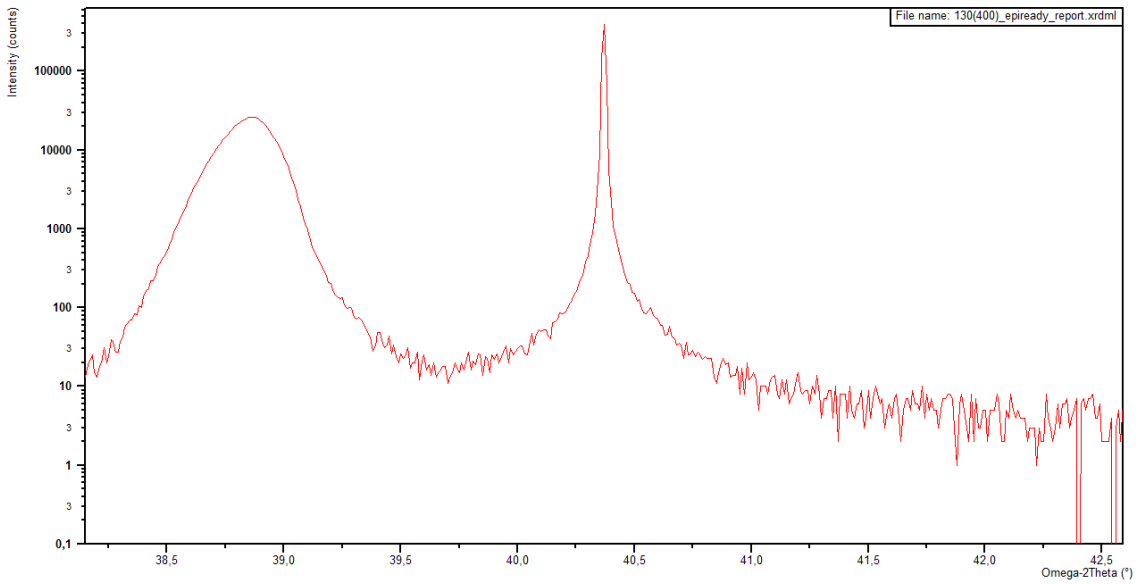

Figure 4.5: Rocking curve of sample SiGe 130 obtained with the beam incident onto (400)crystallographic planes, in open-detector mode and at azimuth φ =0°. The The FWHM of Gaussian distribution for Ge layer was 831 arcsec.

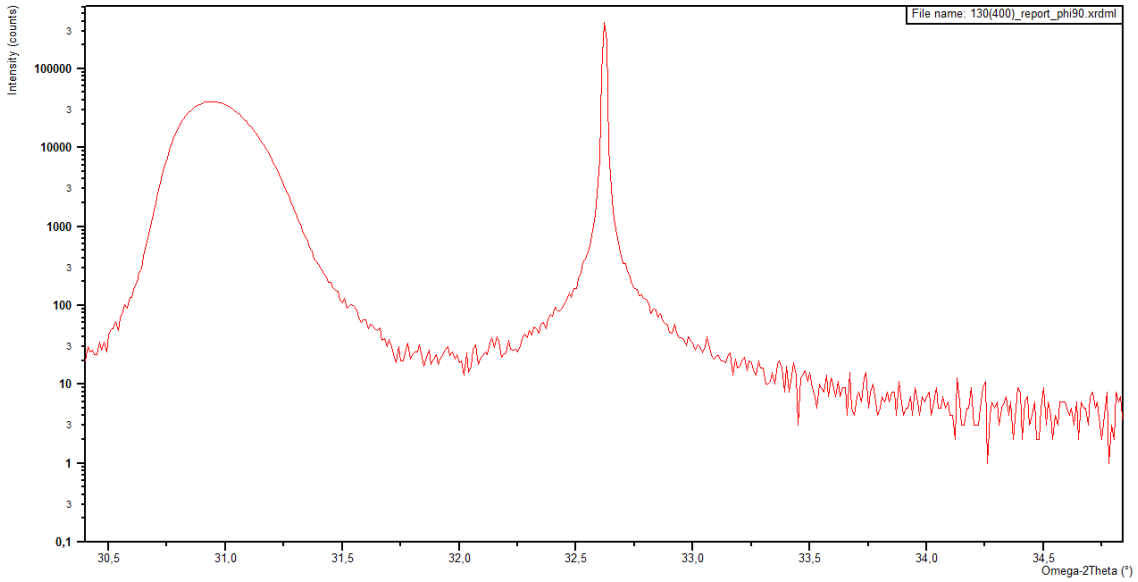

Figure 4.6: Rocking curve of sample SiGe 130 obtained with the beam incident onto (400) crystallographic planes, in open-detector mode and at azimuth φ =90°.

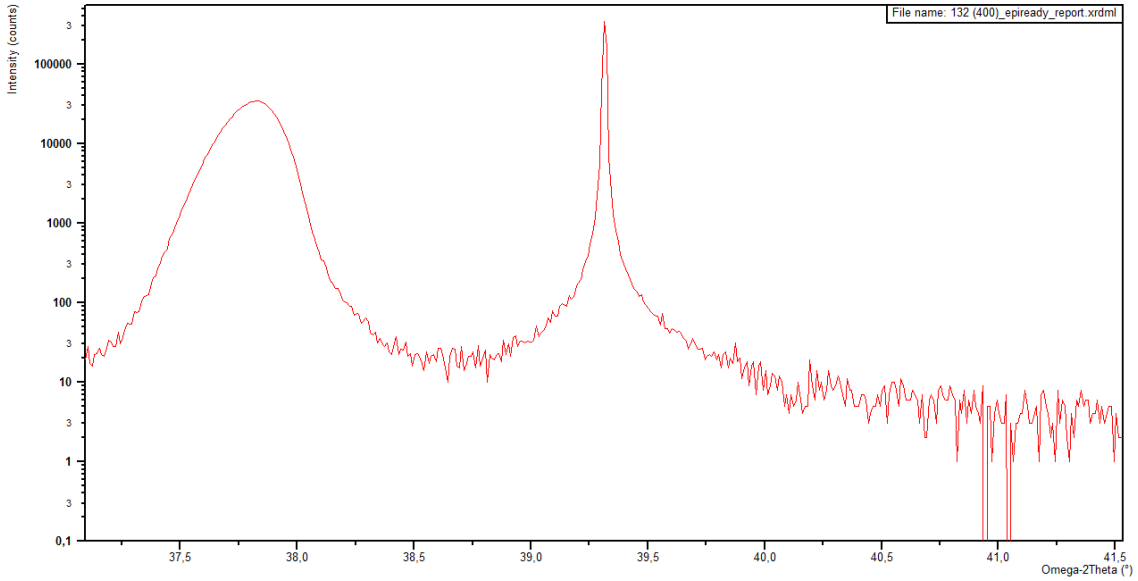

Figure 4.7: Rocking curve of sample SiGe 132 obtained with the beam incident onto (400) crystallographic planes, in open-detector mode and at azimuth φ =0°. The The FWHM of Gaussian distribution for Ge layer was 861 arcsec.

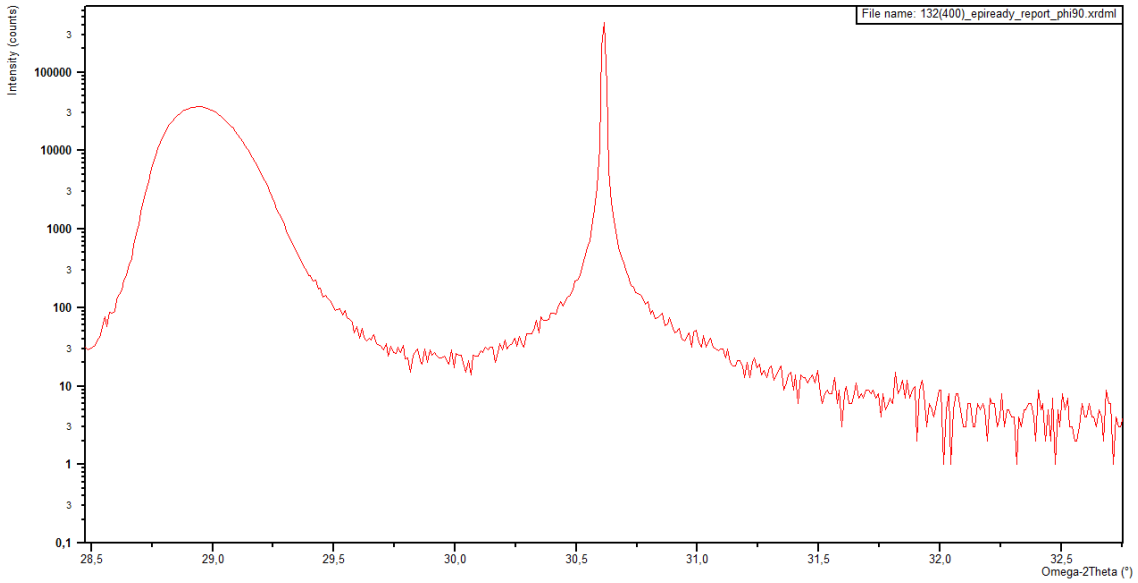

Figure 4.8: Rocking curve of sample SiGe 132 obtained with the beam incident onto (400) crystallographic planes, in open-detector mode and at azimuth φ =90°.

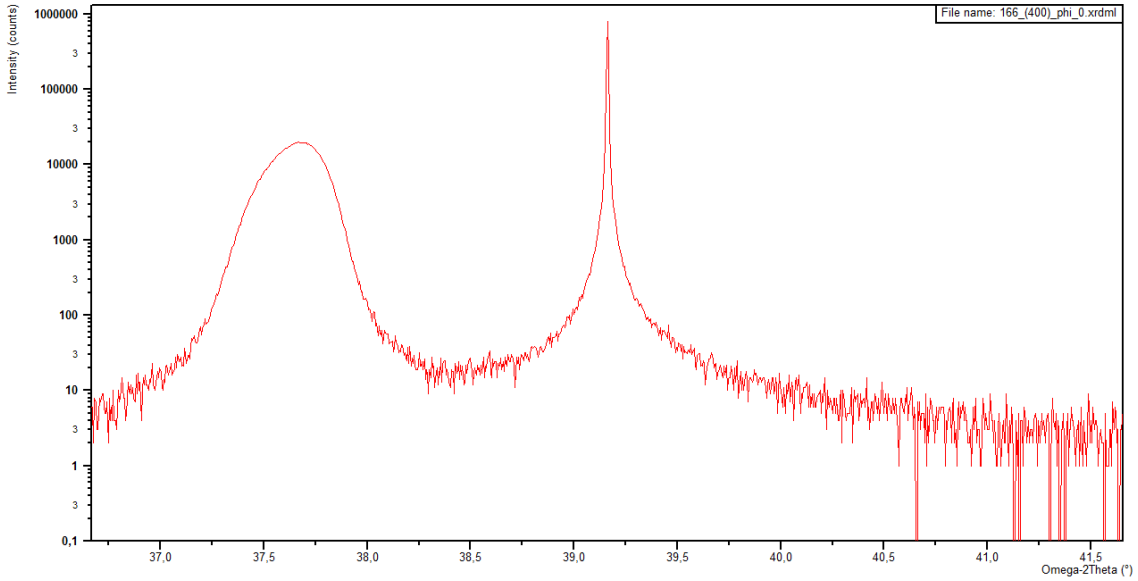

Figure 4.9: Rocking curve of sample SiGe 166 obtained with the beam incident onto (400) crystallographic planes, in open-detector mode and at azimuth φ=0°. The FWHM of Gaussian distribution for Ge layer was 965 arcsec.

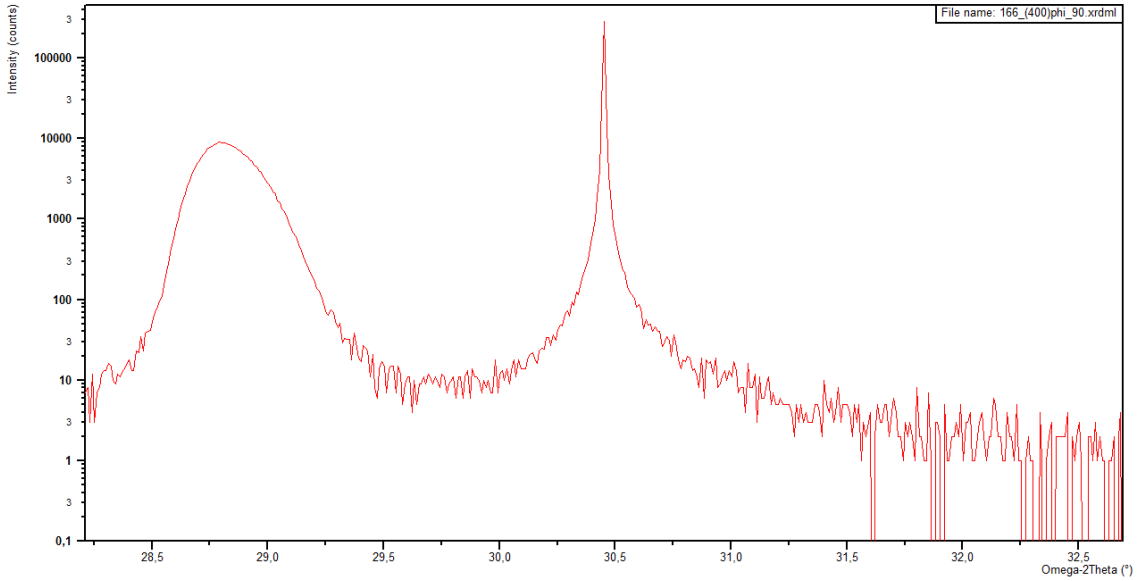

Figure 4.10: Rocking curve of sample SiGe 166 obtained with the beam incident onto (400) crystallographic planes, in open-detector mode and at azimuth φ=90°.

All RCs of the samples exhibited a well-defined Gaussian profile for both Si substrate and Ge film. This highlights that the layer of Ge grown by LEPECVD was structurally crystalline and not amorphous, this fact being important for realization of virtual substrates where a thick crystalline Ge film is needed. The FWHM of the two Gaussian distributions showed a considerable enlargement at the peak of Ge compared to that of Si. Since this broadening is mainly determined by the contribution of dislocations, this evidence means that dislocations slightly deformed the crystallographic planes of the substrate but significantly perturbed the planes in Ge film for all the samples.

From the positions of the diffraction peaks in the symmetric RCs it was possible to determine the lattice constants of the layer cubic cell and consequently the mismatch, strain and degree of relaxation of the layer with respect to the substrate.

On the other hand, the FWHM of diffraction RCs allowed to reveal the density of threading dislocations present in the SiGe samples. The main characteristics of each measured sample are summarized in Table 2. In Figs. 4.11 and 4.12 experimental results of asymmetric RCs for calculation of dislocation density are shown for sample 130.

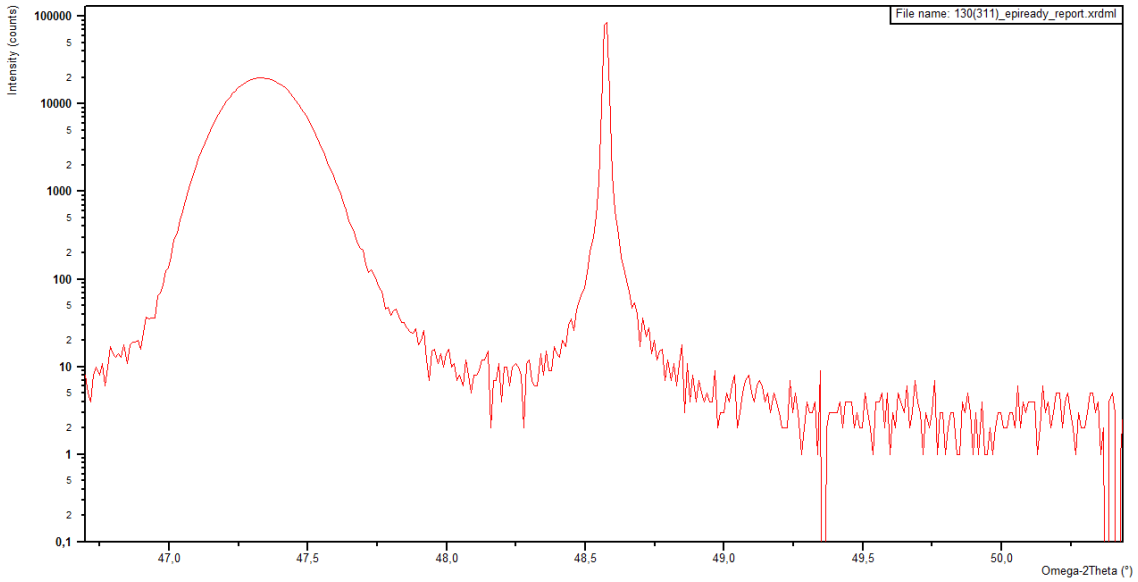

Figure 4.11: Rocking curve of sample SiGe 130 obtained with the beam incident onto (113) crystallographic planes, in open-detector mode. The FWHM of Gaussian distribution for Ge layer was 831 arcsec.

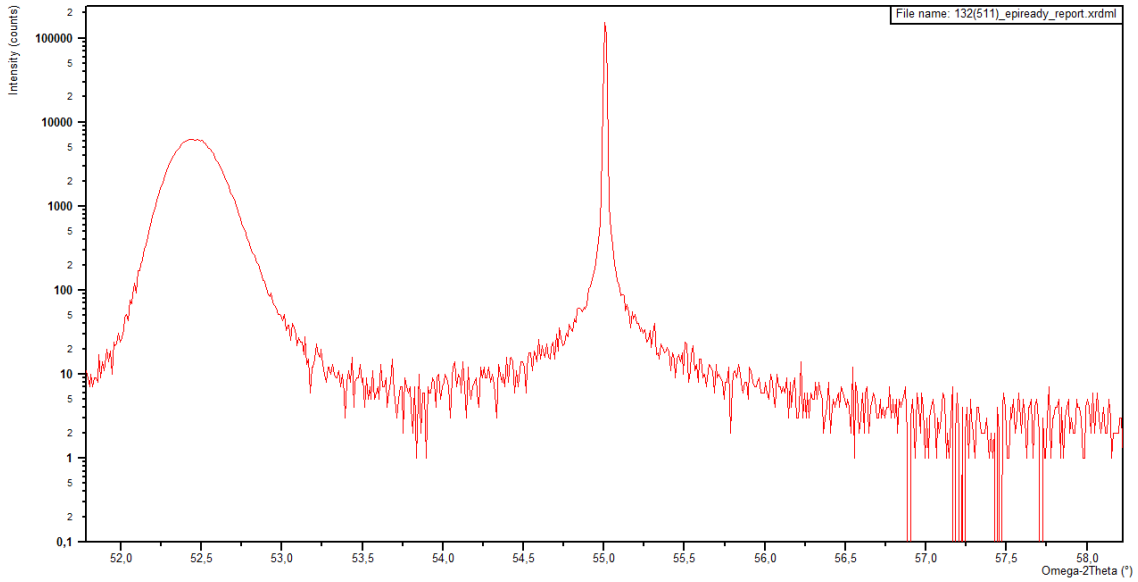

Figure 4.12: Rocking curve of sample SiGe 130 obtained with the beam incident onto (115)crystallographic planes, in open-detector mode. The FWHM of Gaussian distribution for Ge layer was 870 arcsec.

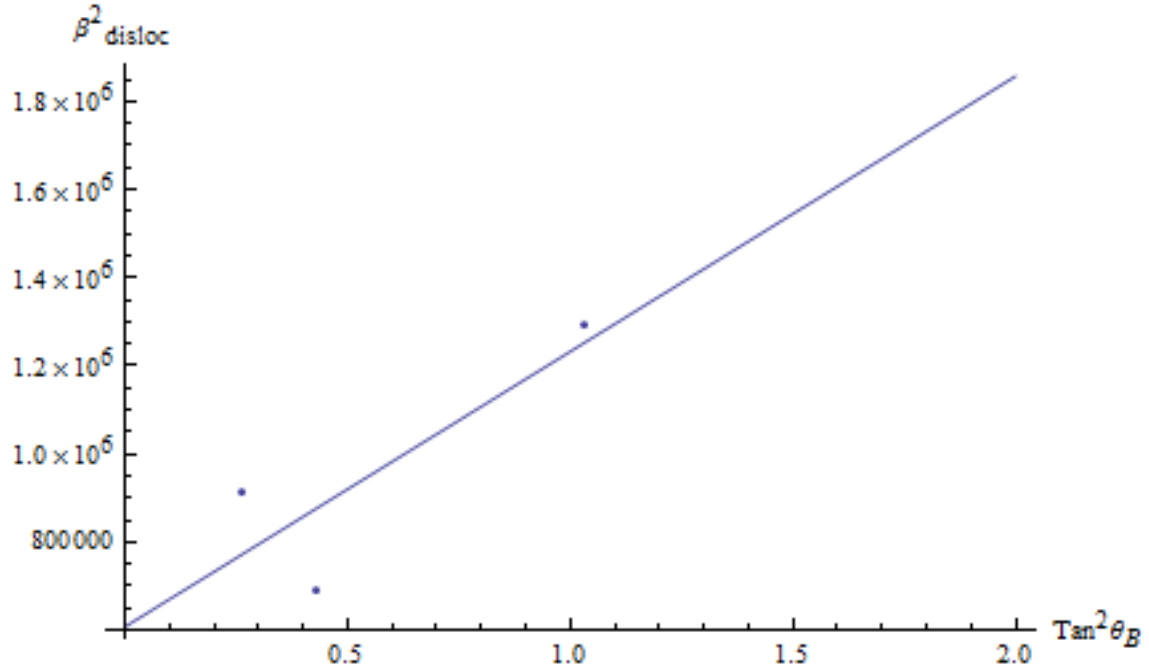

Figure 4.13: $\beta^2_{disl}(hkl)$ vs. $\tan^2\theta_B$ for sample 130. $\beta^2_{disl}(hkl)$ is the square of the dislocation broadening, extracted from measured rocking curve widths for various *hkl* reflections. θ_B is the Bragg angle. The filled circles represent the data extracted from measurements, and the line is the least squares fit.

Table 2: Main features of all samples under analysis

Sample	FWHM Ge-layer (arcsec)	$a^{\perp}_L$ (Å)	$a^{\parallel}_L$ (Å)	$\varepsilon_{\perp}$ (%)	$\varepsilon_{\parallel}$ (%)	$m_{\perp}$ (%)	$m_{\parallel}$ (%)	R (%)	Dislocation density D (10^9 cm^{-2})
130 (Ge-1.5 µm)	831	5.69	5.60	0.65	-0.98	4.85	3.14	75	2.0
132 (Ge-1.5 µm)	861	5.69	5.60	0.64	-0.97	4.84	3.16	75	1.8
166 (Ge-0.7 µm)	965	5.64	5.60	0.61	-0.92	4.81	3.21	77	2.8

As can be seen, all the samples show a partial degree of relaxation of the Ge layer parallel to the interface with the Si substrate. Indeed, the lattice constant of the cubic cell of the layer is greater than that of the substrate (5.43 Å for Si) but still lower than the lattice constant at balance condition or complete relaxation (5.65 Å). This means that the critical thickness of the deposited Ge film has been exceeded and consequently misfit dislocations (plastic deformation) occurred to relieve the deformation due to the epitaxial constraint, though part of the mismatch has been balanced by elastic deformation (relaxation is partial and not total).

Since the conditions of growth are similar for the samples 130 and 132, the obtained results are nearly equal. In particular, the epitaxial layer of Ge is tetragonally distorted with a lattice constant perpendicular to the interface that is greater than that at its state of equilibrium. However, this is not true for the sample 166, for which the film thickness is lower, thus the cubic cell of the layer was probably not properly formed.

Finally, the dislocation density for the layer of Ge is of the order of $10^9/cm^2$ for all the samples. Since this parameter decreases as the distance from the interface between Si and Ge increases, and also the weighting of diffracted intensity from different parts of the crystal will be such that the FWHM of the RC is indicative of the lowest dislocation density inside the crystal, it is assumed that the obtained value corresponds to that of the surface. This is a very important fact for the realization of multi-junction cells on SiGe structures, because it is the surface to play a decisive role in terms of dislocation density.

For the case of a 3-µm thick layer of GaAs, whose chemical properties are similar to those of Ge, grown by Metalorganic Vapor Phase Epitaxy (MOVPE) on a Si substrate, the dislocation density is of the order of $10^8/cm^2$. Indeed, if the deposition thickness increases, defects tend to remain confined at the interface, thus leading to a lower dislocation density.

4.5. References

[4.1] L. Renrong et al., *Tsinghua Science and Technology*, **14** (2009)
[4.2] D. J. Paul et al., *Thin Solid Film*, accepted for publication
[4.3] U. Konig et al., *Solid State Electronics*, **43**, 1383–1388 (1999)
[4.4] J. E. Ayers, *Heteroepitaxy of semiconductors: Theory, Growth and Characterization*, CRC Press (2007)
[4.5] C. Rosenblad et al., *Thin Solid Films* **336**, 89-91 (1998)
[4.6] H. L. Seng et al., *Nucl. Instrum. B* **215**, 235–239 (2004)
[4.7] J.W. Matthews and A.E. Blakeslee, *J. Cryst. Growth*, **27**, 118 (1974)

Appendix: X-ray characterization of ceramic coatings

Ceramic coatings and their applications

Ceramic and cermet (a composite material composed of ceramic and metal) materials are widely used in industrial applications that require high resistance to friction and wear, thanks to their high hardness and resistance to oxidation at high temperatures and their properties of thermal barrier [1.1]. Nevertheless, the high cost of production and their fragility limit the application of bulk ceramics. Hence, these kinds of materials are most frequently used in form of coatings that are applied onto less expensive materials, e.g., steels.

Ceramic coatings are widely used to protect soft materials from wear and corrosion even at high temperatures; due to their resistant and inert properties the main industries that apply this technology are chemical, naval and oil industries [1.2]. As an example, ceramic or cermet are currently used as thermal protection of gas turbines for civil, military and marine. They are usually deposited on "hot" parts of turbine liners or nozzles allowing to raise the operation temperature and, consequently, the efficiency of the machine. The required properties of these coatings are high resistance to corrosion, oxidation and erosion, good stability, and interfacial adhesion to the metal substrate [1.3].

For realization of wear resistant coatings, thermal spraying is often considered a valid alternative as compared to traditional coating techniques [1.4]. The most commonly methods used in thermal spraying are the APS (Air Plasma Spray) and HVOF (High Velocity Oxygen Fuel), as they allow obtaining high-quality anti-wear coatings. As an example, the APS is still the most widely used technique for the production of ceramic such as Al2O3: easiness of use, popularity of technology and lower manufacturing costs are the main advantages of such a technique. However, a factor which limits positive assessment of this method is a high level of porosity of coatings and low adhesion of the layer to base material. These features result both from the specific nature of plasma spraying and properties of used powders [1.5, 1.6].

The HVOF was developed to overcome the limitations of plasma spraying. Indeed, the higher speed deposition and lower spray flame temperature allows to create coatings with low porosity, limited oxidation of fused particles and low decomposition particle [1.1]. However, the HVOF has some limitations mainly related to the cost and difficulty of preparation of the starting powders and the lack of commercial availability of torches used for the deposition on the substrate.

APS coatings are more porous and fragile than HVOF sprayed cermet, mainly due to the lower speed of impact of particles. Nevertheless, the APS coatings have very high hardness and low susceptibility to corrosion in many environments and can resist high temperatures. A precise evaluation of the wear mechanisms that occur in APS and / or HVOF coatings can enable their

correct use in many applications, even when the environmental conditions of humidity are critical to the proper functioning of the tribological system [1.7].

In general, the formation of the coating consists in using powder particles of various size, including nanometric size, which are melted in a torch, ejected and projected at temperature and velocity variables in form of droplets on the substrate to be coated. Compared with bulk materials, the presence of porosity, oxide inclusions and any other phases or partially molten particles that may form during the deposition, may reduce the tribological performance of the coating. In addition, the low adhesion coating-substrate that characterizes the obtained coatings by thermal spraying, severely limits technological applications.

For these reasons, in recent years intensive research has been aimed at assessing the influence of such typical defects on the performance and quality of these types of coatings. This work reports on a microstructural investigation of three types of coatings obtained by X-ray diffraction (XRD) at Sensor and Semiconductor Laboratory (SSL, Ferrara, Italy) in order to identify the phases present in coatings. The research work has been done in collaboration with the group of Prof. Gianluca Garagnani at the Engineering Department and with Prof. Carmela Vaccaro at Geology Department. The analysis has been carried out on the entire surface of the samples creating a matrix array of 49 points (7×7). All samples were fabricated by a company specialized in industrial applications of ceramic and cermet coatings. The deposition parameters are therefore confidential.

Al_2O_3-13TiO_2

One of the main properties of Al_2O_3-13TiO_2 applied with APS, is the wear resistance. Its tribological behavior is currently under investigation by the scientific community [1.6, 1.8, 1.9]. Main factors that are correlated with the wear process are hardness, porosity and toughness. In fact, microhardness and toughness values of Al_2O_3 coating can be modified by varying its composition with addition of TiO_2 in plasma spraying in such a way that this can contribute to increase the toughness and wear resistance values of the coating. Indeed, Al_2O_3 with addition of TiO_2 significantly lower the microhardness of the alumina coating, while a decrease in hardness values result in an increase in toughness values of the alumina coatings [1.10].

Many models try to explain the behavior of evolution in the microstructure. Actually, it is considered that the phase transformation occurs from α (stable) to γ (metastable) Al_2O_3-13TiO_2 and that TiO_2 is in solution in γ phase, after APS process [1.11].

The studied coating, coded as C2, is Al_2O_3-13TiO_2, applied with APS technique onto a steel substrate (75 mm in diameter and 6 mm-thick), and the size particle of the powders being around -45÷15 μm.

WC-12Co

As highlighted in Ref. [1.12], WC–Co hardmetals are well established as materials highly resistant to wear in a wide variety of situations. Main parameters influencing their properties are carbide grain size and volume fraction. Sintered nanostructured WC–Co hardmetals, i.e. materials which have nanoscale tungsten carbide grains in a cobalt matrix, have been reported to exhibit enhanced performance in both sliding and abrasive wear [1.13-1.16]. They also benefit from

substantially higher hardness than those which have carbide grain sizes around the micron size [1.13, 1.16]. Indeed, the wear resistance of sintered WC–Co hardmetals has been shown to increase dramatically as the carbide grain size is reduced [1.13, 1.17].

Thermally sprayed WC–Co coatings, of the order of 200–400 μm thick, are widely used in many industries as they offer an effective and economic method of conferring wear resistance without compromising other attributes of the component. High velocity oxy-fuel (HVOF) thermal spraying has shown itself to be one of the better methods for depositing conventional WC–Co feedstock powders [1.18-1.20] because the higher velocities and lower temperatures experienced by the powder particles, as compared to plasma based routes (e.g., APS), result in less decomposition of the WC during spraying [1.21] along with lower levels of porosity, and thus higher wear resistance.

WC-12Co coatings applied by APS and HVOF techniques have been studied in order to understand the heterogeneity in the microstructure. Two coatings have been applied on steel plates, the size particle of the powders varying depending on application technique, between 88÷44 μm to -45÷15 μm, respectively. The X-ray analysis shows that the coatings present zones with different crystal concentration.

XRD patterns for Al_2O_3-13TiO_2

In Fig. 1.1 the diffraction patterns obtained by XRD analysis show presence of both main polymorphic modifications of Al_2O_3, i.e., both α and γ. A dominating phase in this case is γ-Al_2O_3modification. Reflexes from thermodynamically stable α- Al_2O_3 modification are distinctly weaker. In fact, a partial transformation of the α- Al_2O_3 to γ- Al_2O_3phase owing to the APS process occurred. The powders used for this kind of process usually have an α phase but the alumina is a polymorphic material and high temperatures accomodate phase transformation. The transformation from α→γ Al_2O_3 is due to the fact that nucleation energy of γ- Al_2O_3 is lower than that of α-Al2O3. Indeed, one should consider here thermodynamic aspects of the process and that each arrangement tends to reach a state with corresponding possibly lowest level of free energy, regardless of the fact if this state will be connected with creation of a metastable or thermodynamically stable modification.

Presence of α- Al_2O_3 form in the sprayed layer can be explained by uncompleted remelting of particles during its spread on base material. An important feature is that as hardness of α-Al2O3 is higher than that of γ- Al_2O_3 it is possible that, by a partial transformation of this phase, wear resistance can increase when compared with coatings which present a full transformation.

The peaks relative to γ- Al_2O_3 phase exhibit high intensity and they are wider than those associated to α- Al_2O_3 phase, this being probably due to a smaller crystal size of the γ- phase as compared to the α one.

TiO_2 does not appear in crystalline form in the diffraction pattern. Indeed, transformation in the amorphous state containing crystalline particles of Al_2O_3 is probably due to the lower melting point of TiO_2 and high cooling rate of the APS process.

Moreover, the X-ray diffraction pattern highlights a result of reaction between powder oxides, i.e., Al_2TiO_5. Indeed, aluminum titanate forms by the additive reaction between alumina and titania at temperatures above 1280 ºC [1.22]. However, the creation of this phase has a negative effect in the hardness and toughness of the sample [1.23].

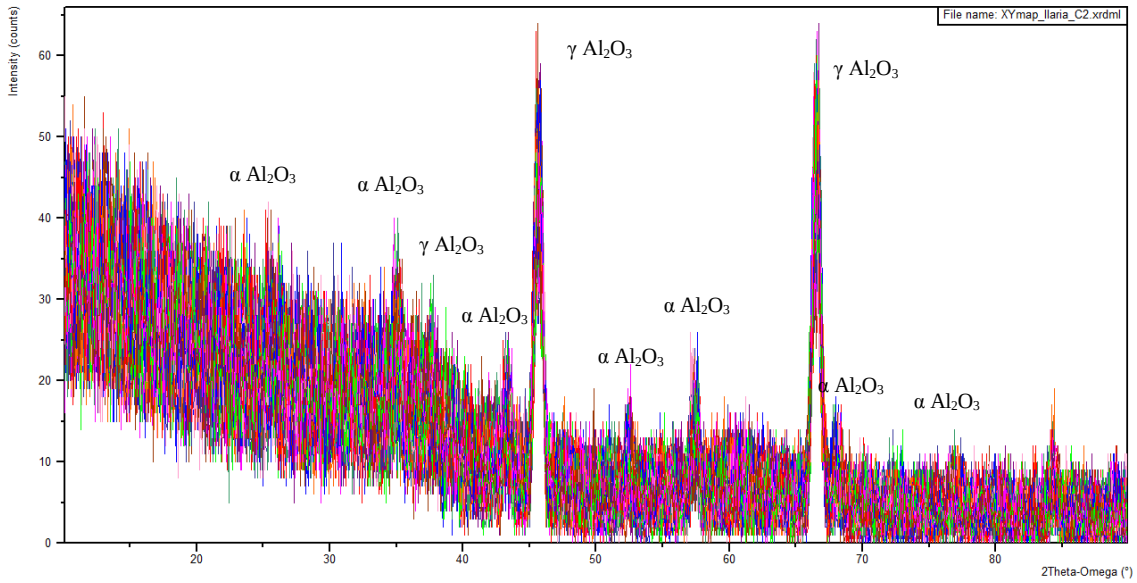

Figure 1.1: X-ray diffraction analysis of sample C2

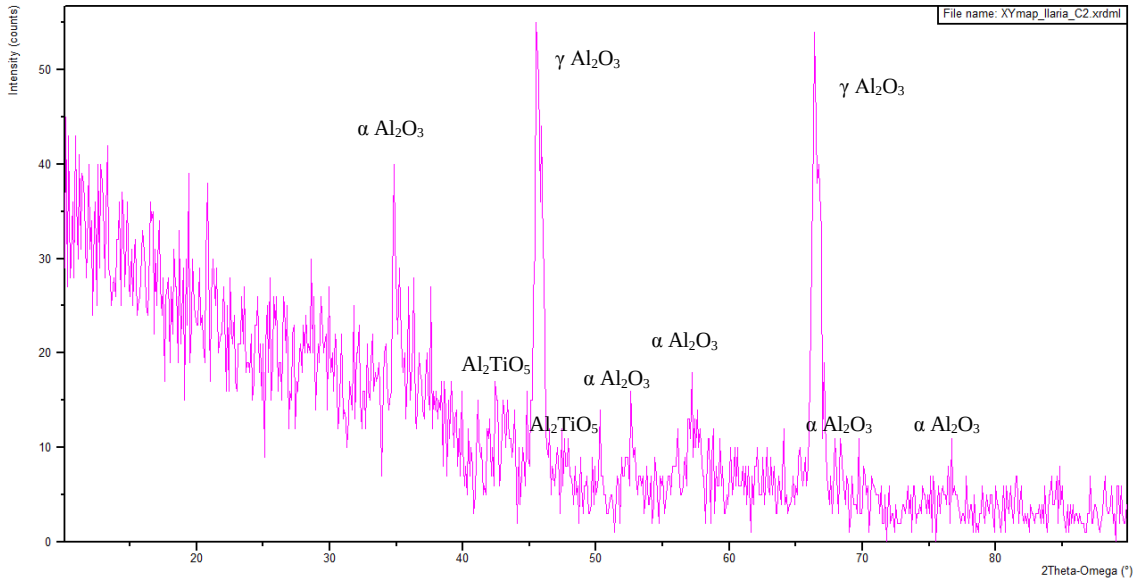

Figure 1.2: Punctual X-ray analysis of sample C2

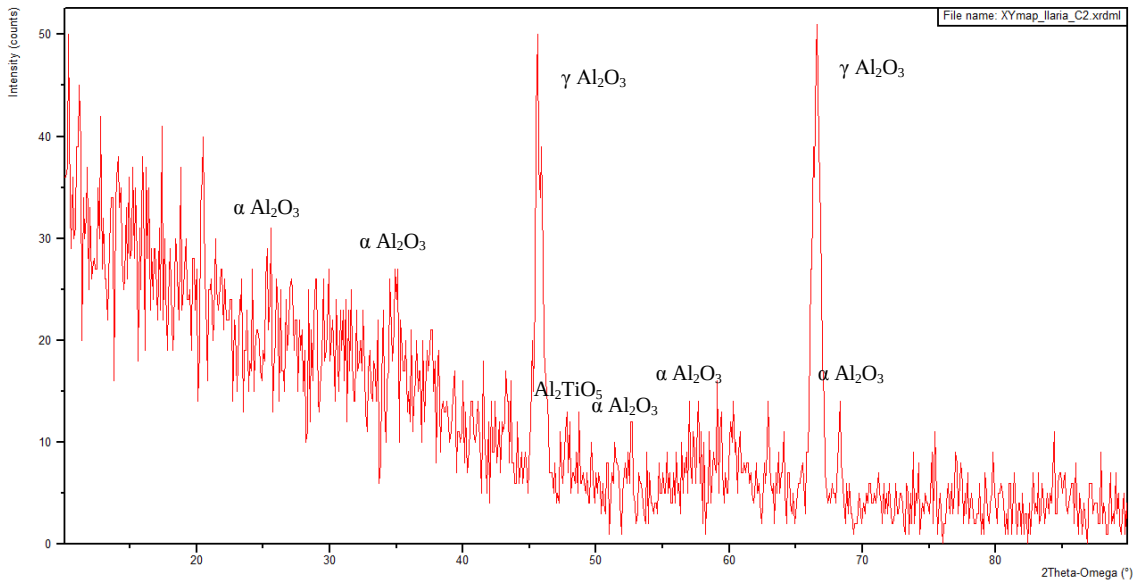

Figure 1.3: Punctual X-ray analysis of sample C2

XRD patterns for WC-12Co

The XRD mapping of the WC-12Co coatings, coded as C4 and C5 and obtained through APS and HVOF techniques respectively, are shown in Figs. 1.4 and 1.7 and clearly show the presence of WC peaks and prominent peaks of W2C. Results of X-ray characterization at fixed positions on the surface of the samples are highlighted in Figs. 1.5 and 1.6, and in Figs. 1.8 and 1.9, for C4 and C5 respectively.

For both samples, the analysis presents decomposition due to decarburization of the WC-12Co. As can be noticed, the decarburization is significantly higher in the APS coating than in the coating obtained by HVOF and this fact is ascribed to the higher temperature used in the APS process.

The intensity in peaks is lower for APS than for HVOF process. Indeed, according to Ref. [1.24], the higher the amount of transformation, the lower the index of crystallinity. A decrease in the intensity of the peaks of WC indicates a decrease in the volume fraction of the primary carbide. As a consequence, in the APS process a higher decomposition of WC occurs.

On the other hand, the higher intensity in HVOF method shows more order in the distribution of phases in the coating, less transformation and higher crystal content.

The XRD patterns for sample C4 show a lower intensity in all cases, as expected. In other cases, the presence of W2C and the differences in microstructure are considerable, while for sample C5 the analysis shows less dispersion in intensity and broadening.

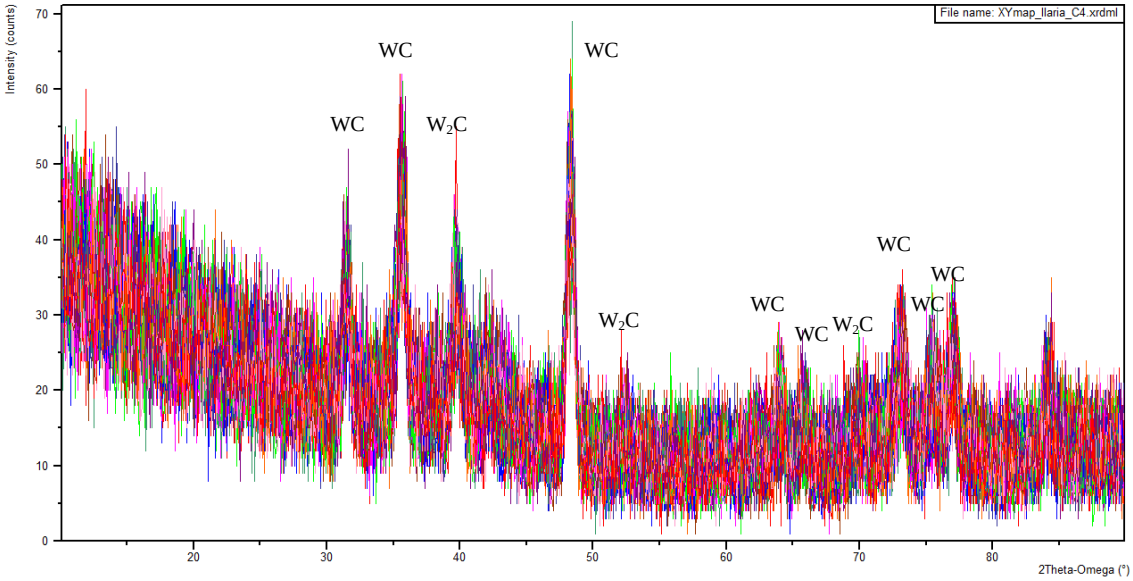

Figure 1.4: X-ray diffraction analysis of sample C4

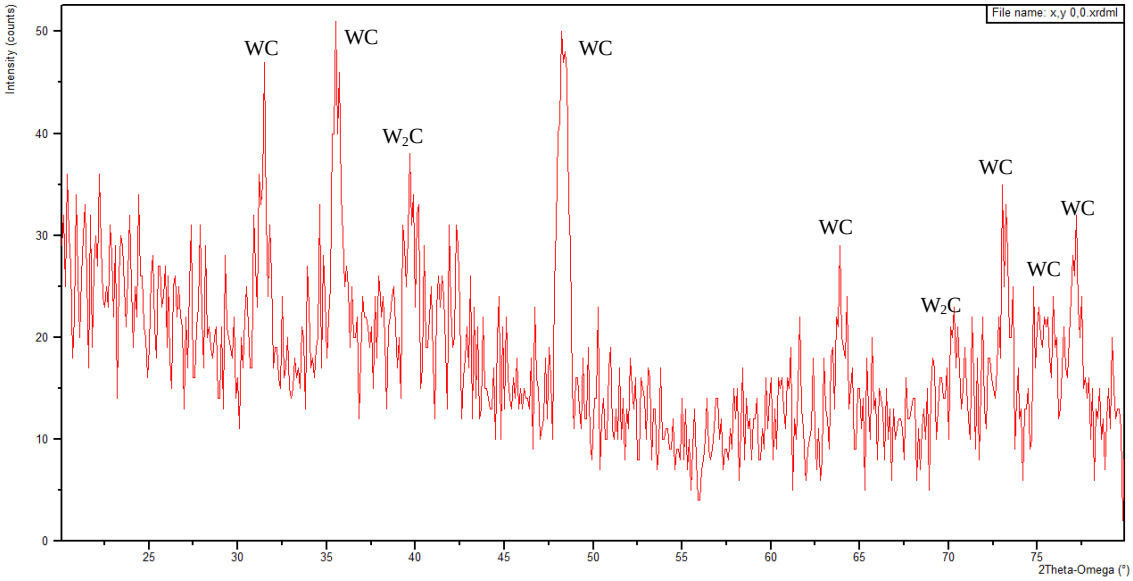

Figure 1.5: Punctual X-ray analysis of sample C4

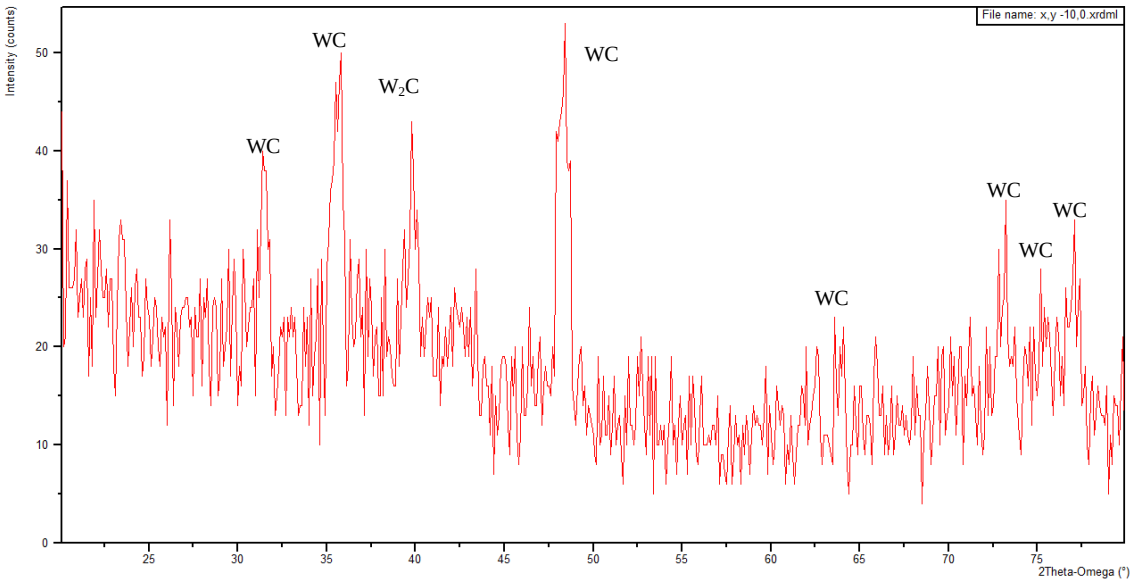

Figure 1.6: Punctual X-ray analysis of sample C4

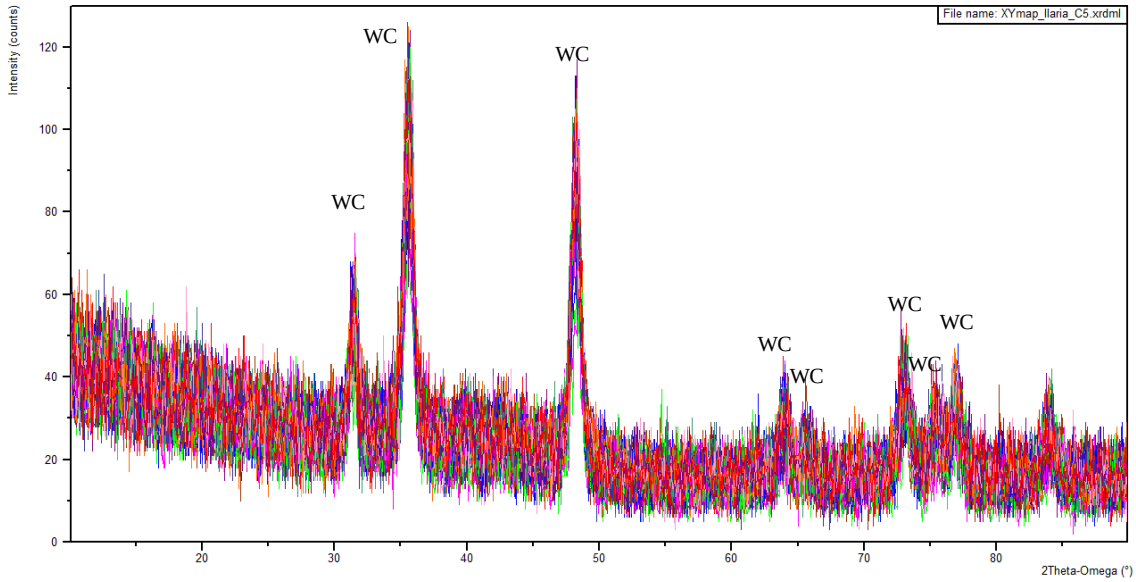

Figure 1.7: X-ray diffraction analysis of sample C5

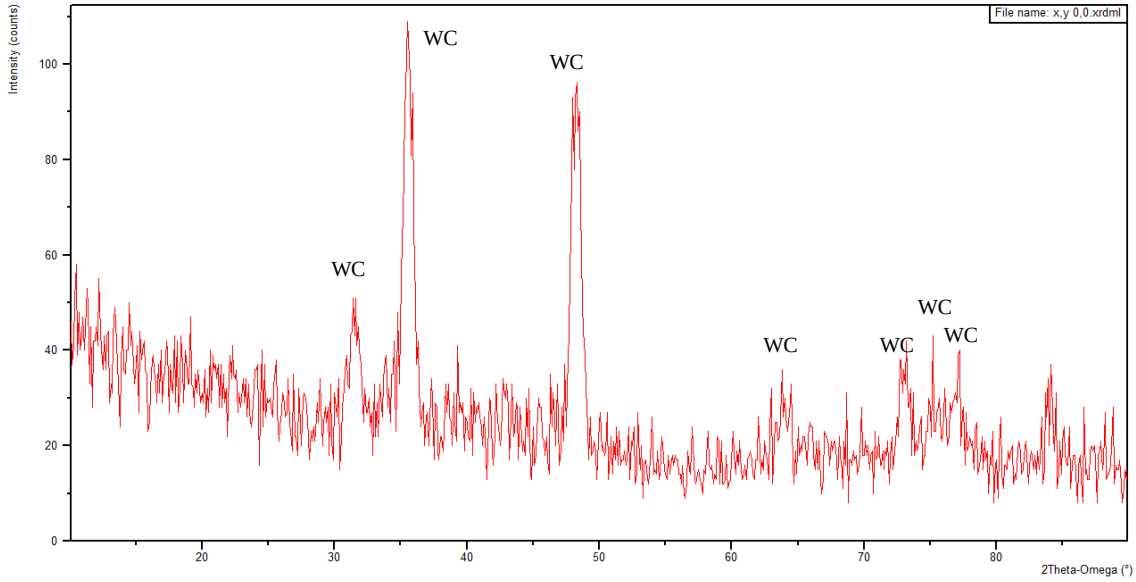

Figure 1.8: Punctual X-ray analysis of sample C5

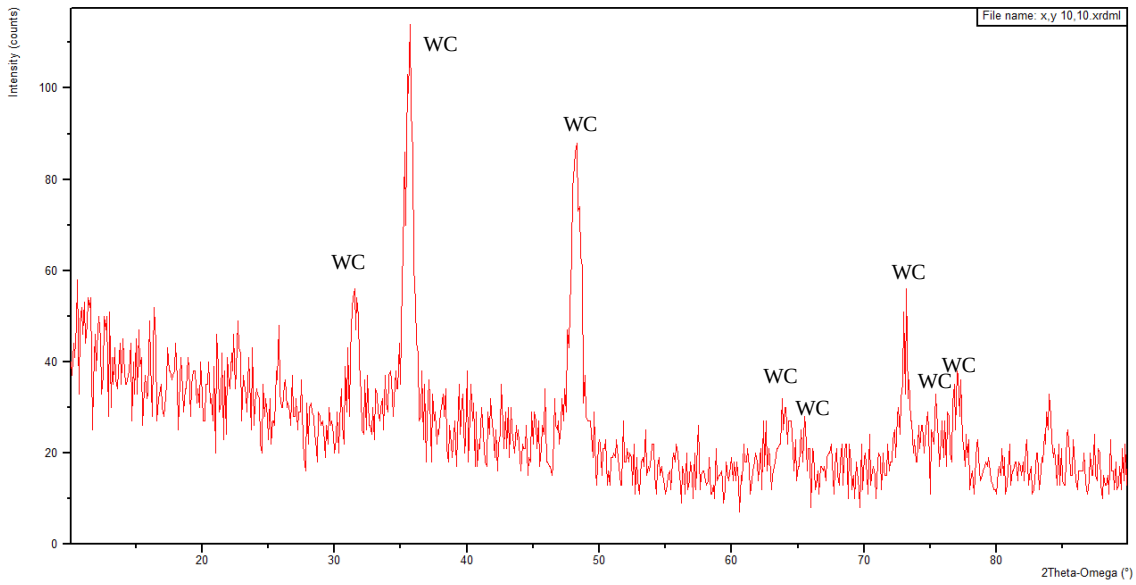

Figure 1.9: Punctual X-ray analysis of sample C5

References

[1.1] M. Merlin et al., *La Metallurgia Italiana, Consedit, Grado (Go)* **11**, 17-23 (2011), ISSN 0026-0843, and references therein

[1.2] V. Fervel et al., *Wear*, **230**, 70-77 (1999)

[1.3] R. S. Lima and B. R. Marple, *Journal of Thermal Spray Technology*, **14**, 397-404, (2004)

[1.4] J. C. Miranda and A. Ramalho, *Tribology letters*, **11**, 37-48, (2011)

[1.5] H. Herman et al., *MRS Bulletin*, 17-25, (2000)

[1.6] A. Dudek and J. Iwaszko, *Archives of Materials Science and Engineering*, **33**, 39-44, (2008) and references therein

[1.7] Y. Liu et al., *Surface and Coatings Technology*, **167**, 68-76, (2003)

[1.8] J. Iwaszko and Z. Nitkiewicz, *Materials Engineering*, **3/151**, 399-402, (2006)

[1.9] M. U. Devi, *Ceramics International*, **30/4**, 555-565, (2004)

[1.10] R. Yilmaz et al., *Journal of the European Ceramic Society*, **27**, 1319-1323, (2007)

[1.11] B. H. Kear et al., *Journal of Thermal Spray Technology*, **9**, 483-487, (2000)

[1.12] P. H. Shipway et al., *Wear*, 259, 820-827, (2005)

[1.13] K. Jia and T.E. Fischer, *Wear*, **203–204**, 310–318, (1997)

[1.14] K. Jia, T.E. Fischer, *Wear*, **200**, 206–214, (1996)

[1.15] B.H. Kear and L.E. McCandlish, *Nanostruct. Mater.*, **3**, 19–30, (1993)

[1.16] L.E. McCandlish et al., in: *R.M. Yazici (Ed.), Protective Coatings: Processing and Characterization, The Minerals, Metals and Materials Society, Warrendale, PA,* 113–119, 1990

[1.17] D. G. F. O'Quigley et al., *Int. J. Refract. Met. Hard Mater.*, **15**, 73–79, (1997)

[1.18] M.R. Dorfman et al., *Proceedings of the 12th International Thermal Spray Conference, London*, 291–302, (1989)

[1.19] K. Niemi et al., in: *C.C. (Ed.), Thermal Spray: International Advances in Coating Technology, ASM Int., Materials Park, OH, USA*, 685-689, (1992)

[1.20] J. Nerz et al., in: *R.M. Yazici (Ed.), Protective Coatings: Processing and Characterization, The Minerals, Metals and Materials Society, Warrendale, PA,* 135–143, (1990)

[1.21] R. Schwetzke and H. Kreye, in: *C. Coddet (Ed.), Thermal Spray: Meeting the challenges of the 21st century, ASM Int., Materials Park, OH, USA,* 187–192, (1998)

[1.22] B. Freudenberg and A. Mocellin, *Journal of Material Science*, **8**, 3701, (1990)

[1.23] K.A. Habib et al., *Surface and coatings technology*, **201**, 1436-1443, (2006)

[1.24] C. Verdon et al., *Microstructures Materials Science and Engineering*, **A246**, 11-24, (1998)

[1.25] J.M. Guilemany et al., *Advances in Surface & Coatings Technology* **201**, 1180-1190, (2006)

Conclusions

In this work they have been shown main experimental results of X-ray characterization of innovative semiconductor crystals for applications in astrophysics and material science.

In the framework of Laue lens for satellite-borne experiments in astrophysics, curved crystals developed at SSL (Ferrara, Italy) by surface grooving have been positively tested at ESRF and ILL (Grenoble, France). Indeed, the crystals have shown significantly high efficiency and broad-band response when subject to X-ray diffraction, proving that the technology of surface grooving opens up a viable way to build up optical components for X- or γ-ray diffraction without any size constraint, which may be useful for the realization of a Laue lens for observation of violent events in galaxy, where weight constraints do not permit any external mechanical device.

For realization of solar cells for photovoltaic applications, Ge heteroepitaxial layers developed at SSL by LEPECVD technique have been characterized by X-ray diffractometry and were proven to exhibit a well-defined Gaussian diffraction profile. This highlights that Ge layers are structurally crystalline, meaning that LEPECVD technique is a viable tool to fabricate Ge virtual substrates for multi-junction solar cells.